A Methodology for Variable Camber Assessment in Conceptional Aircraft Design

Eine Methode zur Bewertung von variabler Wölbung im konzeptionellen Flugzeugentwurf

Von der Fakultät für Maschinenwesen der Rheinisch-Westfälischen Technischen Hochschule Aachen zur Erlangung des akademischen Grades eines Doktors der Ingenieurwissenschaften genehmigte Dissertation

vorgelegt von

Fabian Nicolas Peter

Berichter: Univ.-Prof. Dr.-Ing. Eike Stumpf
Univ.-Prof. Dr.-Ing. Mirko Hornung

Tag der mündlichen Prüfung: 16.09.2025

Abstract

In the continuous challenge in aircraft design to further improve aircraft efficiency, variable camber has been addressed in aviation research several times. Examples of applications of variable camber are the optimization of lift distribution during cruise for standard operations and, more recently, enabling better performance on more diverse flight altitudes to avoid contrail formation. These and other applications call for considering variable camber in conceptual aircraft design, already employing its potential.

The main purpose of camber variation pursued by this thesis is to choose the best available camber for the specific flight condition and to assess the conceptual overall aircraft level. The vast majority of aviation transport is realised with aircraft operating at flight speeds that create flow conditions on the wing, necessitating the incorporation of compressibility effects. Assessing any technology focusing on changing airfoil characteristics in the transonic regime should employ compressible analysis methods. Therefore, the main challenge motivating this work is to develop a method that enables variable camber assessment, incorporating 2D airfoil analysis, considering compressibility effects, while offering stability and adequate computational effort to allow the typical studies necessary for conceptual aircraft design.

An extensive literature review showed that variable camber has been in aviation research and application for over 100 years. The results for the application on the aircraft level vary between 1 and 10 % drag reduction. A systematic approach incorporating variable camber in conceptual aircraft design was found to be lacking in the current state of the art. Therefore, a methodology for assessing variable camber in conceptual aircraft design has been devised to evaluate an advanced dropped hinge flap high-lift system as variable camber architecture.

A reference aircraft has been selected based on the Airbus A350-900 due to its advanced dropped hinge flap high-lift system application. Substantial efforts were made to prepare this reference aircraft to ensure its suitability for a solid assessment basis. This comprised the selection of baseline airfoils suitable for the occurring flow conditions and optimising the twist to achieve an appropriate lift distribution with the analysis methods employed. The former was a challenging task for the airfoils available in the public domain. This became especially clear when the 2.5D method was applied, incorporating compressibility effects. Subsequently, the methodology was applied to the reference aircraft. After deriving the deployed airfoil geometries, the application of the 2.5D method showed that the selected baseline airfoils were not ideal in their pressure distribution for the VC application.

The trends originating from the deployment of the 2D airfoils and their succeeding 2.5D integration into, first, the wing and, secondly, the overall aircraft polars showed to be consistent and in line with expectations and literature statements (0.35 % L/D improvement). The concluding assessment on the mission level continued this consistent propagation. It yielded trip fuel reductions (0.43 %), which was in line with the pure aerodynamic results, which also held for the study on system failure. These results demonstrated the desired behaviour and suitability of the proposed methodology.

Kurzfassung

Um die Effizienz von Flugzeugen weiter zu verbessern, wurde die variable Wölbung in der Luftfahrtforschung mehrfach untersucht. Beispiele für Anwendungen variabler Wölbung sind die Optimierung der Auftriebsverteilung und die Ermöglichung einer besseren Leistung in unterschiedlichen Flughöhen zur Vermeidung von Kondensstreifenbildung. Diese und andere Anwendungen erfordern eine Berücksichtigung der variablen Wölbung im konzeptionellen Flugzeugentwurf, um ihr Potenzial voll zu nutzen.

Während radikale Konfigurationen in Erwägung gezogen werden, um die Auswirkungen des Luftverkehrs auf den globalen Klimawandel zu mindern, bleibt die klassische Drachenflugzeugkonfiguration im Fokus der Forschung und bietet ein geringeres Risiko durch evolutionäre Weiterentwicklung. Der hohe Anteil des Flügels am Gesamtwiderstand macht ihn zu einem der Schwerpunkte der Forschung. Neben der Grundrissform sind Tragflächenprofile ein wichtiges geometrisches Merkmal. Die Möglichkeit, die Wölbung bestimmter Profilabschnitte des Flügels zu variieren, wurde von der Forschung mehrfach als eine Technologie mit hohem Potenzial identifiziert.

Der Hauptzweck der Wölbungsvariation in dieser Arbeit ist die Auswahl der besten verfügbaren Wölbung für die spezifische Flugbedingung und eine Bewertung auf konzeptionellem Gesamtflugzeugniveau. Der überwiegende Teil des Luftverkehrs wird bei Fluggeschwindigkeiten betrieben, die die Einbeziehung von Kompressibilitätseffekten erfordern. Daher sollten Tragflächentechnologiebewertungen für den transsonischen Bereich, kompressible Effekte berücksichtigen. Die Motivation dieser Arbeit besteht daher darin, eine Methode zu entwickeln, die eine Bewertung der variablen Wölbung unter Berücksichtigung von Kompressibilitätseffekten ermöglicht und gleichzeitig Stabilität und angemessenen Rechenaufwand bietet, wie sie für den konzeptionellen Flugzeugentwurf erforderlich sind.

Die Literaturrecherche ergab, dass die variable Wölbung bereits seit über 100 Jahren in der Luftfahrtforschung untersucht wird. Auf Flugzeugebene variieren die Ergebnisse zwischen 1 und 10 % Widerstandsreduktion. Ein systematischer Ansatz zur Bewertung der variablen Wölbung im konzeptionellen Flugzeugentwurf fehlt im derzeitigen Stand der Technik. Daher wurde eine entsprechende Methodik für die Bewertung von variabler Wölbung im konzeptionellen Flugzeugentwurf entwickelt. Die Hochauftriebssystemarchitektur wurde als „advanced dropped hinge flap" ausgeführt. Als Referenzflugzeug wurde der Airbus A350-900 ausgewählt, der diese Architektur besitzt. Dieses Referenzflugzeug wurde so weit vorbereitet, dass seine Eignung als solide Bewertungsgrundlage gewährleistet ist. Dazu gehörten die Auswahl von geeigneten Basisprofilen und die Optimierung der Verwindung. Ersteres erwies sich bei den öffentlich verfügbaren Profilen als anspruchsvoll, insbesondere durch die Anwendung der 2,5D-Methode unter Einbeziehung von Kompressibilitätseffekten. Nach der Ableitung der ausgeschlagenen Profilgeometrien zeigte die Anwendung der 2,5D-Methode, dass die ausgewählten Basisprofile in ihrer Druckverteilung für die VC-Anwendung nicht ideal waren.

Die Trends, die sich aus der Entwicklung der 2D-Profile und ihrer anschließenden 2,5D-Integration in den Flügel und die Gesamtpolare des Flugzeugs ergaben, waren konsistent und stimmten mit den Erwartungen und Literaturangaben überein (0,35 % L/D-Verbesserung). Die abschließende Bewertung auf Missionsebene zeigte konsistente Ergebnisse und ergab eine Verringerung des Reisekraftstoffs (0,43 %), die mit den rein aerodynamischen Ergebnissen übereinstimmte, was sich weiterhin in der Studie zu Systemausfällen entsprechend fortsetzte. Diese Ergebnisse belegen das gewünschte Verhalten und die Eignung der vorgestellten Methodik.

Acknowledgements

I thank Professor Eike Stumpf for guiding me during the thesis, which greatly aided its completion. His contributions and productive review improved it significantly. I also thank Professor Mirko Hornung for serving as my second examiner.

The Institute of Aerospace Systems of the RWTH Aachen University, where I conducted my research, provided an extremely team-oriented and productive atmosphere. The team's dedication to investing effort to integrate our individual work into a larger aircraft design framework has been truly impactful, enabling us to extend our capabilities. I want to express my special gratitude to Kristof Risse and Florian Schlütke. Their technical expertise was important to my research, and our social connections, including some memorable celebrations, are of great value to me. Furthermore, I would like to thank my good friends and office colleagues Abhishek Sahai and Michael Husemann, with whom I have shared many intense times, and their support was a big help. Although Tim Effing and I did not share a lot of time at the institute, the regular exchange on the methodologies and shared projects was hugely constructive and always a pleasure.

My entire research career would not have been possible without the unconditional support of my parents. They supported me from the first aircraft drawings of a small boy up until the completion of my studies while still creating aircraft designs. Lastly, I deeply thank my wife, Sophie, for her patience and the understanding she showed that, for a long time, this thesis was part of our lives and sometimes strongly influenced our plans.

Contents

List of Figures vi

List of Tables ix

List of Symbols x

1 Introduction 1

1.1 Motivation and Problem Statement 1

1.2 Thesis Approach 3

2 Development of Variable Camber Research 4

3 Method for Variable Camber Assessment in Conceptual Aircraft Design 26

3.1 MICADO 26

3.1.1 Overall Process 26

3.1.2 Aerodynamic Analysis 28

3.1.3 Mission Analysis 32

3.2 Incorporation of Variable Camber in MICADO 33

3.2.1 Variable Camber Airfoil Geometries 34

3.2.2 Polar Merger 39

3.2.3 System Failure Integration in Operational Mission Planning 40

3.3 Lift Distribution Optimiser 44

4 Application of Developed Method 46

4.1 Reference Aircraft 46

4.1.1 Derivation of Application Platform 47

4.1.2 Derivation of Wing Geometry 48

4.1.3 Airfoil Selection 51

4.1.4 Twist Distribution Adaptation Without Database Input 65

4.1.5 Twist Distribution Adaptation With Database Input 67

4.2 Derivation of Variable Camber Airfoils 70

4.2.1 Geometry of Airfoils with Deployed Trailing Edges 70

4.2.2 Aerodynamic Assessment of Deployed Airfoils 72

4.3 Incorporation of Deployed Airfoils and Polar Merging 79

4.3.1 Creation of Wing Geometry Permutations 79

4.3.2 Assessment of Merged Polars 80

4.4 Performance Assessment on Aircraft Level 82
4.4.1 Design Mission Performance 82
4.4.2 Performance with Enforced Flight Level Change 85
4.4.3 Impact of System Failure on Fuel Planning 88
5 Conclusion and Outlook 90
6 References 93
7 Annex 101
7.1 Variable Camber Airfoil Coordinates 101

List of Figures

Figure 1: Impact of flight level change on aerodynamic performance 2
Figure 2: General Dynamics F-111 Aardvark with mission adaptive wing [22]. 5
Figure 3: L/D improvement for mission adaptive wing [24]. 5
Figure 4: Variable camber concept of the Boeing study [27]. 6
Figure 5: Comparison of L/D vs C_L for long-range and short-range aircraft design [27]. 7
Figure 6: A300 basic wing L/D improvement by tab rotation increase at 35,000 ft based on [28]. 8
Figure 7: Trailing edge variable camber concept by Hilbig et al. [30]. 8
Figure 8: Variable trailing edge with rotating and translating flap and corresponding spoiler [31]. 9
Figure 9: Impact of trailing edge variable camber on airfoil aerodynamics by Hilbig et al. [30]. 9
Figure 10: Impact of trailing edge variable camber on aircraft level by Hilbig et al. [30]. 10
Figure 11: Trailing edge variable camber impact on cruise Mach number flexibility [30]. 10
Figure 12: Effect of camber increase on basic research airfoil pressure distribution [32]. 11
Figure 13: The impact of trailing edge camber variation on L/D performance [32]. 11
Figure 14: Crucial areas of an airfoil pressure distribution for variable camber [34]. 12
Figure 15: Comparison of the pressure distribution from experiment and theory for the VC airfoil [35]. ... 13
Figure 16: Guidelines for variable camber-specific airfoil design [37]. 13
Figure 17: Discrete variable camber as applied on the NASA X-29 [39]. 14
Figure 18: Prognosis of L/D improvement by wing technology integration [33]. 15
Figure 19: Results of the NEW II program [33]. 16
Figure 20: Plan-form and results for a variable camber wing design [33]. 16
Figure 21: Effect of spanwise variable camber on root bending moment [33]. 17
Figure 22: 2D wind tunnel results of variable camber deployment [40]. 17
Figure 23: Design requirements implied by a family concept [37]. 18
Figure 24: Variable camber optimised airfoil and wing for a medium/long-range aircraft [37]. 19
Figure 25: DOC and fuel mass savings due to VC for different aircraft sizes according to [47]. 20
Figure 26: L/D improvement during cruise by VC application [60]. 22
Figure 27: Theoretical L/D improvement for flap deployments, Ma 0.83, Lockheed L-1011 TriStar [62]. 22
Figure 28: Conventional (top) and variable camber continuous trailing edge flap (bottom) control surface setup of the NASA Elastically Shaped Air Vehicle Concept project [63]. 23
Figure 29: MICADO architecture [74]. 27
Figure 30: Conical flow assumptions on a tapered wing segment [75]. 30
Figure 31: Concept of the variable camber incorporation in MICADO. 33
Figure 32: Idealized adaptive dropped hinge flap concept. 34
Figure 33: Characteristic points of the flap definition. 35
Figure 34: Examples of flap cross sections by given by Rudolph [9] with characteristic flap points. 35
Figure 35: Parent airfoil with derive ADHF components. 36
Figure 36: Airfoil class data structure. 37
Figure 37:Data structure of the spanPosition class. 37
Figure 38: Initialization of the span position objects. 38
Figure 39: ADHF kinematic generation in the CDAG. 38
Figure 40: Creation of the deployed airfoils. 39
Figure 41: Concept of polar merging. 40
Figure 42: Mission Plan with ETOPS Areas [103]. 41
Figure 43: Route JFK - SNN with 90 min ETOPS [103]. 42
Figure 44: Mission Route JFK- (KEF) – SNN. 43

Figure 45: Scaling of normalised target lift distribution. 44
Figure 46: Twist adjustment to achieve scaled target lift distribution. 45
Figure 47: Approach for reference wing geometry derivation 46
Figure 48: Reference aircraft configuration. 47
Figure 49: Top view of the reference aircraft wing. 48
Figure 50: Local lift coefficients for the reference wing with an elliptical lift distribution [105]. 49
Figure 51: Reference aircraft wing segmentation. 50
Figure 52: Relative thickness and twist distribution of the CRM. 51
Figure 53: Extracted CRM airfoils and the transformed 2D geometry. 52
Figure 54: Effect of the XFOIL FILT command on the pressure distribution of the NASA SC 0712 airfoil. 53
Figure 55: Airfoils from the NASA super critical family for the inner and outer kink comparison. 54
Figure 56: Airfoils from the NASA super critical family for the root comparison. 54
Figure 57: Shock position iteration for the 3D to 2D flow condition transformation. 55
Figure 58: Shock position iteration and respective 2D flow conditions for the outer kink. 56
Figure 59: Reference airfoil comparison for total drag vs Ma for the outer kink. 56
Figure 60: Reference airfoil comparison for L/D vs C_{l_res} for the outer kink. 57
Figure 61: Reference airfoil comparison for Ma*L/D vs Ma for the outer kink. 58
Figure 62: Reference airfoil comparison for shock location vs Ma for the outer kink. 58
Figure 63: Shock position iteration and respective 2D flow conditions for the inner kink. 59
Figure 64: Reference airfoil comparison for total drag vs Ma for the inner kink. 59
Figure 65: Reference airfoil comparison for L/D vs C_{l_res} for the inner kink. 60
Figure 66: Reference airfoil comparison for Ma*L/D vs Ma for the inner kink. 60
Figure 67: Reference airfoil comparison for shock location vs Ma for the inner kink. 61
Figure 68: Shock position iteration and respective 2D flow conditions for the root section. 62
Figure 69: Reference airfoil comparison for total drag vs Ma for the root span position. 62
Figure 70: Reference airfoil comparison for L/D vs C_{l_res} for the root span position. 63
Figure 71: Reference airfoil comparison for Ma*L/D vs Ma for the root span position. 64
Figure 72: Reference airfoil comparison for shock location vs Ma for the root span position. 64
Figure 73: Lift distribution modifier result for the reference wing with and without additional segments. 65
Figure 74: Lift distribution modifier results for the reference wing with and without additional segments.66
Figure 75: Generic lift coefficient scaling factors. 67
Figure 76: Resulting lift distributions by applying step wise inboard shift on elliptic distribution. 68
Figure 77: Lift to drag ratio and respective lift coefficient dependent on scaling factors. 68
Figure 78: Drag breakdown for the optimum L/D flight condition dependent on scaling factors. 69
Figure 79: Airfoils created by the CDAG for most upward and downward deployment. 71
Figure 80: Pressure distribution of deployed airfoils for the outer kink. 72
Figure 81: Drag breakdown for the outer kink, C_l 0.8 Ma 0.75 Re 2.5e+07. 73
Figure 82 Drag over lift coefficient for all deployments on the outer kink. 74
Figure 83: Pressure distribution of deployed airfoils for the inner kink. 75
Figure 84: Mach number distribution of deployed airfoils for the inner kink. 75
Figure 85: Drag breakdown for the outer kink, C_l 0.7 Ma 0.72 Re 5.0e+07. 76
Figure 86: Drag over lift coefficient for all deployments on the inner kink. 76
Figure 87: Pressure distribution of deployed airfoils for the root. 77
Figure 88: Drag breakdown for the root, C_l 0.3 Ma 0.82 Re 1.0e+08. 77
Figure 89: Drag over lift coefficient for all deployments on the root. 78
Figure 90: Wing trailing edge with highest/lowest and zero deployment. 79
Figure 91: Excerpt of 3D aircraft polars for 4 sets of deployments. 80

Figure 92: number of used data points for merged polar for deployment set combination. 80
Figure 93: 3D aircraft polar with selected deployment combinations for all lift coefficients 81
Figure 94: 3D aircraft polar with selected deployment combinations for relevant lift coefficients excerpt 81
Figure 95: Altitude and C_L for the predefined trajectory for the reference and the VC aircraft. 83
Figure 96: Altitude and C_L for optimised ICA and fixed FL selection for the reference and the VC aircraft. . 83
Figure 97: Design mission flap deployments and lift coefficients for predefined and optimised trajectory. 84
Figure 98: Typical mission altitude and lift coefficient with optimised trajectory and flat cruise examples. 85
Figure 99: VC Flap deployments and lift coefficients for the flat cruise for FL 430 and FL 330. 86
Figure 100: Fuel reduction by VC integration for optimised trajectories and different flat cruise altitudes. 87
Figure 101: VC Flap deployments and lift coefficients of the system failure simulation. 88

List of Tables

Table 1: Summary of VC aircraft performance increases in literature 25
Table 2: Aerodynamic coefficient prediction methods for components based on [75] 28
Table 3: Reference aircraft key overall aircraft data. 48
Table 4: Plan-form data, 3D and initial 2D flow conditions for main reference wing sections. 49
Table 5: Effect on the XFOIL FILT command on the NASA SC 0710 airfoil global parameters. 53
Table 6: NASA SC airfoil thicknesses before and after transformation from 2D to 3D. 54
Table 7: Comparison of overall aircraft aerodynamic performance for reference wing geometries. 66
Table 8: Comparison of overall aircraft aerodynamic performance handbook vs. 2.5D database. 69
Table 9: Geometric data for the CDAG airfoil deployment. 70
Table 10: Performance parameters of the predefined and optimised design mission. 84
Table 11: Typical mission performance parameters for optimised trajectory and flat cruise examples. 86
Table 12: Enforced flat cruise fuels for reference and VC aircraft at different altitudes. 87
Table 13:Flight conditions and flap settings for the system failure analysis points. 88
Table 14: Fuel impact of system failure for the analysed ranges. 89

List of Symbols

Variables

c	Airfoil Chord, m
C_D	Drag Coefficient
$C_{D,ind}$	Induced Drag Coefficient
$C_{D,visc}$	Viscous Drag Coefficient
$C_{D,wave}$	Wave Drag Coefficient
C_l	Lift Coefficient (wing section/2D)
C_L	Lift Coefficient (wing/3D)
C_M	Pitching Moment Coefficient
c_p	Pressure Coefficient
D	Drag, N
g	Gravimetric Constant, m/s²
l	Sectional Lift, N
L	Wing Lift, N
L/D	Quotient of Lift and Drag
Ma	Mach Number, -
p	Pressure, N/m²
Re	Reynolds Number
S	Wing Reference Area, m²
T	Thrust, N
U	Velocity
W	Weight, N
W	Aircraft Current Weight, kg
x	Local Coordinate along Airfoil Chord Line in X-Direction
z	Airfoil Thickness, m

Greek symbols

ϕ	Sweep Angle
∞	Freestream Condition
Φ	polar angle in developed conical wing plane
ρ_∞	is the free-stream density
α	Angle of attack
η	relative span position

Subscripts

25	25% percent of airfoil chord
2D	Two dimensional
3D	Three dimensional
LE	Leading Edge
r	Radial
ref	Reference
TE	Trailing Edge

Abbreviations

ADHF	Adaptive Dropped Hinge Flap
AFTI	Advanced Fighter Technology Integration
CDAG	Control Device Airfoil Generator
CP	Critical Point
CRM	Common Research Model
CDAG	Control Device Airfoil Generator
DOC	Direct Operating Cost
ETOPS	Extended Range Operations
ETP	Equitime Point
GTM	Generic Transport Model
ICA	Initial Cruise Altitude
ILR	Chair and Institute of Aerospace Systems of RWTH Aachen University
ISA	International Standard Atmosphere
JFK	John F. Kennedy International Airport in New York City, USA
KEF	Keflavik Iceland
LDM	Lift Distribution Modifier
LILI	DLR multiple lifting-line code LIFTING_LINE
MAW	Mission Adaptive Wing
MICADO	Multidisciplinary Integrated Conceptual Aircraft Design and Optimization
MTOM	Maximum Take-Off Mass
NASA	National Aeronautics and Space Administration
NASA SC airfoils	NASA Supercritical Airfoil Family
NAT	North Atlantic Tracks
OEI	One Engine Inoperative
OEM	Operational Empty Mass
Q3D	Quasi-Three-Dimensional
RANS	Reynolds-averaged Navier-Stokes
SAR	Specific Air Range
SFC	Specific Fuel Consumption
SNN	Shannon Airport, Ireland
SST	Simple Sweep Theory
T/W	Thrust/weight Ratio
TAS	True Air Speed
TLAR	Top Level Aircraft Requirements
TOW	Take-Off Weight
TTBW	Transonic Truss Braced Wing
VC	Variable Camber
VCCTEF	Variable Camber Continuous Trailing Edge Flap
VCOPS	Variable Camber Operational Standards
W/S	Wing Loading
ZKP	Ziviles Komponenten Programm

1 Introduction

This thesis presents a methodology that can capture the 2D transonic effects of trailing edge variable camber (VC) while being fast, stable, and flexible enough for application in conceptual aircraft design. VC was employed in aircraft from the beginning of powered flight and has been reintroduced in the last generation of long-range aircraft (e.g. the Airbus A350 [1]). The adequate assessment of VC as a regular component of conceptual aircraft design has not yet been realised and should be routinely incorporated into the considered technologies. The author has published research before on the topic of VC, which will be included in this thesis [2–4].

1.1 Motivation and Problem Statement

The ever-increasing need to limit the impact of aviation on global climate change motivates the continuous improvement of aircraft fuel efficiency. While radical configurations are under consideration, the tube and wing layout remains the focus of research and offers smaller risks by enabling the introduction of evolutionary technologies. The high sophistication of the airframe technology has led to highly challenging demands for keeping costs for integrating new technologies acceptable [5]. The benefit of every technology must be thoroughly analysed, and its added value and possible increased complexity, cost, or weight must be defined.

The wing's high contribution to the overall aircraft drag, in the order of two-thirds for conventional tube and wing configurations [6], persistently puts it in the focus of aviation research. Next to the plan-form, the cross-section airfoils and, specifically, their camber are key geometric parameters. During the development of the Airbus A300-600, a performance increase due to the increase of airfoil camber was identified in the early 80s and subsequently integrated into its design [7]. The possibility of varying the camber of specific wing airfoil sections has been recognised multiple times by research in recent decades as a high-potential technology. Fielding states, after an analysis incorporating cost estimations, that an application of VC on a long-range, low- to medium-capacity aircraft has a high potential [8]. Today's dense air traffic dictates rules for separating aircraft near airports and over non-territorial areas such as the North Atlantic Tracks (NAT). This includes a vertical separation on the NAT of 1000 ft. Suppose an aircraft wants to change its altitude while on the NAT; it must change it by at least 2000 ft. To understand the aerodynamic implications of this separation, the lift and drag of the wing airfoil must be discussed. A key performance aspect of a wing airfoil can be described in terms of the drag created by the airfoil while generating lift. The performance of a specific airfoil depends on different parameters, the most important being included in the local lift coefficient c_l defined in equation (1), where l is the sectional lift, ρ_∞ is the free-stream density, U_∞ is the free-stream velocity, and c is the chord at that section.

$$c_l = \frac{l}{\frac{1}{2} * \rho_\infty * U_\infty^2 * c} \tag{1}$$

When applying the lift of the entire wing and S (wing reference area) instead of the chord, the equation can be adapted to compute the global lift coefficient of the entire aircraft c_L. Combined with the quotient of lift and drag (L/D), a commonly used diagram can be created showing L/D in dependence of C_L, shown in Figure 1 for a generic case. This "L/D polar" helps explain how the aircraft's aerodynamic performance alters between two flight level changes and over time. For example, it can be imagined that the aircraft has just changed its flight level during cruise and has reached its new target altitude, requiring a higher C_L due to lower air density. The plane burns fuel while flying at this flight level, reducing its weight. To keep the movement stationary, the lift has to decrease identically to the weight. According to equation (1), and the assumption of constant flight speed, C_L must be reduced, shifting to the left along the polar in Figure 1 and constantly changing its L/D. This is indicated by the upper arrow in Figure 1. With fixed airfoil geometry, in order to return to the optimum L/D, altitude has to be increased, decreasing the atmospheric density and thus increasing C_L. A flight level change must be executed, as indicated by the lower arrow in Figure 1.

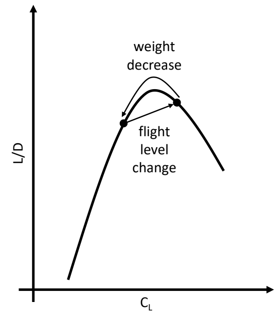

Figure 1: Impact of flight level change on aerodynamic performance

Changing the altitude is restricted to specified climb steps. This means most of the time, the aircraft is not flying in conditions where the airfoils of its wing perform optimally. Furthermore, the number of flight level changes is restricted by the air traffic control, and depending on the traffic density, a flight level change might be denied. Changing the airfoil geometry and thereby adjusting its optimum L/D to the current C_L is one of the applications of VC and the focus of this thesis. Conventional control surfaces such as flaps and slats are not suited for changing the airfoil geometry during cruise, mainly due to the drag their deployment would cause, e.g. due to the gap between the centre wing and the moving elements [9]. Therefore, control devices able to modify the airfoil shape during cruise without creating a gap are required for a feasible application of VC. This was realised in the Airbus A350 with the Adaptive Dropped Hinge Flap (ADHF) [1], also referred to as the advanced dropped hinge flap [10].

In addition to this application of VC, other technologies envisaged to have a sizeable synergistic potential with VC are a full span roll control, an aeroservoelastic[1] control [11] for wings with increased flexibility, as well as the application of (hybrid) laminar flow applications [12]. By applying the multifunctionality of trailing edge devices that can modify the lift distribution of a wing, a reduction in drag and structural weight can be expected by adapting to the aircraft's current weight or flight phase [13]. The shock development on the wing's upper surface is strongly sensitive to geometry changes and drives transonic wing wave drag [6]. Hence, assessing any technology focusing on changing airfoil characteristics in the transonic regime, present for large modern transport aircraft, should employ compressible flow analysis methods. However, these methods require higher computational effort and are less stable than methods commonly used in conceptual and preliminary aircraft design (e.g. vortex lattice or panel methods). Therefore, the main challenge motivating this work is to develop a method that enables VC assessment, considering compressibility effects while offering stability and adequate computational effort to allow the typical studies necessary for conceptual aircraft design.

[1] Use of control surfaces to mitigate reduced flutter margins of wings with increased flexibility by provision of load alleviation control.

1.2 Thesis Approach

To meet this challenge, the following approach has been defined for this thesis:

- **Selection of a suitable reference aircraft with variable camber enabling control surface type**
  The regime with the highest potential for the application of VC, according to the literature (see section 2), is the long-range segment. For this reason, the best-suited long-range reference aircraft featuring a control device setup capable of VC operation or enabling the incorporation of a VC-compatible control device setup will be identified (see section 4.1).

- **Deduction of deployed control surface airfoils from a control surface plan-form description**
  Since the method of this thesis is aimed at the application in conceptual aircraft design, the level of detail available at this stage must be considered. In conceptual design, information about the kinematics of the control surfaces from a detailed design is commonly unavailable. Instead, a default kinematic will be defined and applied to the plan-form of the control surface, which is often part of the conceptual design. The goal of this kinematic is to define the geometry of the deployed airfoils (i.e. airfoils with extended trailing edge surface and rotated spoiler) (see section 4.2.1).

- **Produce aerodynamic polars for 2D airfoil data for lift, drag, and moment**
  As pointed out previously, considering compressibility effects for a sound assessment of airfoil characteristics in the transonic regime of today's large transport aircraft is mandatory. Hence, a suitable method will be selected and established to calculate the 2D airfoil data (see section 4.2.2).

- **Incorporate 2D airfoil polars in 3D overall aircraft polars**
  For the overall aircraft assessment, the aerodynamic performance of the entire aircraft is necessary. The airfoil data will, therefore, first be integrated into the wing polars and then combined with the polars of the other components and drag contributors. A key aspect will be tracking the VC control device deployment angle for a specific point of the polar (see section 4.3.2).

- **Apply aircraft polars in an aircraft mission analysis with optimised VC application during cruise**
  For the method to be able to state changes in fuel due to VC, the application of the gathered polar data on specific aircraft missions is required. Therefore, a mission analysis will be conducted, which allows for a transparent interpretation of effects such as initial cruise altitude (ICA) selection, flight level changes, and, subsequently, mission fuel. As before, the tracking of VC control device deployment must be sustained to enable a sound interpretation of the influence of VC (see sections 4.4.1 and 4.4.2).

- **Define the application of mission planning considering possible VC system failure**
  Fuel planning must account for the respective malfunction to identify the true benefit of any technology with a theoretical potential for malfunction. For this purpose, a representative mission will be executed, following the Extended Range Operations (ETOPS) approach, and a suitable VC malfunction will be simulated to determine the required fuel reserve (see section 4.4.3).

2 Development of Variable Camber Research

Materials used in the early years of aviation were much less rigid than today's standards. This allowed for a relatively easy deformation. As early as 1890, J. J. Montgomery experimented with wing warping to achieve roll control. The better-known early example is the asymmetric warping of the wing for roll control of the 1903 Wright Flyer [14]. Dedicated research on VC was published by Parker in 1920. His focus was on the improvement of low-speed performance. He proposed three options for this challenge: variable angle of incidence, variable surface, and camber variation. Parker selected the latter one as the most viable option [15]. This is attributed to the higher performance compared to variable twist while being mechanically more complex, and vice versa if compared to variable surface. It should be kept in mind that this conclusion must be set into the context of the much more flexible materials used for aircraft at that time, mainly wood and canvas. The introduction of metal for the cantilever wing in the first full metal plane, the Junkers F-13, is representative of the increased use of metal and made flexibility less achievable. Furthermore, a higher degree of geometric deformation increased the complexity of the predetermination of aerodynamic properties. With an increased understanding of flow physics and fixed geometries highly optimised, geometric variation returned to aviation research. A strong motivation was the challenge posed by the then high speeds achievable by jet aircraft. While the swept-back wing concept was advantageously applied for drag reduction in the late phase of the Second World War, its complex low-speed characteristics called for unconventional solutions. VC was incorporated into fighter aircraft development quite early in the United States of America. It was introduced to the McDonnell Douglas F-4 Phantom II, which was commissioned in 1960 in various stages. The F-4 featured leading and trailing edge devices with dedicated fixed geometry surfaces, which could be deployed [16]. The National Aeronautics and Space Administration (NASA) approached further improving the performance and manoeuvrability of fighter aircraft with thin swept wings with moderate aspect ratios using conformal (i.e., geometry deforming in contrast to fixed geometry segments) VC in the 1970s. Ferris reported in 1977 on wind tunnel experiments employing leading and trailing edge camber variations with elliptical, circular form and single/double hinges on the leading and elliptical shapes on the trailing edge [17]. The airfoils were incorporated in a slim, low aspect ratio wing. It was found that the leading edge camber variation offered drag reduction from lift coefficients from 0 - 0.4 with an L/D improvement of up to 19%. In comparison, the trailing edge devices were effective for lift coefficients higher than 0.5 and yielded up to 34 % drag decrease in combination with a deployed leading edge. These promising results enabled the continuation of this line of research and led to sub-scale integration on an existing airframe. Boltz et al. presented the results of one of the first large-scale test campaigns focusing on integrating conformal VC devices on fighter aeroplanes. They compared the application of plain leading and trailing edge hinged devices to conformal VC devices on a model of a Vought F-8 Crusader in a transonic wind tunnel. The results showed a considerable lift increase while the drag increase was comparable small [18]. Due to their less complex kinematics, plain flaps became VC devices in many fighter designs. As stated by Siewert et al., subsequently, VC was integrated into several US fighter aircraft for an increase of manoeuvrability or drag reduction, including the Grumman F-14 Tomcat, Northrop F-5 Freedom Fighter, General Dynamics F-16 and McDonnell Douglas F/A-18 Hornet [16]. The specific case of the high manoeuvrability demand of fighter aircraft also calls for good performance at high lift coefficients. Siewert et al. present results for the Northrop F-5E Tiger II trailing edge deployment, which show a particularly large benefit at a high lift coefficient, a characteristic commonly stated for VC applications. A significant testbed for NASA's research on fixed-wing aircraft was the General Dynamics F-111 Aardvark. From 1975 on, research was undertaken leading to the fitting of the F-111 with a supercritical wing design in the transonic aircraft technology research program; consequently, the Advanced Fighter Technology Integration (AFTI) program developed the Mission Adaptive Wing (MAW) (see Figure 2)

[19–21]. The MAW's goal was to improve the efficiency of the aircraft in variable missions and flight conditions.

Figure 2: General Dynamics F-111 Aardvark with mission adaptive wing [22].

The MAW was equipped with a smooth conformal VC leading edge (forward 20 % chord) and conformal trailing edge (aft 40 % chord). The leading edge could be deployed -5° up and 30° down, and the trailing edge -7.5° up and 25° down. The deployment could be changed spanwise, with a restriction of 1° per foot of span [23]. The improvement in drag was presented by Gilyard and España and is shown in Figure 3. The drag improvement of the AFTI (named "Variable Camber" in Figure 3) varies from an L/D improvement of 8 % (design point: C_L 0.4 at Mach number (Ma) of 0.85) and over 20 % improvement for higher C_L (i.e. C_L of 0.8 and Ma of 0.7) [24].

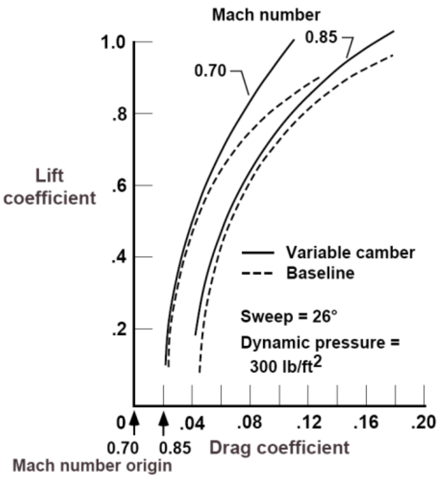

Figure 3: L/D improvement for mission adaptive wing [24].

Improvement of L/D was only one of the aims of the AFTI program. According to Gilbert [23], other goals were:

- Roll control: integral aileron action,
- manoeuvre load control: spanwise control of the aerodynamic centre for wing root moment reduction at high load factors,
- direct lift mode: increased lift without increased angle of attack and
- gust load alleviation: quick response camber variation to avoid gust impulse loads.

The control of the surfaces was automated in the later stages of the program to adjust the leading and trailing edge deployment according to data gathered in the wind tunnel and stored in a database. For the L/D optimisation, an automated algorithm was implemented, maximising speed for the given flight conditions and power settings. According to deCamp et al., additional flight modes were planned, including differential flap settings that optimised the spanwise lift distribution for each specific flight condition [25].

In civil aviation, the 1970s oil crisis triggered a vast number of technology programs for more fuel-efficient aircraft. Furthermore, Renken states the advances in computational power and tools for aerodynamic airfoil design in the late 1970s were the prime reason for the renewed research activities in airfoil research [26], making VC studies more viable. An extensive study was published in 1980, conducted by Boeing with funding from NASA [27]. The study's goal was to estimate the potential of leading and trailing edge benefits on the aircraft level for a technological status representative for 1980 and comprised three distinct aspects:

- The mechanical devices that provide the wing with the capability for variable geometry,
- the aerodynamic capability for various stages of flight (i.e. take-off, cruise and approach) and
- the capability to integrate with and improve the characteristics of transport aircraft configurations.

The concept featured a conformal leading edge VC device extending as far back as 25 % of the wing chord while being able to deploy 30° down. The conformal VC trailing-edge device could extend as far forward as 55 % of the wing chord with a maximum upward deployment of 15° and downward of 20° (see Figure 4). The variable camber concept was applied to the outboard 65 % of the wing.

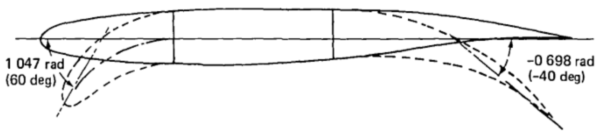

Figure 4: Variable camber concept of the Boeing study [27].

Two aircraft configurations were analysed: an intercontinental (long-range) and a domestic (short-range) configuration. The results for the intercontinental configuration showed a potential fuel saving of 3.1 % for the design mission of 5,500 nmi and 4.2 % for a shorter mission based on the averaged airline route structure. For the domestic configuration, the fuel saving was estimated to be 4.0 % for the design mission of 2,000 nmi and 1.5 % for the reduced range mission. The resulting L/D polar of the two aircraft for Ma 0.8 is shown in Figure 5. For the domestic aircraft, design variant "A" contained a design with increased wing area, while variant "B" kept the wing size from the reference and featured a double-slotted flap design.

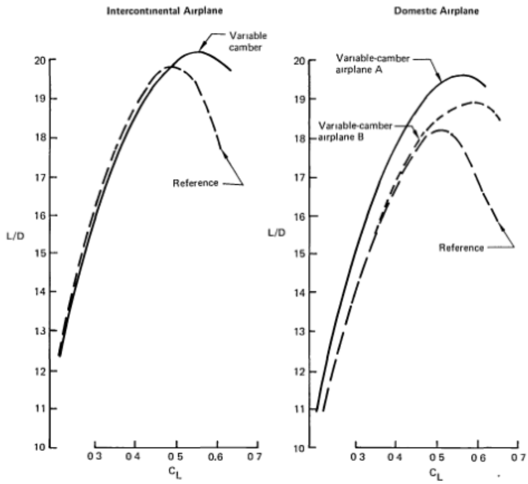

Figure 41. Aerodynamic Efficiencies, Mach = 0.8

Figure 5: Comparison of L/D vs C_L for long-range and short-range aircraft design [27].

Like Boeing, Airbus also analysed the potential of variable cambers on aircraft performance and integrated results into the development of their products. Mantel reports in 1982 on the development of the Airbus A300-600, which was based on the A300B4, during which one of the main features integrated was the increase in trailing edge camber [28]. The motivation for the change was to:

- Increase the buffet margin by at least 5%,
- improve cruise L/D and
- reduce the increase in wing root bending due to increased total wing lift.

Mantel states that the spanwise distribution of the camber increase had a decisive impact on the overall drag characteristics, considerably more significant than the chord-wise extension. The comparison of a camber variation restricted to the inboard portion of the wing and a variation including the outboard flap showed better results if the outboard flap was included. Also, no measurable influence of the chord variation could be determined. With a change in the preset of the flap tabs, the buffet margin could be increased by 7.4 %, allowing for a take-off weight increase of 5 %. The resulting change in L/D is shown in Figure 6. The optimum L/D is shifted to higher $C_{L,}$ and the L/D improvement is restricted to C_L higher than 0.38, thereby including the entire cruise C_L range.

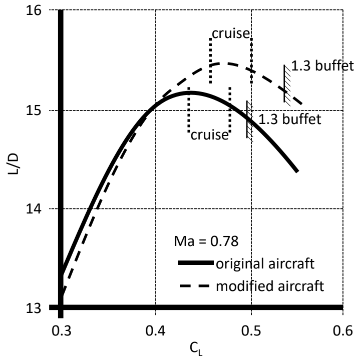

Figure 6: A300 basic wing L/D improvement by tab rotation increase at 35,000 ft based on [28].

Taking the increased lift into account, an L/D increase of 1.8 to 2.3 % was achieved for the respective design area of C_L. Therefore, the stated goals could be fulfilled, which was a significant reason for the actual realisation of the A300-600. The awareness of the potential of camber modification also led to the implementation of an adaptive camber wing able to change camber during flight in the official goals of the Airbus development program. In 1983, Ewald stated that this goal was to be implemented in 3 to 5 years [29]. This was, however, not implemented in the subsequent Airbus A310 development. The research for implementing VC was nonetheless extended, e.g., in the Civil Component Programme (German: Ziviles Komponenten Programm, ZKP). Hilbig et al. present different kinematic solutions for VC from the ZKP in 1984 [30]. The basic assumption for these kinematics was that flexible skin over the entire airfoil chord did not seem feasible. Therefore, solutions applying separated single components (discrete VC) were developed. The concept shown in the upper half of Figure 7 foresees the usage of the spoiler surface as a flexible component and a rotating main flap segment with a preloaded aft tap. The lower concept shown in Figure 7 omits the aft tap and employs a flap segment with fowler motion, thereby already containing the main features of the A350's ADHF, which is analysed in this thesis.

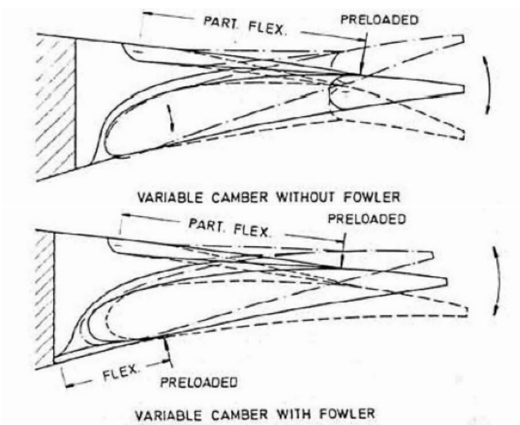

Figure 7: Trailing edge variable camber concept by Hilbig et al. [30].

A further increase in the level of detail for this concept was conducted and presented by Renken and Carl (see Figure 8) in 1982 [31]. With this concept, a droop angle of 8° was achieved with a combination of flap body rotation and the corresponding spoiler movement, prohibiting the creation of a gap. Renken also presented a concept for flight control integration, considering the impact on the engine auto throttle strategy [26].

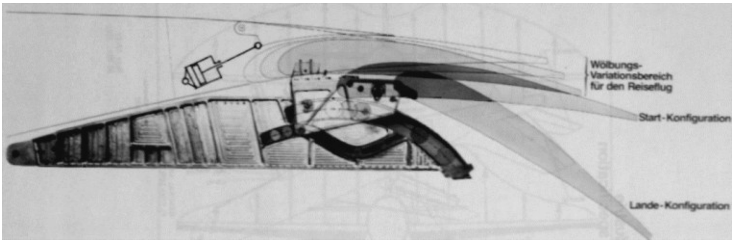

Figure 8: Variable trailing edge with rotating and translating flap and corresponding spoiler [31].

A report by Hilbig et al. published in 1984 describes wind tunnel tests of the airfoils with these trailing edge modifications. The mechanism was not implemented, but the shapes were tested by attaching exchangeable trailing edges on the wing. The impact of these trailing edge camber variations is shown in Figure 9. Hilbig et al. do not state the deployment angle, but an arrow indicates the trend for camber increase. On the horizontal axis, three different parameters are shown. On the left side is the moment coefficient (C_m), followed by the angle of incidence (α) and the drag coefficient (C_D). The vertical axis shows C_L (further called C_l since the diagram shows 2D/section-wise data). As expected, the relation between C_l and α is linear until a certain point and then shows a decrease in slope. The lift curves show a parallel shift with an increase in zero-lift with an increase in camber. Buffet onset occurs at nearly the same α and thus at higher C_l. C_m shows the same characteristics with an increase in a nose-down pitching moment for increasing camber. This can be explained by the rise in tail loading with increasing camber. The curves of C_d show an increase in minimum drag for increasing camber and a reduction of C_d for higher C_l. This leads to a crossover point at which a specific camber value leads to the lowest C_d.

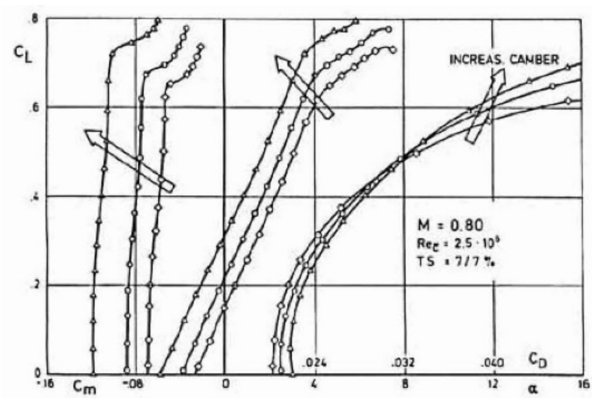

Figure 9: Impact of trailing edge variable camber on airfoil aerodynamics by Hilbig et al. [30].

Hilbig et al. trimmed the wind tunnel results and translated them to an aircraft configuration of the early 1990s that is not described in more detail. The resulting impact on L/D is shown in Figure 10. L/D is shown in relation to C_L. Hilbig et al. state that the upper curve incorporates several camber variations, including increases up to 5°. At the design C_L, an L/D increase of about 3 % is achieved (see Figure 10). The figure furthermore states the experimental conditions, including a Ma of 0.8 and a Reynolds number (Re) of 7.22 million. These conditions are well in the transonic regime and would be difficult to assess with lower-order computational methods at that time. Hilbig et al. state that these benefits translate into a block fuel reduction of 5 %.

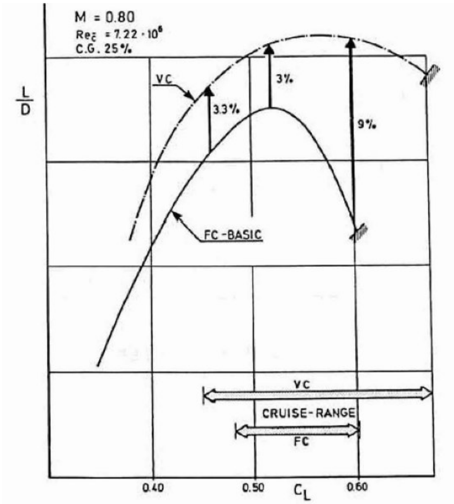

Figure 10: Impact of trailing edge variable camber on aircraft level by Hilbig et al. [30].

Hilbig et al. also indicate the increased operational flexibility gained by the variable camber application via the flatter optimum of the product of Ma and L/D (see Figure 11).

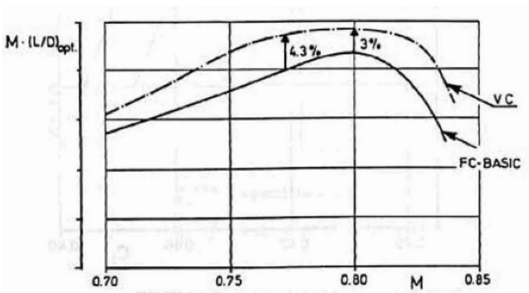

Figure 11: Trailing edge variable camber impact on cruise Mach number flexibility [30].

Szodruch refers to the publication of Hilbig et al. [30] and draws the same conclusions regarding the effects of increased trailing edge camber in 1985 [32]. He further states that for a data set consisting of a comparison of wind tunnel and flight test data, the impact of Re was found to be negligible. However, he states that this might not be suitable as a general statement. As an example of the effect of trailing edge camber increase on the pressure distribution, he comments on Figure 12 that the increase of camber moves the shock backwards. In a later publication, Szodruch further states that the increase of camber increases the load on the rear of the airfoil, reducing large local velocities and thus decreasing friction drag [33].

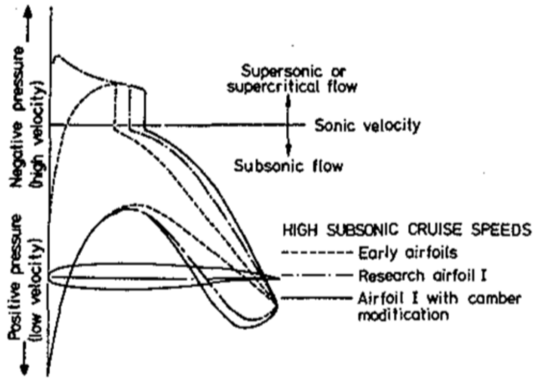

Figure 12: Effect of camber increase on basic research airfoil pressure distribution [32].

Szodruch shows the results of an experimental investigation of the variation of the L/D polar for a supercritical wing design in which the trailing edge was modified between 85 % and 100 % chord (see Figure 13). The optimum of the envelope of the single airfoil polars is flattened, thereby offering a broader operational flexibility. He further states that 6° is the maximum sensible deployment since this deployment already leads to relatively early flow separation at the trailing edge.

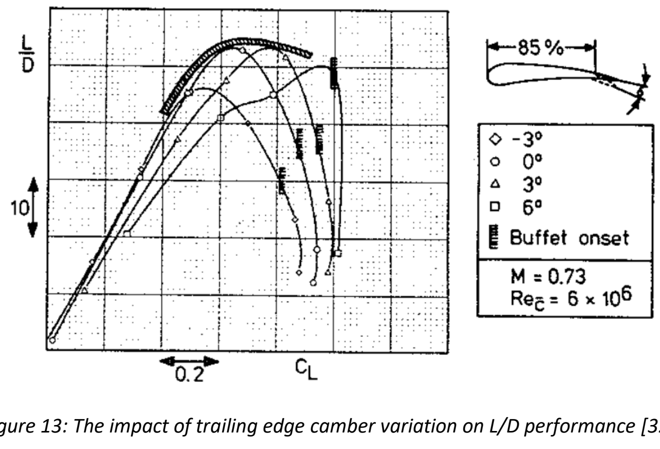

Figure 13: The impact of trailing edge camber variation on L/D performance [32].

Szodruch further discusses specific aspects of a VC-optimised airfoil design. While this thesis does not aim to execute a design of the complete airfoil for VC, it offers valuable context for the ideal application of VC. Furthermore, the information might be helpful in follow-up work. Hence, some aspects provided by Szodruch and connected research are relevant to discuss. In 1986, Szodruch listed the most problematic areas of airfoil pressure distribution concerning VC [34]. Szodruch states the following challenges for the areas shown in Figure 14:

1. A strong shock (1) can induce a separation for a small positive camber increase.
2. The shock of a possible second supersonic area (2) may be positioned at the hinge of the spoiler. In combination with the strong recompression gradient (3) and the curvature change at this position, separation would be most likely.
3. A convex pressure gradient at the trailing edge (4) might lead to separation, although this would not be to a very large extent.
4. On the lower surface, a late pressure minimum (7) and the resulting high gradient in the pressurisation area (6) negatively influence the boundary layer with potential for separation.
5. A profound rear loading (5) can lead to separation at small positive deployments.

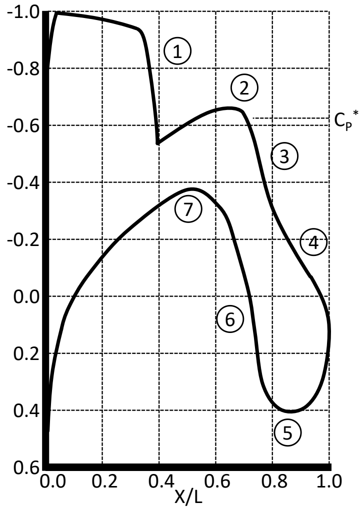

Figure 14: Crucial areas of an airfoil pressure distribution for variable camber [34].

Based on these insights, an airfoil with a specifically VC-friendly pressure distribution was developed. Unfortunately, no coordinates of the airfoil geometry are available. An attempt to execute an inverse airfoil design from the pressure distribution given in Figure 14 did not yield exploitable results.

An indication of the effectiveness of the implementation of this strategy for a pressure distribution is given by Greff in a publication from 1988 [35]. This publication compares a conventional airfoil designed for C_l 0.6 and Ma 0.74 with a VC airfoil designed for C_l 0.48 [36]. Both airfoils were designed with a target pressure distribution, implementing the strategy mentioned above for the VC airfoil and applying a full potential solver coupled with a semi-inverse boundary layer integral model. The comparison of the pressure distribution for the theory and experiment of the VC airfoil is shown in Figure 15.

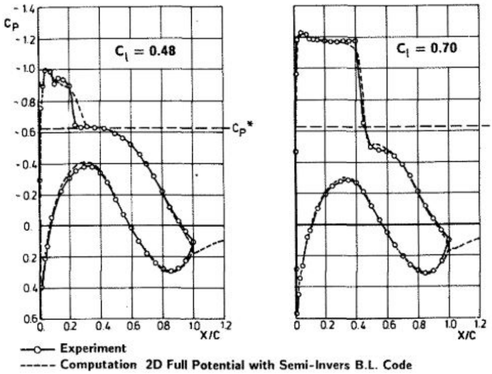

Figure 15: Comparison of the pressure distribution from experiment and theory for the VC airfoil [35].

VC trailing edge devices with different chords were analytically and experimentally tested, producing a 2-4 drag count (11.8% L/D) benefit of the VC airfoil at the design Ma of 0.74 and a 20 % higher C_l. Greff further lists specific guidelines to achieve this pressure distribution, which are visualised in Figure 16 [37].

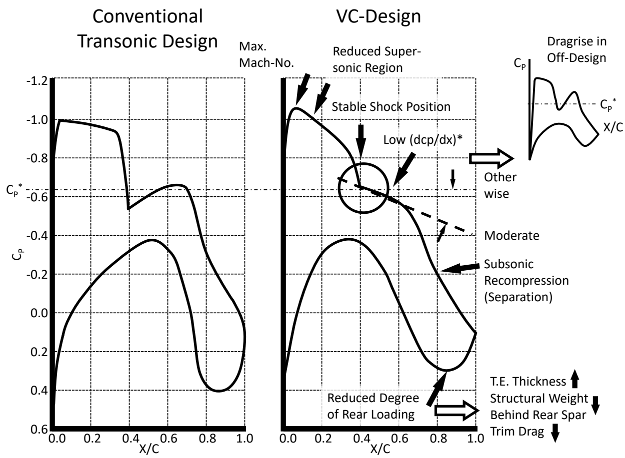

Figure 16: Guidelines for variable camber-specific airfoil design [37].

The guidelines are:

- Restrict supersonic region to a relative chord position of 40%,
- in the vicinity of the critical pressure coefficient (c_{p*}), pressure gradients should be moderate to stabilise the shock position,

- in the recompression area, gradients should be smaller than $dC_p/dx = 3$,
- the trailing edge pressure gradient should be degressive and
- the lower surface should show an increase in front loading to mitigate the pitching moment effect of the camber increase.

Extensive research activities in the VC field, especially the publicly funded research programs, led to a state of VC technology that was considered for upcoming aircraft development programs. As Szodruch states in a publication from 1986, VC was specifically one of the technologies under consideration for the development of the Airbus A330 and Airbus A340 [34]. Since these aircraft differ quite substantially in their Top Level Aircraft Requirements (TLAR), e.g. the A340 features a significantly longer range than the A330, the common wing design envisaged for the A330 and A340 made the operational flexibility gained by VC an attractive aspect. However, variable camber was not included in the wing design of these programs.

The integration level of the VC concepts increased with further maturation of the basic concept. Renken discusses different aspects on aircraft level in 1987 [5]. For the application of spanwise differential VC, e.g., the torque shaft has to be split to adjust the lift distribution in specific flight phases. Not only does this allow different deployments of adjacent flap panels, but if further split, flap panels can be deformed to achieve more flexibility in deployment adjustment. Renken further extends his concept for integrating camber variations in flight procedures and the integration of control algorithms for the deployment. The principle is a predefined deployments table with the current aircraft weight and the flight condition (i.e. altitude and speed) as input variables. Already in the mid-80s, studies concluded that the then-available data should be sufficient for the required control. The main functions of the flight management computer would be mainly unchanged by this procedure since it has the enveloping polar as input and not the multiple polars of the possible deployments. The required functions can be integrated into the flight augmentation computer and transmitted via existing communication paths. The concept of the enveloping polar is also applied in this thesis (see Section 3.2.2). It should be noted that alternative suggestions have been made. McAvoy et al. presented a control scheme for the optimised application of a trailing edge VC system on a natural laminar flow airfoil in 2002 [38]. This control system employs pressure measurement orifices at the wing section to determine the stagnation point. This information is used to control the deployment of a trailing edge flap to adjust the laminar bucket according to the airfoil lift coefficient.

Computerised control of the VC system was also central for the NASA X-plane X-29A forward-swept-wing flight research program [39]. The X-29 saw the application of an automatic camber control system and had its first flight in 1985. While the most prominent feature of the X-29 was a forward-swept wing, it also incorporated discrete variable camber at the main wing trailing edge (s. Figure 17).

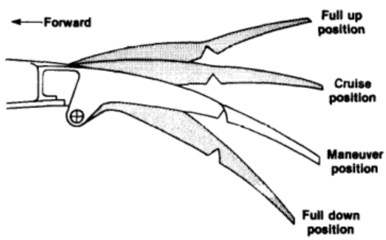

Figure 17: Discrete variable camber as applied on the NASA X-29 [39].

The goals of the discrete variable camber in the X-29 were to:

- Minimize trim drag,
- maximise off-design performance and
- minimise wave drag.

Szodruch et al. summarise the VC activities up to 1988 and derive that VC is a standard technology for glider planes, has been implemented multiple times in military fighter aircraft, and that discrete VC in the X-29 was proven to be almost as efficient as conformal VC while at considerably less cost and complexity [33]. An important role is prognosed for VC for integration in civil aviation, as visible in Figure 18. Here, an application for the A330/A340 of VC is already envisaged while combining it with further technologies (e.g. shock-boundary layer interaction) for a possible follow-on program.

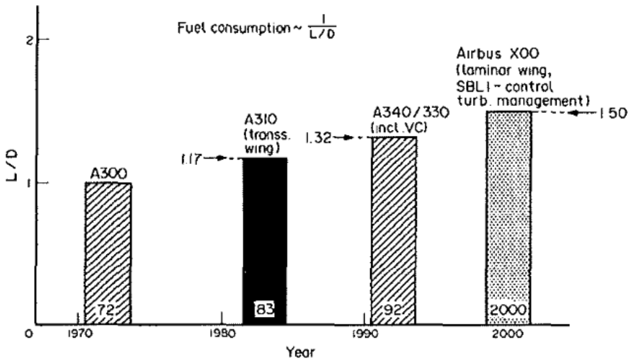

Figure 18: Prognosis of L/D improvement by wing technology integration [33].

In the same publication, Szodruch et al. further report on two research programs concerning the implementation of VC on existing wing designs, NEW I and NEW II (German: Nutzlast-Erweiterung, English: payload increase). While NEW I focused on improving an existing wing design with a peaky pressure distribution airfoil, NEW II dealt with a wing design incorporating a supercritical airfoil design and a generally high degree of optimisation for that time. Figure 19 shows the analysed modifications of NEW II, which focused on the change of inboard trailing edge deployment. The respective results on L/D are displayed on the right-hand side of Figure 19. The figure indicates that an L/D increase over the basic wing of 1.5 % could be achieved.

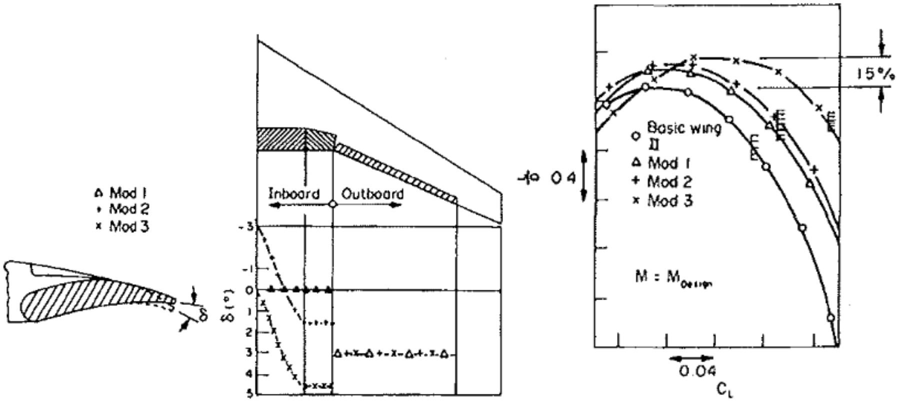

Figure 19: Results of the NEW II program [33].

As a subsequent step, Szodruch et al. describe a research program devising a new wing with VC aspects incorporated in the design from the beginning. The wing's plan-form and control surface layout are shown on the left-hand side of Figure 20. The achieved L/D improvements in relation to a comparable conventional wing are shown on the right-hand side of Figure 20 and show an increase of 3 % - 9 %. In addition to the L/D improvement, a 12 % increase for the maximum allowable C_L with respect to buffet onset was achieved.

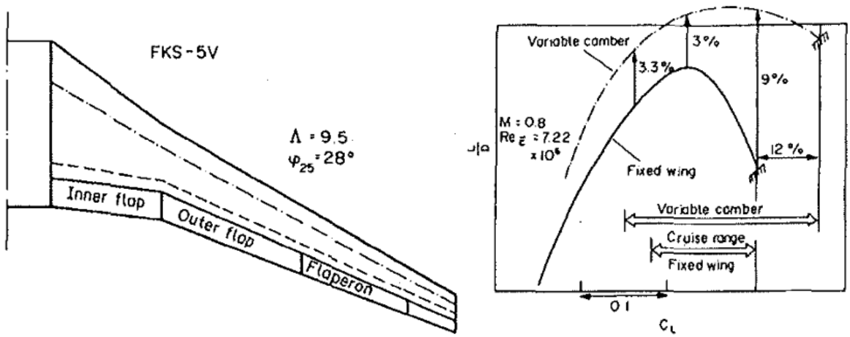

Figure 20: Plan-form and results for a variable camber wing design [33].

In the same program, studies were conducted for the differential spanwise application of VC. The results are presented in Figure 21. A reduction in wing root bending moment of up to 23.7% could be achieved by redistributing the lift over the wing differently for high load cases. This concept can also be applied to the design of load cases (e.g., a 2.5 g pull-up manoeuvre), and it can even lead to a negative lift on the outboard wing.

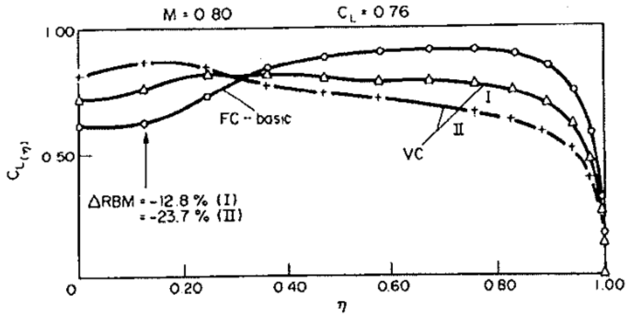

Figure 21: Effect of spanwise variable camber on root bending moment [33].

Hilbig et al. report on the same studies and add a graph containing results for the L/D increase [40]. This graph is shown in Figure 22 and depicts L/D versus C_L polars for several variable camber deployments. The data in the graph result from 2D wind tunnel experiments. While determining the absolute values of L/D is impossible, the characteristic of a high VC potential and an increase of effect with an increase of C_L is visible.

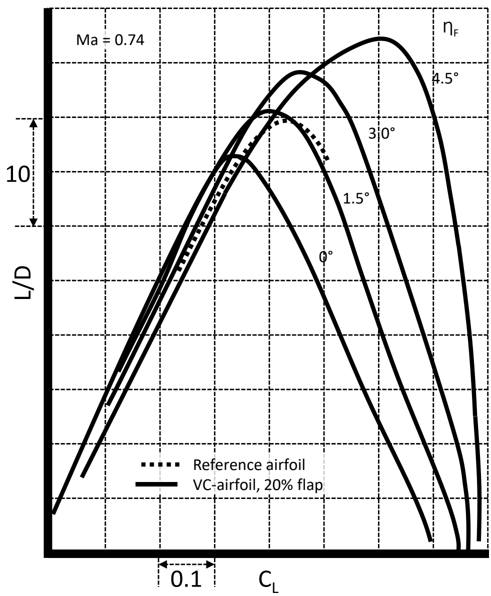

Figure 22: 2D wind tunnel results of variable camber deployment [40].

In a journal publication of Greff, the results described by Szodruch and Hilbig are integrated and put into a larger context [37]. Greff sees VC as a key technology to mitigate the compromise imposed by a common wing for an aircraft family. This challenge is visualised in Figure 23. The figure shows the increase in take-off weight (TOW) by a stretch of a baseline aircraft and the impact on the C_L values occurring during a mission for a long-range aircraft with four engines and a medium-range aircraft with two engines.

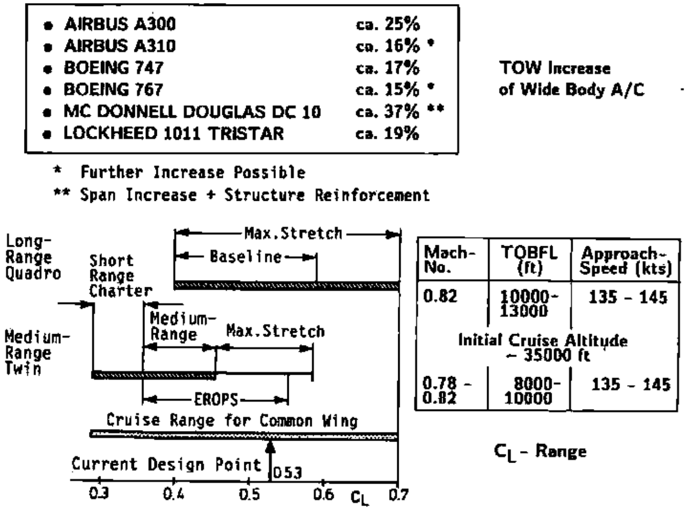

Figure 23: Design requirements implied by a family concept [37].

Based on these values, the need to increase the wing surface of the baseline aircraft above its specific optimum to enable the common wing for the stretched variant is derived. Greff sees a prime application scenario for VC in the possibility of increasing the effective applicability of higher C_L by increase of camber with one wing, thereby mitigating the otherwise necessary increase of wing area. While realising the benefits of improved drag characteristics in off-design C_L values, Greff states that the penalty by increased trim drag due to increased camber is one order of magnitude smaller than the achieved drag improvement. This strategy and a specific VC airfoil designed with the above guidelines were incorporated in a medium/long-range aircraft design study. The result of this study is shown in Figure 24 and depicts the L/D versus C_L polar. Compared to the fixed camber reference wing, with a conventional airfoil, the VC design achieves a 4 % increase in L/D at the design point of the fixed camber wing and a 12% increase in buffet margin.

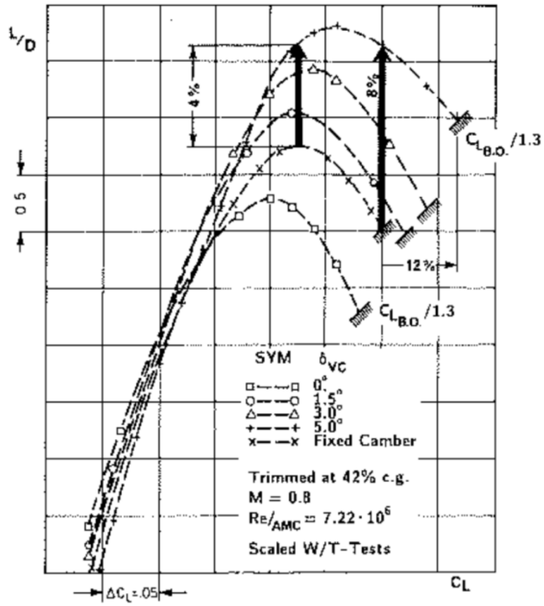

Figure 24: Variable camber optimised airfoil and wing for a medium/long-range aircraft [37].

In 1998, Monner et al. cited the publication by Greff [37] and postulated its application in an Airbus "Megaliner" concept [41]. This was before the announcement of the Airbus A380 program. Monner further explains that while the concept cited by Greff has potential, the long-term goal would be flexible (conformal) fowler flaps. A concept deforming the last 30-40 % of the flap is presented. The goals of this deformation are the same as the ones described by Hilbig [30], Szodruch [32] and Renken [26]. The concept is described as capable of deploying +/- 15°. The actuation is described in more detail, but no aerodynamic performance is given. Similarly, Bauer et al. also postulate the requirement and introduction of a flexible trailing edge device for VC application and present a structural concept [42].

The strong growth in the availability of computational power in the 1990s enabled the application of large aerodynamic numerical studies. These increased computation capabilities were applied at the Cranfield Institute of Technology and used in several years of active research in the area of VC. Spillman describes the approach and concept for VC studied at the Cranfield Institute of Technology in the early 90s [43]. For the basic benefit of VC, he refers to the characteristics of an airfoil family, i.e. the NACA 6 airfoil family, as described by Abbott and von Doenhoff [44]. Spillman reasons that for an increase in the lift coefficient, the camber of the optimal airfoil increases as well. He explains this effect with an increased loading of the airfoil's trailing edge that leads to a reduction of local velocities at the leading edge and, hence, a reduction of friction drag. Furthermore, Spillman postulates a possible weight reduction due to an inboard loading of the wing during manoeuvre load cases and a reduced bending moment. This weight reduction potential was analysed in a study at Cranfield and estimated to lead to a 10 % wing mass reduction. This estimate includes a 25 % weight increase of the flaps for VC incorporation and a 10 % higher mass of the flight control system. A structural design for Spillman's VC concept was developed and tested by Macci [45]. Fielding et al. describe in 1992 studies based on Spillmans's research conducted at Cranfield, optimising a VC concept starting with a supercritical airfoil with a 14% thickness to chord ratio and a hinge line position at 64.5 % of the chord [46]. The theoretical results were compared against wind tunnel experiments of a rhombus wing with a 25° sweep and several spanwise segments tested at 50 m/s and a Re of two million. The results showed a good agreement of the lift slopes. For a 5° deployment, improvements in drag could only be achieved for C_L higher than 0.8. Different combinations of deployments were tested, with the outcome that an increase in deployment of the inner spanwise segments produced a stronger lift increase than the outer segments; hence, the influence of spanwise deployment can be described as non-linear. On overall aircraft level, Fielding and Vaziry-Zanjany applied the results of available VC research on the overall aircraft level and published them in 1996 [8]. Drag savings for an A340-like aircraft in cruise were estimated to be:

- 0.9 drag counts by fuselage drag reduction (due to changed angle of attack),
- 0.0857 drag counts by viscous interference and
- 5.833 drag counts by induced drag.

The sum of this is 6.8 drag counts. With assumptions for an A340-300 (mid-cruise weight 200 t, wing reference area of 360 m², flight altitude of 35,000 ft, Ma 0.82), C_L can be estimated to be 0.486 (see equation (1)). If an L/D of 19 is assumed, C_D can be calculated to 0.025554 or 255.5 drag counts. For these assumptions, the drag savings amount thereby to 2.28 %. A flap weight estimation method for calculating VC flap weight was applied, and a mass of 3518 kg was calculated for an A340-like aircraft for the VC trailing edge surfaces, compared to 2771 kg for the conventional surfaces. For a twin-engine long-range airliner with VC for 210 passengers and a design range of 11230 km, Fielding and Vaziry-Zanjany state results of their performance and cost estimations. With a 6 % fuel reduction, they calculate a 2 % direct operating cost (DOC) reduction [8]. The created framework was further applied to generate overall aircraft results for several aircraft sizes and is described with its discipline-specific methods in Vaziry-Zanjany's Ph.D. thesis [47]. Results for various aircraft sizes are given, including the estimated reduction in fuel mass and DOC (see Figure 25).

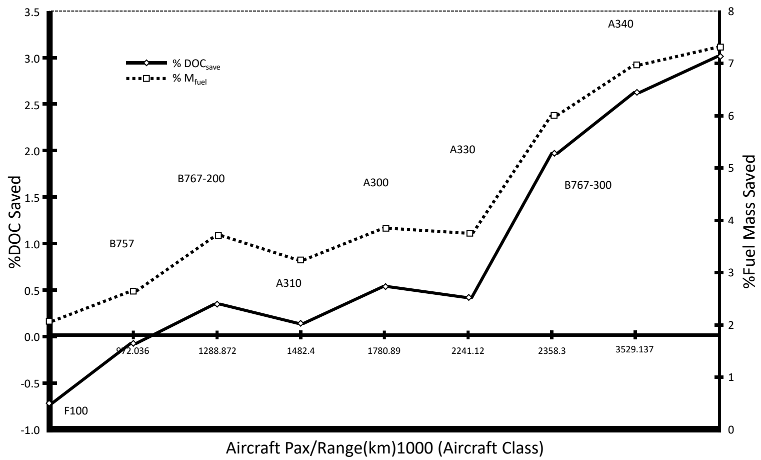

Figure 25: DOC and fuel mass savings due to VC for different aircraft sizes according to [47].

A compilation of the research activities regarding VC from 1988 to 1999 that took place in Cranfield was given by Fielding in 2000 [48].

The further growth in computational power enabled the employment of more sophisticated aero-numerical methods. Siclari et al. present a study conducted at Northrop Grumman in 1997, optimising the hinge lines of a two-dimensional airfoil with three flap segments [49]. The study employs full potential code coupled to a turbulent integral boundary layer methodology. The optimal hinge position and deployment angles for two Ma (0.726 and 0.815) and specific C_l (0.7 and 0.55) were determined in the first step. In the second step, the solution resulting in the minimum sum of the drag for the two Ma was identified. The solution was analysed using a Navier-Stokes solver. The reduction in drag counts for the lower Ma was 98 according to the Navier-Stokes analysis and 63 according to the full potential method. The reason for the deviation is reported to be the weak shock approximation in the full potential method. For the higher Ma, the results were 30 and 20 drag counts, respectively. Despite the available computational power, studies have been published after the year 2000 and are still published applying analysis methods neglecting compressibility effects on transonic cases due to their stability, ease of use and relatively low computational effort. Many of these studies do include comments that the impact of compressibility will most likely change the results severely (e.g. Martins and Catalano [50–54]). Incompressible methods are especially attractive for studies with a large design space. This is the case for the study presented by Gaspari and Ricci about a two-level airfoil optimisation, including the variation of a class shape transformation defined airfoil with a morphing leading and trailing edge [55]. The first step is determining the optimal aerodynamic shape, which is conducted with a method based on the subsonic 2D airfoil tool XFOIL [56, 57]. In the second step, skin stress is minimised, and internal structure is optimised. The EU project NOVEMOR extended the approach by integrating the PyPAD (Python-based Preliminary Airframe Design) framework, applying aeroelasticity tools and a panel code for aerodynamics [58]. The outcome is a conformal airfoil with variable leading and trailing edges. This process was subsequently extended further with the application of a RANS solver, which was reported on by Gaspari et al. in 2016 [59]. The produced conformal leading and trailing edges were integrated in an unswept wing section with a scale of 1:10 and tested in a subsonic wind tunnel. The result of the downward deployment of the trailing edge was an increase in the magnitude of the suction peak, while the deployment of the leading edge resulted in a backward shift of the peak.

In addition to an increase in the variety of applied methodologies, the types of devices have also diversified. An example is the application case of the trailing edge taps discussed by Mertens in 2001 [60]. While this thesis focuses on applying an ADHF, some application cases are relevant for VC-specific advantages. This is the case for Mertens comments on load distribution, where he argues that a passive application would keep an inboard shifted load distribution during an entire flight segment, where loads are very high (e.g. gusts) and the additional drag is not harmful. This would be the case for descent. For an active system, a sensor detecting gusts is required. This information makes a short-term redistribution with a respective short-term drag increase possible. This system is applied in the American B1 bomber for low-level flight. Furthermore, Mertens presents data from a wind tunnel study on an unspecified civil aircraft that yielded a 1.5 % increase in L/D for the application of VC and a further 2 % drag reduction by an 8 % decrease in wing area enabled by an increase of good performance over wider C_L-ranges and increase of buffet margin. It is important to note that the 8 % wing area reduction implies a redesign of the aircraft. In total, this resulted in a L/D improvement of 3.5 %, as shown in Figure 26.

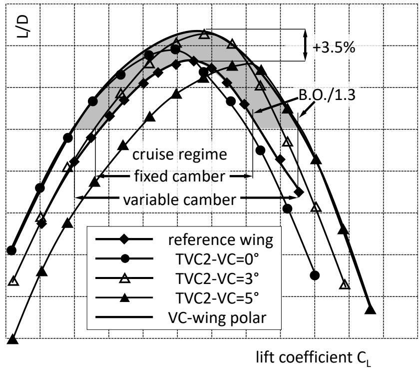

Figure 26: L/D improvement during cruise by VC application [60].

Another example of tab application was given by Dargel et al. in 2002, presenting results from the national Pro-HMS technology research program focusing on multifunctional control surfaces [61]. Amongst other applications, deploying tabs at the trailing edge control surfaces was analysed and proved effective for reducing wave drag for off-design points and increasing buffet margins when deployed globally. When deployed differentially, benefits for the induced drag were achieved.

NASA also used the widely available computation power and airfoil assessment methodologies. In a publication from 1999, Bolonkin and Gilyard use a combination of analytical and semi-empirical methods combined with wind-tunnel data to establish a database for a variable wing geometry application on the Lockheed L-1011 TriStar [62]. With this database, a theoretical L/D improvement for Ma 0.83 in dependence on C_L and camber variation (see Figure 27) was created. They deduct an L/D improvement of 1 – 3 % for the most relevant C_L segment (0.3 to 0.5) for cruise phase. These results again show the increased L/D improvement of VC for high C_L and the shifting cross-over point of best-performing airfoil going from low to high camber.

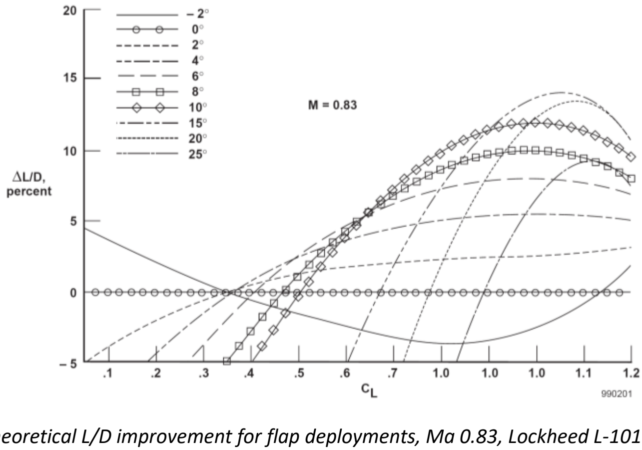

Figure 27: Theoretical L/D improvement for flap deployments, Ma 0.83, Lockheed L-1011 TriStar [62].

VC stayed in the research focus of NASA and was integrated into the NASA innovation fund project entitled "Elastically Shaped Air Vehicle Concept", presented by Nguyen in 2010 [63]. In this project, control surface setups were designed for a long-range aircraft concept, amongst other technologies. The deployment of the control surfaces shapes the highly flexible wing. Two setups that were investigated aimed towards achieving a seagull-shaped wing deformation. The first setup consists of six conventional flaps and slats each. The second setup is built of the same slats but 12 spanwise connected flaps that feature three hinge lines in the flap for smooth deformation (see Figure 28). The latter is called the Variable Camber Continuous Trailing Edge Flap (VCCTEF) concept. Nguyen states that the drag advantage of the VCCTEF compared to the conventional flap is up to 66 % for cruise lift coefficients due to the elimination of vortices generated by the gaps between conventional flaps [63].

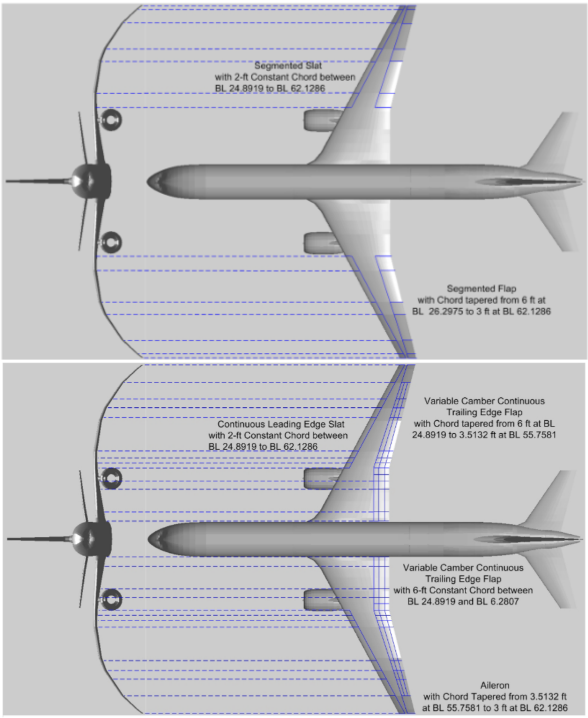

Figure 28: Conventional (top) and variable camber continuous trailing edge flap (bottom) control surface setup of the NASA Elastically Shaped Air Vehicle Concept project [63].

The VCCTEF concept was further investigated and integrated into other projects and aircraft studies. Urnes et al. reported on the "Fundamental Aeronautics Technical Conference" in 2012 about the integration of the VCCTEF concept in the Generic Transport Model (GTM), which is based on a Boeing B757 geometry [64]. The example data for the VCCTEF showed two-digit cruise drag savings. A description of the aerodynamic analysis method for this application case was given by Ippolito et al. in 2013 [65]. The analysis was applied to a rigid wing and conducted with a vortex-lattice method (VORLAX) at cruise conditions with several fuel loads. The results show a drag reduction of up to 9.8 %. A more detailed description of the geometric setup and the results of the application of a different vortex-lattice solver was given by Urnes and Nguyen in 2013 [66]. The setup of the VCCTEF system consists of 14 sections on the outboard wing and three sections on the inboard wing, all connected by 8-inch (20.32 cm) sections of flexible material for the GTM application case. Again, a vortex-lattice method was applied (Vorview). For an unconstrained movement of the single sections relative to each other, the induced drag reduction for 20 % fuel loading is 9.88 %; for a 2° constraint, the reduction is 5.71 %, and for a 1° constraint, it is 3.24 %. The reduction for an 80 % fuel load is 2.64 %, 2.38 % and 1.00 %, respectively. This is a noteworthy trend since the observation in the studies presented previously in this thesis shows a larger benefit for higher lift coefficients. The VCCTEF results presented here decrease with an increase in fuel load and hence with an increase in lift coefficient. However, it must be noted that the vortex-lattice method applied here does not account for any compressibility effects, which could strongly influence this trend. The results of Lebofsky et al. support this assumption for the same application case (i.e. the GTM) [67]. This study focuses on the effect of the VCCTEF application on a wing with decreased stiffness, employing a finite element analysis for the wing structure simulation. The baseline wing stiffness was calibrated to produce a wing tip deflection of 3 %. The reduced stiffness wing featured 50 % reduced Young's and shear modulus, leading to a wing tip deflection of approximately 6 %. In addition to the vortex-lattice method applied 2D data for the airfoil were calculated with the 2D compressible flow solver Cart3D. The two off-design cases (80% versus 20% fuel load) analysed in this study show a higher drag reduction for the higher-loaded case (20.4% drag reduction versus 7.8%). This indicates the importance of applying methods that consider compressibility effects for assessing VC, which is the main motivation for this thesis. Furthermore, it confirms the trend of the higher VC potential for higher lift coefficients from the previously discussed studies. The transonic nature of the application case of this study is further solidified in a numerical study of the VCCTEF concept presented by Kaul and Nguyen in 2014 [68]. This study applies the OVERFLOW code, which employs Reynolds-averaged Navier-Stokes (RANS) equations. The study concludes that with increased trailing edge deployment, the absolute drag increases while the lift increases as well. Furthermore, the study shows a stall of the deployed airfoils at a lower angle of attack. L/D is found to be increased for a cruise lift coefficient of 0.51 with all deployed airfoils, but the most deployed one, which featured a deployment angle of 6 °. An analysis of the pressure distribution showed shocks for all deployed airfoils at the first hinge line of the flap. In cooperation with Boeing and other partners, the integration of VCCTEF in the GTM model was part of an extensive research project with NASA, presented by Nguyen et al. in 2015 [69]. The numerical aerodynamic analysis followed a similar approach to the study presented by Lebofsky, employing the RANS solver OVERFLOW combined with VORLAX. Again, this study showed a higher drag reduction for increasing C_L. The overall aircraft drag saving for the baseline stiffness wing is 2.6 % for an 80 % fuel load whilst increasing to 4.6 % for a 30 % C_L increase. During this project, the high lift capability of the VCCTEF was also analysed. The GTM VCCTEF model was tested at the University of Washington Aeronautical Laboratory, and the results were presented by Nguyen et al. in 2015 [11]. The tests proved the high lift performance would be sufficient for a B757-like aircraft. The VCCTEF is currently one of the key components of NASA's Transonic Truss Braced Wing (TTBW) concept [70]. The TTBW is applied to a Boeing B737-sized aircraft and features a wing with an aspect ratio in excess of 19. This slender wing requires technologies to mitigate its high bending moments. As clear from the name, trusses are included in the concept for this purpose. In addition, aeroelastic control using VCCTEF is incorporated, as presented by Bartels et al. in 2019 [71]. The transonic nature of the application requires a specific consideration of compressible effects. In 2021, Xiong presented the methodological setup for the transonic assessment of VCCTEF on the TTBW [72]. In this study, MSES was used to assess 2D airfoil characteristics similar to those applied in this thesis. However, the trailing edge devices were split into six spanwise sections. The results of this approach were compared to RANS calculations and found to have a good agreement in pressure distributions and "key aerodynamic parameters". The drag reduction results ranged from 0.77 % to 2.24 %, depending on the lift coefficient.

Reist et al. 2022 [73] presented an ADHF application on a business jet and analysed it with a RANS flow solver. The results showed an increased deployment for higher lift coefficients for the wing. Drag reductions by the application of VC differed from 35 % for a non-optimised wing and 1-5 % for a wing optimised before the application of VC. This emphasises the need to optimise the wing, specifically the lift distribution, using a homogenous method for the VC assessment.

In summary, VC has been thoroughly researched in the aviation research community with varying applied methods and benefits predictions. To give an overview, Table 1 lists the aircraft performance increase predictions found in the previously discussed literature.

Table 1: Summary of VC aircraft performance increases in literature

Source	application case	aerodynamic method	VC improvement
Ferris 1977 [17]	generic wing 35° sweep	wind tunnel data	L/D: 19 – 35 %
Gilyard and Espana 1994 [24]	AFTI	flight test data	L/D: 8 – 20 %
Boeing 1980 [27]	intercontinental civil	"combination of wind tunnel and analytical data"	mission fuel: typical 3.1 %, design 4.2 %
	domestic civil		mission fuel: typical 4.0 %, mission 1.5 %
Hilbig 1984 [30]	civil aircraft	wind tunnel data	L/D: 3 %, fuel: 5 %
Szodruch 1988 [33]	civil aircraft, retrofit	not specified	wing L/D: 1.5 %
	civil aircraft, clean sheet		wing L/D: 3 – 9 %
Greff 1990 [37]	civil aircraft	not specified	L/D: 4 %
Fielding and Vaziry-Zanjany 1996 [8]	Airbus A340	not specified	L/D: 2.3 %*, mission fuel: design 6 %
Merterns 2001 [60]	civil aircraft	not specified	L/D: 3.5 %
Bolonkin and Gilyard 1999 [62]	Lockheed L-1011 TriStar	analytical equations based on flight test data	L/D: 1 – 3 %
Ippolito et al. 2013 [65]	Generic Transport Model	vortex-lattice method	L/D: 9.8%
Nguyen et al. 2015 [69]	Generic Transport Model	RANS	L/D: 2.6 - 4.6 %
Xiong 2021 [72]	Transonic Truss Braced Wing	2.5D	L/D: 0.8 - 2.2 %
Reist et al. 2022 [73]	business jet	RANS	L/D: 1 - 5%

*computed with assumptions in this thesis

3 Method for Variable Camber Assessment in Conceptual Aircraft Design

This section describes the methods devised to achieve the goals of this thesis. This includes a description of the integration into the existing aircraft design framework and a short presentation of the most relevant components.

3.1 MICADO

The interdependent and interdisciplinary nature of the calculations that must be performed for conceptual and preliminary aircraft design requires the application of a capable framework. At the Chair and Institute of Aerospace Systems (German: Institut für Luft- und Raumfahrtsysteme, ILR) of RWTH Aachen University, a design environment has been developed with the goal of fast aircraft design based on TLAR and optimisation for conventional aircraft. This framework is called Multidisciplinary Integrated Conceptual Aircraft Design and Optimization (MICADO) [74, 75]. MICADO contains a variety of modular tools, which are based on handbook methods (e.g. Raymer [76], Roskam [77] and Torenbeek [78]) as well as analytical methods (e.g. lifting line - LILI [79]). The modular nature of MICADO is an advantage for this thesis since it allows for the easy selection of relevant tools during the study's execution. The following sections will discuss the general structure of MICADO and the modules that are important for this thesis. For an overview of other aircraft design tools, the dissertation of Böhnke is recommended [80].

3.1.1 Overall Process

The overall process of MICADO is structured to facilitate a balanced conceptual and preliminary aircraft design with only the TLAR as input. MICADO features a modular structure of tools implemented in C++, mainly exchanging information via the ´aircraft.xml´ file. This file contains all main aircraft data (e.g. geometry, masses, etc.); additional xml-files contain the aerodynamic aircraft polars and the propulsion performance maps. The architecture of MICADO is shown in Figure 29. Starting from the user-defined TLAR and the selected configuration specifications of the aircraft, the MICADO environment first performs the ’Initial sizing’, estimating initial values for thrust/weight ratio (T/W), wing loading (W/S) and Maximum Take-Off Mass (MTOM), and subsequently the “Fuselage Design” creating the fuselage geometry based on passenger classes, seating configuration and number of seats. These two modules are executed before entering the iterative design loop. The first category of modules in the design loop is ’Aircraft Sizing’, in which the geometry of the structural components is set up, and the propulsion performance maps are scaled for the respective T/W. The created aircraft is then analysed using the modules of the ´Detailed Design´ category, enabling the additional synthesis of flight controls, subsystem architecture, and component mass estimation. The ´Aircraft Performance Analysis´ category contains aerodynamic, structural, and mission tools for estimating the aerodynamics, masses, and, ultimately, the fuel consumption of the aircraft during the design mission and, optionally, other missions. This design procedure is carried out in an iteration loop until convergence in specified main design parameters (e.g. MTOM, block fuel, etc.) is achieved. After convergence, the design is checked against the TLAR, and it is reported whether the assumptions made led to a valid design. If a valid design is created, it is analysed by the modules in the ´Design evaluation´ category. This analysis can include non-technical parameters such as cost, life cycle cost, climate impact, and noise. With a dedicated parameter study manager module, parameter variations allow for assessing and optimising the design.

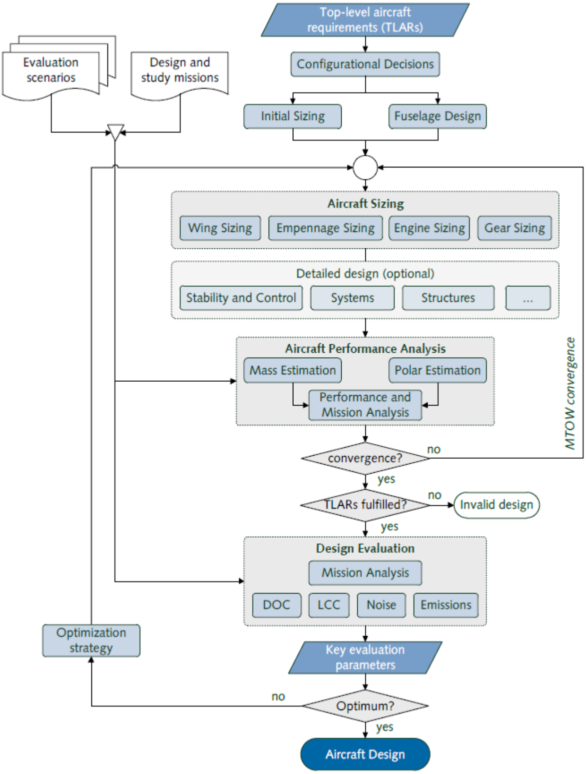

Figure 29: MICADO architecture [74].

The scope of this thesis focuses on the aerodynamic performance of a VC system and its impact on the mission fuel burn. Hence, the modules described in more detail in the following sections are the aerodynamic module, “calculate polar”, and the “mission analysis” module.

3.1.2 Aerodynamic Analysis

The aerodynamic analysis is the central aspect of this thesis, and the multi-fidelity approach implemented in MICADO will hence be described in more detail. This includes the overall aircraft polars, the wing polars and the airfoil polars and their respective integration.

3.1.2.1 Calculate Polar

The module for creating the overall aircraft aerodynamic polars is called "calculate polar". This module can estimate a conventional aircraft's lift, drag and moment based on wing configuration (take-off, cruise and landing) and flight condition. With this information, trimmed aircraft polars are produced that provide the aircraft drag, i.e. the total aircraft drag ($C_{D,total}$) is provided as a function of C_L, Ma, Re, wing geometry and aircraft configuration, as described in Equation (2).

$$C_{D,total} = f(C_L, Ma, Re, wing\ geometry, aircraft\ configuration) \tag{2}$$

In order to reach a converged solution on a personal computer in minutes, a fast and stable determination of the aircraft polars, which can be executed several times during the design loop, must be ensured. For this reason, "calculate polar" offers different methodologies for specific aircraft components that can be selected as the study at hand requires. The semi-empirical methods used in MICADO are generally implemented in "calculate polar" itself. The application case in this thesis focuses on the wing's aerodynamics. Therefore, the drag components due to inviscid flow that are not impacted (i.e. fuselage, nacelles and empennage) are calculated based on a component build-up as suggested by Raymer [76]. The lift and lift-induced drag are computed using the methods of Torenbeek [78] and Roskam [77], respectively. A more detailed description of the structure of the calculate polar module is given by Lammering et al. [81]. For this thesis, the aerodynamic focus is on the wing, and the principle setup is based on the approach developed and applied by Risse [75]. The assessment methods for each component and resulting aerodynamic coefficients are listed in Table 2, where C_M, $C_{D,ind}$, $C_{D,visc}$ and $C_{D,wave}$ are the coefficients for pitch moment, induced, viscous, and wave drag, respectively.

Table 2: Aerodynamic coefficient prediction methods for components based on [75]

Component/Coefficient	**C_L**	**C_M**	**$C_{D,ind}$**	**$C_{D,visc}$**	**$C_{D,wave}$**
Wing	LILI	LILI	LILI	MSES	MSES
Horizontal tail plane	LILI	LILI	LILI	semiemp.	semiemp.
Vertical tailplane	-	-	-	semiemp.	semiemp.
Fuselage	LILI	semiemp.	semiemp.	semiemp.	-
Nacelles	-	semiemp.	semiemp.	semiemp.	-

A trimming function is executed during the design loop for a point in the middle of the cruise segment, changing the angle of incidence of the horizontal tail plane to achieve a trimmed flight state. This limits the representation of trim drag, which is impacted by the VC incorporation. However, according to the literature, this effect is small (see section 2 and [37] specifically). The applied trim results are considered in "calculate polar", which produces trimmed aircraft polars. The following sections will describe the modules and methods in more detail.

3.1.2.2 Lifting Line

For the calculation of the induced drag, pitching moment, and lift coefficients (total and spanwise sections) of the lifting surfaces (i.e. wing and horizontal tailplane), the DLR multiple lifting-line code LIFTING_LINE (LILI) [79] was incorporated in MICADO. LILI employs potential theory and solves a vortex system for the wing surface split into panels. LILI can process multiple and non-planar lifting surfaces.

An advantage over conventional vortex-lattice methods is that the circulation along a vortex in a spanwise direction is not constant due to introducing a predetermined quadratic function. This reduces the number of required vortices along the span and increases the accuracy of induced drag prediction. The lift distribution of LILI was shown to be comparably accurate to results calculated by RANS by Liersch and Wunderlich [82]. The calculation of the spanwise lift distribution is, next to the induced drag, the major output for the applied aerodynamic setup in this thesis. The local lift coefficients from this distribution will be used as an interface for the 2D airfoil aerodynamic data.

The method implemented in MICADO for incorporating LILI implies a continuous geometry between wing segments. This is incompatible with discontinuities, e.g. small gaps between control surfaces or wing segments, in a spanwise direction. The gap between the inboard flap and the outboard flap of the reference aircraft, especially if the flaps are deployed differently, is such a gap and cannot be assessed with the current state of the methods in MICADO. Additionally, NASA studies have shown a great drag reduction potential for applying continuous trailing edge flaps as the VCCTEF (see section 2) [63]. For this purpose, an adaption of the wing geometry of the selected reference aircraft is required, and a continuous transition between the airfoils of wing segments is mandatory, which will be described in section 4.1.2.

The method LILI is based on can neither consider compressibility effects nor does it take the airfoil geometry into account beyond the application of its skeleton line. While for standard cases, compressibility effects can be accounted for with Göthert's 3D extension [83] of the Prandtl–Glauert rule [84, 85], applying VC requires a more analytical approach sensitive to small airfoil geometry variations. Hence, for this thesis, LILI must be augmented by a more sensible method for these aspects, described in sections 3.1.2.3 and 3.1.2.4.

3.1.2.3 Quasi Three-Dimensional Framework

A major reduction in complexity and computational effort is achieved by reducing the problem analysed with higher-order methods from 3D to 2D. One approach to facilitate this is applying a quasi-three-dimensional (Q3D or 2.5D) process, enabling the application of higher-order methods to 2D airfoils. Risse accomplished the required implementation in a Q3D framework as part of his dissertation [75]. A central part of the Q3D framework is the transformation from 3D to 2D and vice versa. For this, Risse employs the Simple Sweep Theory (SST), which is based on the early theories of Busemann [86]. As described by McLean, the SST is based on the assumption that certain flow properties (e.g. compressibility effects) are strongly correlated with the Ma perpendicular to the lines of constant pressure on a swept wing (i.e. isobars) [87]. As McLean states, SST cannot predict drag effects but does allow valuable conclusions with respect to lift. With SST, equivalent 2D flow conditions can be estimated for given 3D values by applying equation (3) for Ma and equation (4) for C_l.

$$M_{\infty,2D} = M_{\infty,3D} * \cos\varphi_{ref} \tag{3}$$

$$C_{l,2D} = \frac{C_{l,3D}}{\cos^2\varphi_{ref}} \tag{4}$$

The reference sweep angle is ϕ_{ref}. For subsonic applications, ϕ_{ref} can be substituted with the quarter line sweep angle ($\phi_{1/4}$), while it has been proven to be more suitable for transonic flow to use the sweep angle at the shock position [88].Equations (3) and (4) will be used in section 4.1.3 to assess the suitability of airfoil performance based on 2D data derived for the 3D flow conditions of the reference aircraft.

For the analysis of tapered wings, an SST extension called sweep-taper theory was developed, which is based on research of Lock [89] and was applied by Boppe [90] during the program of the X-29A aircraft (see section 2). It is best explained with the conical wing concept, displayed in Figure 30. Here, the local sweep angles are marked with ϕ and carry the chord position (i.e. leading edge (LE) and trailing edge (TE)) as subscript. The freestream conditions Ma and the velocity U carry the subscript ∞, while the subscripts Φ and r represent the polar and radial angle in the conical wing plane, respectively.

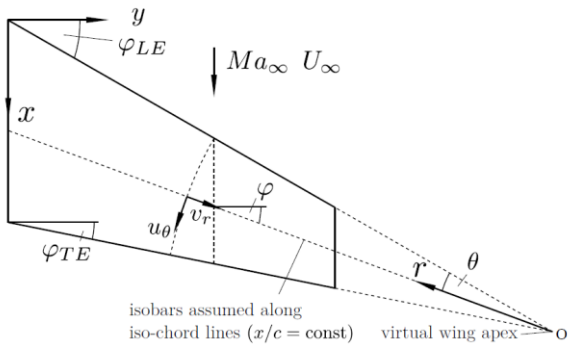

Figure 30: Conical flow assumptions on a tapered wing segment [75].

Next to the flow condition, the airfoil geometry must also be transformed according to the terminology used for conical wings introduced by Kaups and Cebeci [91]. This thesis focuses on the derivation of deployed airfoil geometries in 2D. Hence, the relations from Risse [75] are rearranged to produce 3D values for the airfoil geometry for a 2D input. The relation of the local thickness of an airfoil, normal to the wing leading edge, is given by equation (5), where z is the local thickness and c is the chord.

$$\left(\frac{Z}{C}\right)_{3D} = \left(\frac{Z}{C}\right)_{2D} * \cos\varphi \tag{5}$$

For the tapered wing, ϕ is a function of the position along the chord line and is defined by equation (6), where x is the local coordinate along the airfoil chord line in the x-direction.

$$\tan\varphi = \tan\varphi_{LE}\left(1-\frac{x}{c}\right) + \tan\varphi_{TE}\frac{x}{c} \tag{6}$$

The combination of equations (5) and (6) produces equation (7), which will be used to transform the assessed 2D airfoils into the 3D shape that will be integrated into the 3D wing geometry.

$$\left(\frac{Z}{C}\right)_{3D} = \frac{\left(\frac{z}{c}\right)_{2D}}{\sqrt{1+\left[\tan\varphi_{LE}\left(1-\frac{x}{c}\right) + \tan\varphi_{TE}\frac{x}{c}\right]^2}} \tag{7}$$

3.1.2.4 MSES

As discussed before, the solid assessment of the effect of airfoil modification in the transonic regime requires an analysis method that is able to capture compressibility effects sufficiently. While applying the full Navier-Stokes equations is impractical, using RANS has become affordable enough in terms of computational effort to be executed on personal computers. However, the application in conceptual aircraft design requires a flexible and stable method that has not yet been reached by RANS, especially with the persisting challenges connected to creating and preparing functional calculation meshes. The Navier-Stokes equations are further simplified if the viscous terms are neglected, providing the Euler-Equations [92]. Drela developed such a 2D Euler-Equation-based method in his PhD in 1985 [93], which became the MSES tool after further development [94, 95]. For the incorporation of viscous effects, MSES combines several methods and the viscous-inviscid interaction is incorporated by applying the displacement thickness [96].

In the approach developed by Risse at the ILR, MSES calculation results for predefined airfoils are stored in a database and accessed during the design loop with the LILI results for the local lift coefficients as input. While MSES is more stable and faster than RANS, it still is not well suited for direct execution in the design loop. The usage of a database for the predefined airfoils, as well as flow conditions, mitigates this problem. The database and its capabilities in interpolation between specific airfoil geometries are described in more detail by Schültke and Stumpf [97]. This includes interpolating different laminar-turbulent transition positions along the chord length. In this thesis, all results imply fully turbulent flows.

3.1.3 Mission Analysis

The MICADO "mission analysis" module utilises the data calculated in the design loop (mainly aircraft mass, aerodynamic polars and engine performance maps) to simulate either the design or an off-design mission of the analysed aircraft. Only a short description will be given in this thesis, focusing on the relevant aspects. Anton et al. give a more detailed description [98]. For different flight phases (i.e. accelerated climb or descent, constant speed climb, level flight and constant speed descent), the equations of motion are solved, and the optimisation problem of energy is solved iteratively to determine the required thrust and resulting fuel flow. This process is undertaken for each mission increment (per default 2 nmi), produced by splitting up the mission. An alternative strategy for a more detailed control strategy analysis for thrust in combination with VC, Renken suggested a concept taking the interaction of engine control and drag slope into account [26]. The fuel flow is added up by the "mission analysis" module to calculate the actual mission fuel. The fuel mass at the start of the mission is either a result of the previous instance of the design loop or a Breguet Range Equation estimate. Equation (8) shows one form of the Breguet Range Equation in which g is the gravitational acceleration of Earth, SFC is the specific fuel consumption, L/D characterises the aerodynamic efficiency, and m is the aircraft mass at the start and end of the mission, respectively.

$$Range = \frac{U}{g}\frac{1}{SFC} * \frac{L}{D} * ln\left(\frac{m_{start}}{m_{end}}\right) \tag{8}$$

Several aspects of the mission can be optimised during the mission simulation; the two attributes of importance for this thesis are the ICA and the execution of flight level changes. The underlying figure of merit for evaluating these two procedures is the Specific Air Range (SAR), shown in equation (9), where TAS stands for the current true airspeed [99].

$$SAR = \frac{TAS}{SFC} * \frac{L}{D} * \frac{1}{m * g} \tag{9}$$

For example, for flight level changes, the SAR is calculated once for the current altitude and once for the altitude obtained when performing a climb step. If an advantage for a flight level change regarding SAR is found, equation (8) estimates whether the climb step is advantageous. If the fuel needed for the remaining part of the cruise flight at the current altitude is greater than the fuel required for performing, e.g., a 2000 ft climb step plus the remaining part of the cruise flight, then a climb step should be performed. If the decision is made to perform a climb step, an additional check is carried out to ensure that the aircraft's maximum operating altitude is not exceeded. It is crucial for the transparent analysis of the effects of technologies to distinguish fuel mass changes due to mission profile changes and changes caused by a different point performance. Therefore, during the execution of the application in this thesis, the optimisation function of "mission analysis" will be activated after analysing the results for a predetermined fixed trajectory.

3.2 Incorporation of Variable Camber in MICADO

The components of MICADO described so far are part of the default aircraft design routine. This section presents the general approach and the tools created for this thesis. Figure 31 shows the general concept of VC incorporation in MICADO. The geometry preparation is described on the left side of Figure 31. The "Control Device Airfoil Generator" (CDAG) module extracts the spoiler and flap plan-form information for a specific wing section from the aircraft.xml file. The CDAG then incorporates the ADHF kinematics and creates the deployed airfoil geometries. Subsequently, the 2D deployed airfoils are transformed into 3D airfoils and incorporated into the 3D wing geometries with all deployment permutations, meaning different deployments of, e.g. the inner and outer flap of the wing. In the middle of Figure 31, the aerodynamic processing is presented. The created deployed 2D airfoils are analysed with MSES, and the results are stored in a database. During the application of "calculate polar", LILI is executed, and the database is accessed with the Q3D framework, applying the SST and producing an overall aircraft polar. This process is repeated for all ADHF deployment permutations, creating a group of aircraft polars. The right side of Figure 31 shows the integration into the mission assessment. The group of aircraft polars is processed with the "polar merger" module, which selects the best L/D for each polar point of the aircraft polar while storing the respective ADHF deployment settings. This merges the group of aircraft polars into one aircraft polar with the best L/D envelope. The "mission analysis" module then executes the mission simulation, during which the tracked ADHF deployment settings can be displayed, representing the ADHF deployments used at specific mission points. Subsequently, an analysis accounting for fuel planning considering a VC malfunction at particular points of the mission based on the ETOPS concept is conducted.

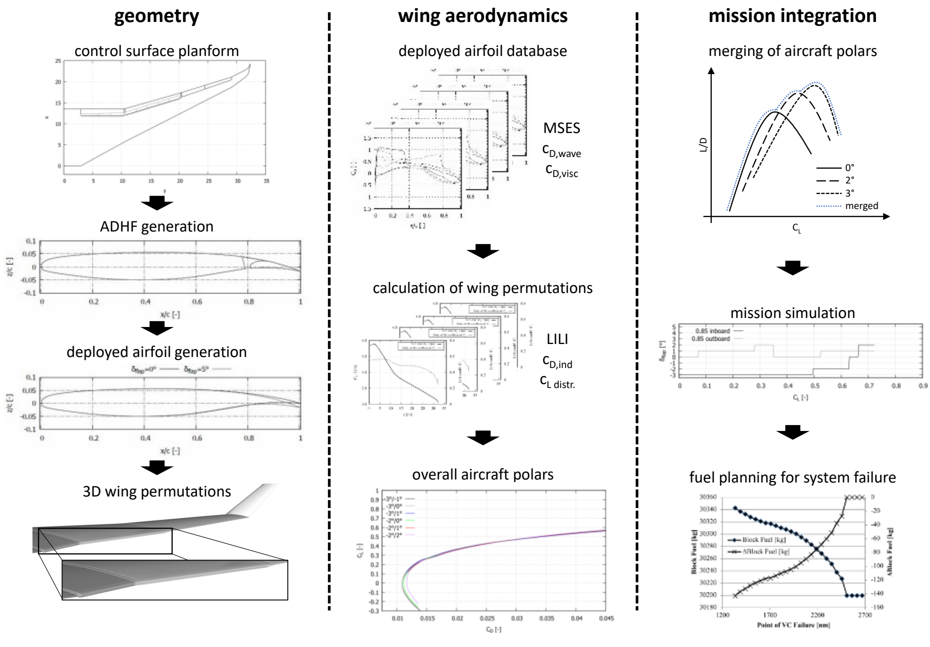

Figure 31: Concept of the variable camber incorporation in MICADO.

The following sections describe the modules required for this methodology and implemented for this thesis in more detail. The execution of the modules on the application case is then part of section 4. More specifically, the geometry derivation (left column in Figure 31) is described in section 4.2.1, the aerodynamic assessment (middle column in Figure 31) in sections 4.2.2 through 4.3.2 and the integration on aircraft and mission level (right column in Figure 31) in section 4.4.

3.2.1 Variable Camber Airfoil Geometries

The airfoils currently used in MICADO are defined without separate control device coordinates. Flaps and other control devices are described within another section of the aircraft.xml, but only their plan-form and maximum deployment angles are given. The corresponding airfoil coordinates (if such devices were to be deployed) are not defined. The geometry and kinematics of high-lift devices can be complex. Rudolph gives a detailed description of a large number of high-lift devices employed by large airliners [9]. For the specification of the movement of a commonly used fowler flap, either a complex track geometry or the kinematic interaction of the support bars has to be known. The ADHF is much more easily specified, i.e. the possible position of the flap element is determined by the pivot point's position and the deployment angle, as is the case for the spoiler, as shown in Figure 32.

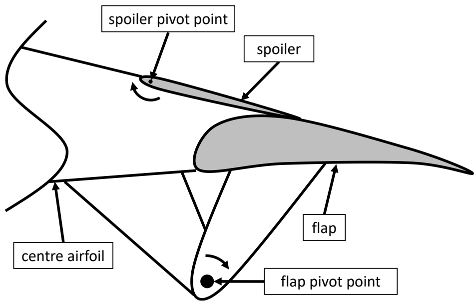

Figure 32: Idealized adaptive dropped hinge flap concept.

This comparable simple geometric definition motivated the concept of this thesis to implement an automated derivation of the ADHF kinematic with only the spoiler and flap plan-form (i.e. the outer shape projected from a top-view) as input and predetermined relative values for the pivot point positions and a few other generalised parameters. The approach presented here is the best estimate of an ADHF geometry derived from the limited data available in the public domain.

The CDAG aims to define control device airfoil coordinates when at 0°-deployment position based on an automated method. After that, the control device airfoil coordinates for deployed positions are determined. The current implementation is tailored for the use within this thesis, meaning that only an ADHF is available as a control device type and only for the application as a VC system, meaning it is not used for high-lift assessment. The process only considers the existence and generation of the corresponding components. However, additional control devices (such as slats, fowler flaps or ailerons) can be implemented, and the program structures are planned with such an extension in mind.

The derivation of the flap airfoil is based on the approach presented by Dorbarth [100] and defines a cut-out from the parent airfoil. The developed process is based on a few characteristic points around the parent airfoil and flap. These points are shown in Figure 33. In common with Dorbath [100] is applying an ellipsis to define the flap’s upper curvature and leading edge. The necessary input from the plan-form of the flap and spoiler is the leading and trailing edge position. The point declared with “1” in Figure 33 is defined by the trailing edge of the spoiler; thus, the x- and z-coordinate can be directly extracted from the parent airfoil. Furthermore, the gradient at point 1 is calculated by calculating the slope to the next point towards the airfoil trailing edge. The x-coordinate of point 2 is defined by the flap's leading edge, known from its plan-form. As explained later in this section, the z coordinate is derived from existing flap geometries. The gradient of point 2 would be infinite by definition as it is the most forward point. Therefore, a high value (i.e. 99999.0) is used. Point 3 represents the change in curvature from the leading edge ellipse to the flap's lower side and is derived in dependence on point 2, which will be explained later in this section.

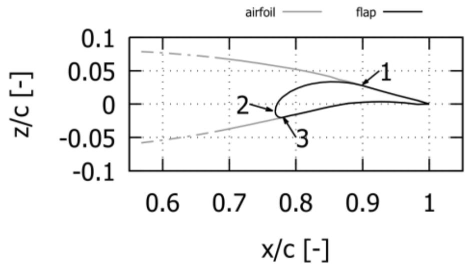

Figure 33: Characteristic points of the flap definition.

For points 2 and 3, estimates must be made from existing flap geometries. Rudolph [9] presents the cross-section of an Airbus A320, Boeing B777 and B757 flap airfoil, shown in Figure 34.

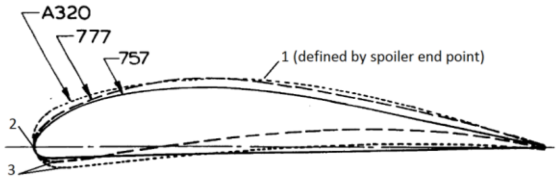

Figure 34: Examples of flap cross sections by given by Rudolph [9] with characteristic flap points.

From the flap cross-sections in Figure 34, the following default values have been derived:

- Point 3 x-position
  Distance from the flap leading edge to point 3 relative to the flap chord: 0.05
- Point 3 z-position
  Is determined by the parent airfoils geometry
- Point 2 z-position
  Distance perpendicular to the chord between point 3 and point 2 in relation to the flap chord: 0.03

With these assumptions, the flap geometry is completely defined. As the flap must represent the parent airfoil aft of point 1, the flap coordinates from this point towards the trailing edge are easily found. From point 2 towards point 1, the equations for an upper-sited ellipse are solved and based on its centre and halfaxes, the corresponding flap coordinates are calculated. The flap's upper surface coordinates are determined with the coordinates determined above. The same procedure is applied from point 3 to point 2.

While the upper side of the spoiler is identical to the parent airfoil, the lower side needs to be constructed. Here, Dorbarth [100] suggests a horizontal line at the z-coordinate of the spoiler trailing edge. This would produce a very thick spoiler. Instead, a thin plate is judged to be more representative of real aircraft spoilers. It is implemented and defined by a predetermined relative thickness in relation to the local airfoil thickness (default is set to 0.02).

A section in front of the flap and spoiler must be defined for the deployed airfoil's complete definition. The three components (i.e. centre, flap and spoiler airfoil) are shown in Figure 35.

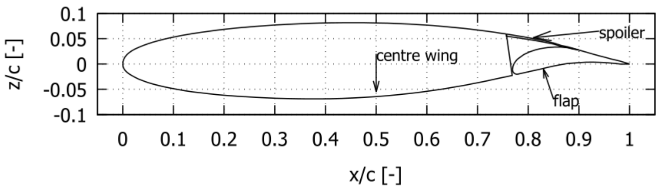

Figure 35: Parent airfoil with derive ADHF components.

For the centre airfoil, the lower side parent airfoil coordinates are adopted as close as possible to the flap leading edge when retracted. Concerning the upper surface coordinates, the parent airfoil coordinates are taken over until the spoiler's leading edge point. Closing of the centre wing airfoil is then achieved by connecting the lower surface's last coordinate point to the lower coordinate point at the upper surface, i.e., the spoiler leading edge, thereby completing the centre airfoil.

Although MSES can calculate multi-element airfoils, it was decided to create a single, closed airfoil from the created segments for simplicity. Therefore, gaps must be closed with auxiliary lines. The centre wing is connected with a horizontal line to the flap airfoil. The same approach is executed for the upper side from the centre airfoil to the spoiler leading edge. Although this appears crude, it should be noted that, especially for the sensitive upper side, the gap, and hence the length of the horizontal line, is comparably small. After the deployed airfoil geometries are created, the three components are merged into a combined airfoil geometry and written as output to a new file. This approach was implemented in the CDAG during the master thesis of Boever [101]. The minimal and maximal deployment angle and increment can be specified in the CDAG settings file. During the flap deployment, the spoiler follows the flap segment with a contact condition. It must be mentioned that this approach neglects the chord variation of the airfoils. A detailed study of the impact of camber variation by Mantel did not show a strong influence of the variation in camber [28]. The chord variation in this thesis's application case, presented in section 4.2, is in the order of 0.5% resp. 0.7%. Recent studies at ILR have shown that this change has a negligible effect on performance.

After the concept of the geometric derivation was described, the CDAG's implementation is now discussed. The structure of the CDAG follows the MICADO module standards and is implemented in C++, therefore using an object-oriented programming style. The CDAG focuses on the geometry and the coordinates of the control devices. Thus, a basic class called *airfoil* is defined and represents a new type that can be used. This class only contains two arrays representing the upper and lower surface coordinates (data type 'Vec3'). The original 2D wing airfoil that will be read in and the centre wing airfoil that will be determined are two instances of the *airfoil* class. Using inheritance, two classes (*ADHFAirfoil* and *spoilerAirfoil*) are created, as shown in Figure 36, including additional parameters as the characteristic points discussed earlier in this section. Furthermore, these classes comprise arrays that store the deployed airfoils' coordinates and the corresponding deployment angle information. In the following diagrams and this thesis, the term "deflected" is understood as a synonym for "deployed".

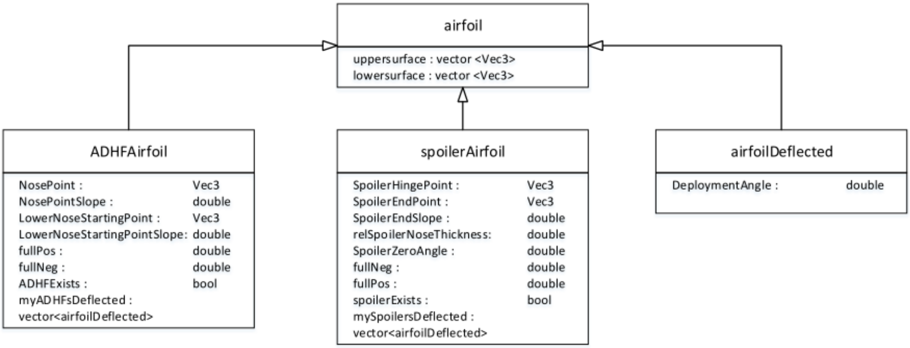

Figure 36: Airfoil class data structure.

The CDAG can process multiple wing sections during one execution, creating instances of the spanPosition class (see Figure 37). Besides the spanwise position, this class also contains different airfoil objects declared earlier. It thus also holds the information about the airfoil surface coordinates at the respective span location. Furthermore, the class *span position* possesses the arrays, including the merged/fused airfoils in the dedicated class *fusedAirfoil*.

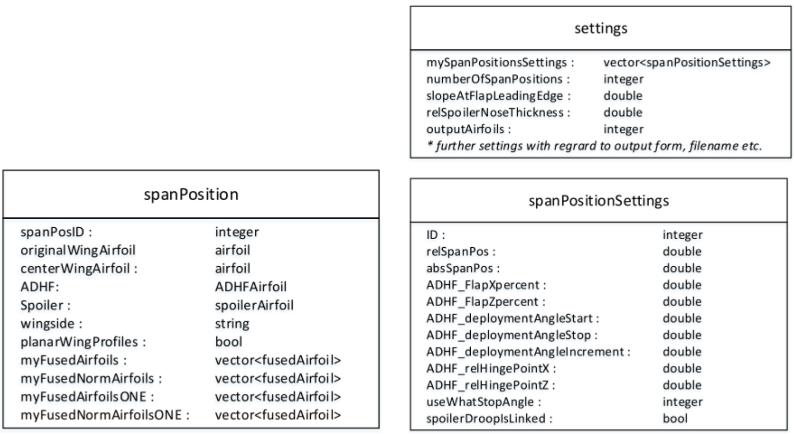

Figure 37:Data structure of the spanPosition class.

To create the different deployed control device airfoils, the *fusedAirfoil* objects contain the product of the merging of the constant *centerWingAirfoil* and the deployed segments with the auxiliary lines.

As is the standard in MICADO, the input data are stored in the settings xml-file, named after the module (i.e. ControlDeviceAirfoilGeneration.xml). For the CDAG, the most relevant data are the link to the target aircraft.xml file, the default values necessary for determining the characteristic points as discussed above, and the spanwise positions with the specification of the deployment angles. These values are mirrored in a respective settings class. During the runtime of the CDAG, this information is used to initialise the span positions, as shown in Figure 38.

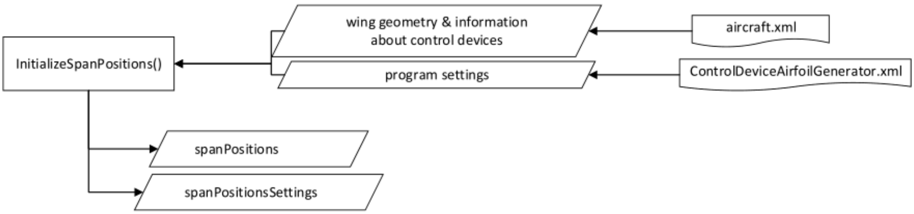

Figure 38: Initialization of the span position objects.

The construction of the ADHF kinematic is displayed in Figure 39. It starts with reading in the original airfoil at each specified span position, which is achieved by using a function already implemented in the geometry classes of MICADO. The CDAG checks the existence of the required control devices to create an ADHF kinematic in the aircraft.xml file at each span position and proceeds accordingly with the creation of the characteristic points and component coordinates.

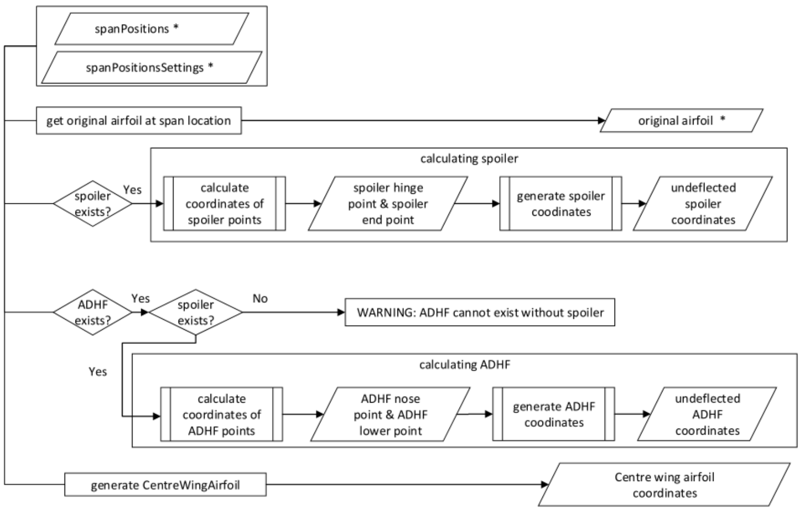

Figure 39: ADHF kinematic generation in the CDAG.

After the creation of all ADHF components, a function is executed that applies a rotational matrix calculation, taking into account the defined hinge points, to create the deployed airfoils (see Figure 40) in accordance with the deployment angles from the settings class for the specific span positions. For the spoiler tracking of the dropped hinge flap segment, the maximum z-coordinate of the flap is used.

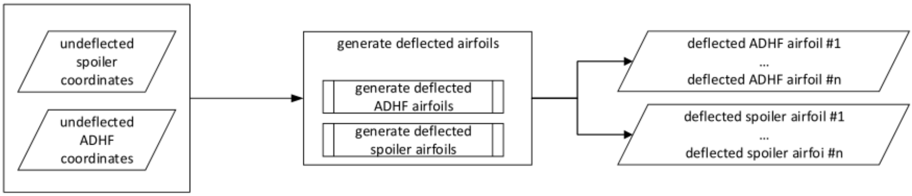

Figure 40: Creation of the deployed airfoils.

The created separate component airfoils offer the potential for different analyses. If stored separately, they can be used to calculate the individual aerodynamic load on each component. This approach was used in a research project at the ILR to size a simplified beam model of the ADHF kinematics with loads calculated in AVL [102]. For the application in MICADO as a VC system, they are merged into one airfoil. The point distribution of the direct CDAG output is not ideal for the analysis in MSES and has been shown to have an undesirable convergence behaviour. To mitigate this, the airfoil coordinate resolution is redistributed with the XFOIL tool, adjusting point density based on curvature change [57].

3.2.2 Polar Merger

The main output of the “calculate polar” module is the polar.xml file, in which the overall aircraft polars are stored in a hierarchical tree structure for each 3D wing geometry with its respective ADHF deployment permutation. The group of overall aircraft polars produced by “calculate polar” for the deployment permutations show different performances (i.e. overall aircraft L/D) for various flight conditions. In section 2, this has been stated by several previous researchers (e.g. see Figure 22). An algorithm could be devised that selects the best ADHF deployment combination during the execution of the mission simulation. However, this would require storing and exchanging all aircraft polars between the ”calculate polar” and “mission analysis” modules. Furthermore, it would necessitate an additional action at each mission increment to select the best-suited deployment configuration, thereby increasing the computational effort of the mission simulation. Therefore, the author decided to extract this process from the mission analysis and instead compile a single merged aircraft polar from the group of aircraft polars. The concept is idealised visualised in Figure 41. The merging can happen based on different strategies, selecting the polar with the best overall aircraft L/D being the most straightforward. For each point (i.e. C_L, Re and Ma) of cruise configuration segment of each polar, all polars of the permutation group are compared, and the dataset (i.e. C_D, C_M and deployment information) with the lowest C_D is transferred into the merged polar.

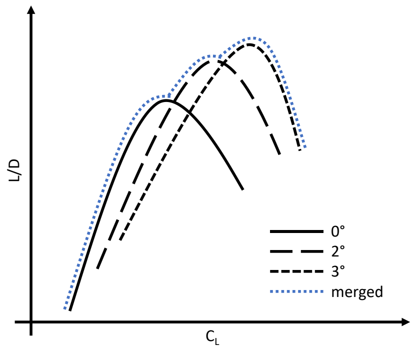

Figure 41: Concept of polar merging.

This concept was implemented in a module called “polar merger” and has been described in more detail in a prior publication by the author [2]. This module is not part of the design loop but is executed manually and outside of the design loop after all overall aircraft polars have been produced. During the subsequent execution of the design loop, the polar set created by the “polar merger” is used. This approach minimises the modification in the “mission analysis” module required for the VC integration. It only contains the tracking and graphical output of the specific ADHF deployment for the particular mission increments.

During cruise flight, cases can occur where a C_L is required that does not specifically exist in the polar file: e.g., a C_L of 0.43589 may be calculated, but only 0.434 and 0.436 exist in the polar file. The problem encountered at this point is the interpretation of the ADHF setting that would be required. It is simple to interpolate the corresponding C_D of the aircraft at that point, but the question arises as to whether an interpolated ADHF setting is sensible. The difference between the required C_L to the next smaller and the greater CL existing in the polar file will be calculated to avoid this ambiguity. The ADHF setting of the data set with the smaller difference is then used.

3.2.3 System Failure Integration in Operational Mission Planning

In case of a VC system malfunction, the aircraft's drag will increase, at least for some parts of the remaining mission. The consequence is an increase in fuel consumption. Hence, the safety considerations for VC go beyond airworthiness and must be incorporated in the mission and fuel planning, and possibly accounting for additional reserves. Therefore, a dedicated analysis of the drag increase due to a VC system malfunction is required. The ETOPS procedures are a suitable analogy, while certain aspects differ. The approach presented herein has been previously published by the author [2].

The operational framework of ETOPS offers a valuable context for evaluating the implementation of morphing technology systems. Introduced in 1985, ETOPS regulations permit certified twin-engine aircraft to operate routes where a suitable alternate airport is within a specified flight time (initially 90 minutes, one engine inoperative). The Airbus A330-200, powered by the General Electric CF6-80E1 engine, notably achieved pre-service ETOPS certification, establishing a 180-minute diversion time limit [103]. This regulatory shift expanded route options for twin-engine aircraft, previously restricted to larger, multi-engine platforms. While ETOPS primarily addresses the viability of twin-engine operations, the incentive for morphing systems centres on maximising fuel efficiency. If VC operation is treated as non-essential, the aircraft must carry the fuel equivalent of non-VC operation. Given the established acceptance of ETOPS principles by regulatory bodies, manufacturers, and airlines, its framework should inform the planning of VC operations. A concise explanation of ETOPS mission planning follows, describing the constraints of applying this principle to Variable Camber Operational Standards (VCOPS).

The fundamental principle of ETOPS acknowledges the potential for engine failure at any stage of a flight. The core requirement specifies that the flight time to an appropriate alternate airport with one engine inoperative (OEI) must remain below a designated threshold at any given point during the mission. Absent ETOPS certification, this threshold is 60 minutes for twin-engine aircraft. In conjunction with the specified OEI flight speed, this time limit defines geographical areas surrounding alternate airports along the planned route. The standard operational route must be situated within these defined areas, as illustrated by the dashed circles in Figure 42.

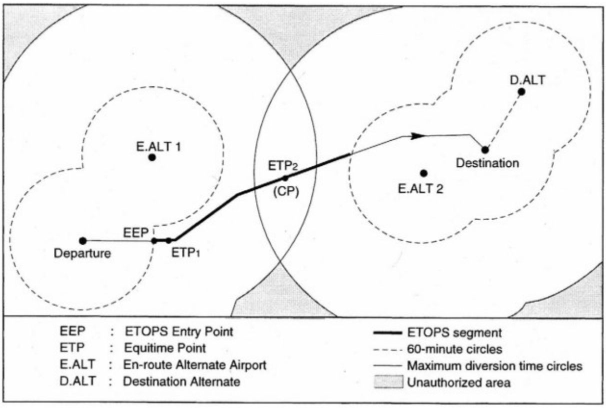

Figure 42: Mission Plan with ETOPS Areas [103].

ETOPS certification and planning allow for the expansion of these operational circles, corresponding to the designated ETOPS category (e.g., 90, 180 minutes), as depicted by the solid circles in Figure 42. Each instance where the route exits a 60-minute circle defines an ETOPS area; this potentially occurs multiple times during a single mission. Within each ETOPS area exists an Equitime Point (ETP), representing the aircraft's position equidistant from two airports. An engine failure at this location necessitates traversing the maximum flight time for that ETOPS area to reach the nearest airport. The ETP associated with the longest flight time to an airport is designated the Critical Point (CP), which determines the required ETOPS rating for the specific mission. Given the increased fuel consumption under OEI conditions, fuel planning must account for ETOPS requirements. Typically, the ETP in the final ETOPS area represents the most critical point for fuel planning due to the minimal remaining fuel. However, this can vary if an earlier ETP involves such a substantial distance to the nearest alternate airport that it becomes the limiting factor for fuel reserves. Each mission necessitates this individual assessment. In contrast to ETOPS, the critical event for VCOPS is a VC system malfunction. This is reflected in the “mission analysis” module by a shift from the merged polar representing full VC system functionality to a polar describing aircraft performance with a VC malfunction. A key distinction between ETOPS and VCOPS lies in the relative importance of post-malfunction flight time. This remaining flight time is paramount in ETOPS, as it dictates the required engine failure probability, the primary driver of ETOPS certification. VCOPS, however, lacks a redundant system; a failure results in increased drag for the remainder of the flight. Consequently, the remaining flight time is less critical in VCOPS, with fuel consumption becoming the central concern. While ETOPS likely remains the defining criterion for twin-engine aircraft long-range route planning, ETOPS circles are irrelevant for VCOPS fuel planning. For VCOPS, the sole relevant factor is the distance to the nearest airport, contingent on whether the reduced aerodynamic performance with a failed VC system prevents reaching the destination airport. The CP is readily determined for a route considering only departure and destination airports, typically at the route midpoint, neglecting weather and terrain. With alternate airports, the CP, as in ETOPS, is one of the ETPs. Having established the relevant ETOPS principles and their implications for VCOPS, they will now be applied to a specific mission using the MICADO "mission analysis" module.

The NAT region, an early adopter of ETOPS principles, serves as a relevant case study. Utilising an Airbus-published example mission for this region [103], this analysis considers a flight originating at John F. Kennedy International Airport (JFK) in New York City, USA, and terminating at Shannon Airport (SNN) in Ireland. As depicted in Figure 43, a direct route is infeasible under the 90-minute ETOPS category.

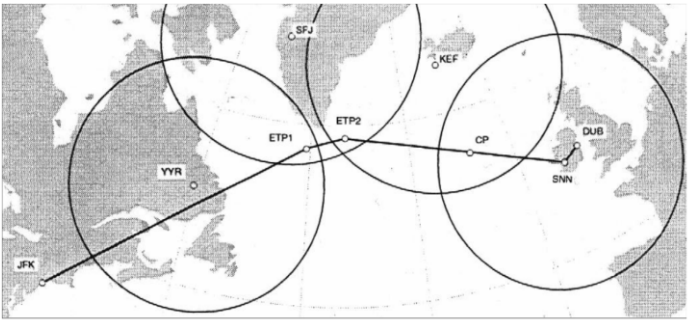

Figure 43: Route JFK - SNN with 90 min ETOPS [103].

As previously discussed, the ETOPS circles depicted are irrelevant to VCOPS. Without ETOPS route restrictions, a viable initial approach involves selecting the direct great circle route and subsequently analysing the impact of a VC system failure. This methodology is adopted for the VCOPS analysis presented herein. Aerodynamic assessment of the VC performance in this thesis suggests that deviation from the direct route is unnecessary (see section 4.3.2). However, with a significantly higher VC performance increase, this would change. Consequently, the 120-minute ETOPS recommended route is selected, enabling the use of the direct route while designating Keflavik, Iceland (KEF), as the alternate airport, yielding a range of 2670 nmi, as illustrated in Figure 44. This route features two ETP. The dashed lines in Figure 44 represent the distance to KEF at any point along the mission. The first ETP denotes equal distance from JFK and KEF, while the second ETP (the CP in Figure 44) is equidistant from KEF and SNN. The second ETP is identified as the CP by comparing the mission abort distances at each ETP. For the first ETP, this distance is the sum of JFK to the first ETP and then to KEF, or alternatively, back to JFK. For the second ETP, the distance is the sum of JFK to the second ETP and then to KEF or, alternatively, to SNN. The longer route to the second ETP designates it as the CP. The resulting diversion range to KEF at the CP is 2010 nmi. Contextually, the 2018 average mission length for the A350-900 fleet, extracted from the Official Aviation Guide of the Airways (OAG) database, is 2600 nmi. Given its greater relevance to the reference aircraft model, the failure analysis will be conducted for a range of 2600 nmi.

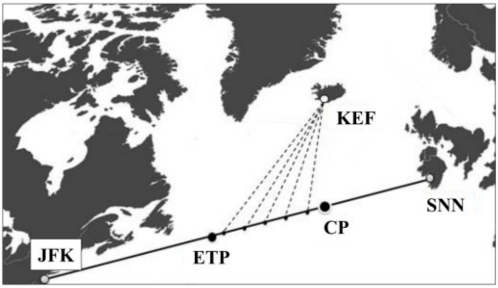

Figure 44: Mission Route JFK- (KEF) – SNN.

Within the context of VCOPS, an analysis of a VC system failure at the CP is required. The parameter study initiated in section 4.4.3 will be expanded to encompass three points to provide a more comprehensive understanding of the effects of such a failure. The required fuel reserves for mission completion can be determined by leveraging MICADO's iterative mission analysis capability for each VC system failure point.

3.3 Lift Distribution Optimiser

For VC studies, it is highly important to analyse the twist of the wing before applying deployed airfoils. Foremost, this is paramount to ensure a fair assessment of the VC technology since a suboptimal twist would have a stronger negative effect on the baseline aircraft compared to the VC aircraft. Furthermore, previous studies by the author have shown that if no twist optimisation is conducted, the possible deployment range of the flaps will at least partly be used for a quasi-twist distribution optimisation. To avoid this and offer the maximum deployment range for actual variations during cruise, executing a twist optimisation for the reference wing is crucial. The necessary basic process is straightforward and was devised by the author of this thesis, Tim Effing made further improvements and the final implementation at ILR. The respective module is named Lift Distribution Modifier (LDM).

The general goal is to adjust the twist of specific sections to meet a given target lift distribution. For this thesis, the optimisation goal will be the induced drag, and hence, the target lift distribution will be elliptic. Therefore, the target lift distribution, given in a normalised form, is scaled to meet the total lift produced by the reference wing. Following Equation (1), the free stream density and wing surface are needed for a given C_L. A given target lift distribution is dissected into n elements in spanwise direction, (see Figure 45 left side). The C_l of each element can be multiplied by the local chord and the element's width (Δη) to calculate the lift of this element. A scaling factor “a” can then be multiplied by either each element or the sum to achieve the desired target lift ($C_{L,target}$), see Figure 45 right side. This is described in Equation (10).

$$C_{L,target} = a * \sum_{0}^{n} (C_l * c)_i * \Delta\eta \tag{10}$$

The result is either the scaling factor or the scaled lift distribution.

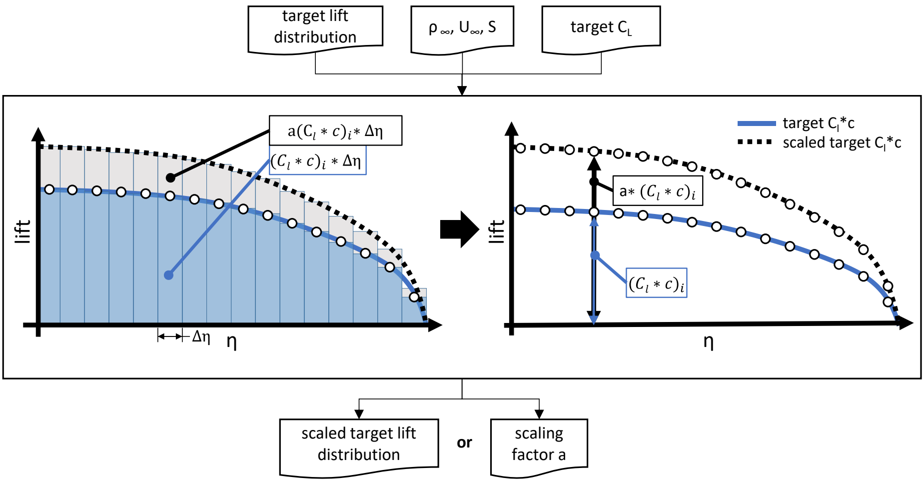

Figure 45: Scaling of normalised target lift distribution.

The second step is the adjustment of the reference wing sections to tune the reference wing's lift distribution to the scaled target lift distribution. For each wing section, the difference between the targeted lift and the lift of the current wing geometry can be calculated according to Equation (11), where α stands for the angle of attack.

$$\Delta\alpha_i = \Delta(C_l * c)_i \frac{d\alpha}{d(C_l * c)} \tag{11}$$

Figure 46 visualises the approach to applying this concept. LILI processes the current wing geometry and provides a respective lift distribution. Equation (11) is used for each section, and the necessary change in α is calculated. The wing geometry is adjusted at each section with the respective α, creating a new wing geometry. These steps are repeated in an iterative loop until a predefined convergence limit is reached. For the gradient of lift and angle of attack change, a default value of 2π is feasible. The specific gradient of each section, determined from previous iterations, could be used if required. This proved to be unnecessary for the optimisation in this thesis.

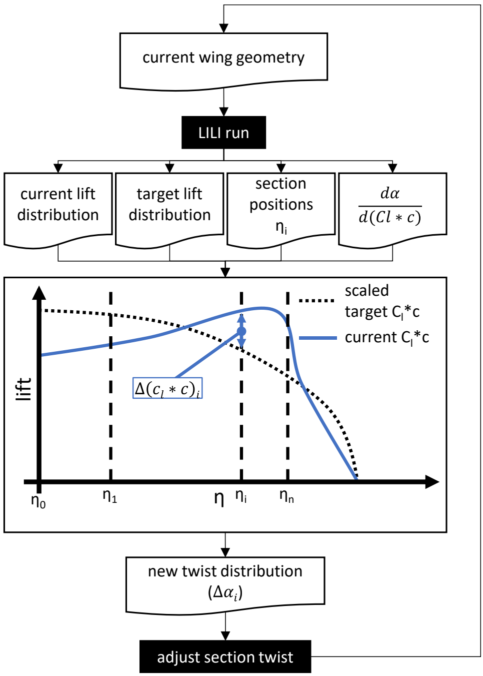

Figure 46: Twist adjustment to achieve scaled target lift distribution.

An alternative optimisation goal would be aircraft L/D, which would include not only the effect of induced drag but also other drag components, mainly the trimmed aircraft drag. Since the moment of each section changes with a twist change, a correction of the trim is necessary, resulting in a shift in trim drag. However, this would require a different approach and would not allow a direct calibration of the lift distribution; hence, it was not implemented for this thesis. More sophisticated modifications of the 3D outer shape of the entire wing have been described in the literature. An example is the wing shape optimisation towards an elliptic lift distribution published by Rodriguez et al. [104]. For conceptual design, these bring the typical challenges of mesh preparation and computational effort.

4 Application of Developed Method

This section describes the VC assessment methodology and the application case of this thesis.

4.1 Reference Aircraft

The definition of a suitable reference aircraft is mandatory to produce a sensible assessment of aviation technology. The data for large commercial aircraft in the public domain is insufficient to execute a conceptual design synthesis of a given aircraft since the manufacturer provides very limited official data. Therefore, the incomplete data must be combined with suitable available data and assumptions. This thesis focuses on creating a method for VC assessment; hence, emphasis is put on the wing design process. The process to create the wing of the reference aircraft will follow the steps listed below and is visualised in Figure 47:

1. select suited aircraft to base reference aircraft on,
2. retrieve wing plan-form,
3. apply given or assumed relative thickness distribution,
4. determine local C_l by applying elliptic lift distribution,
5. transform flow conditions to 2D and
6. select the best-suited airfoil for 2D flow conditions.

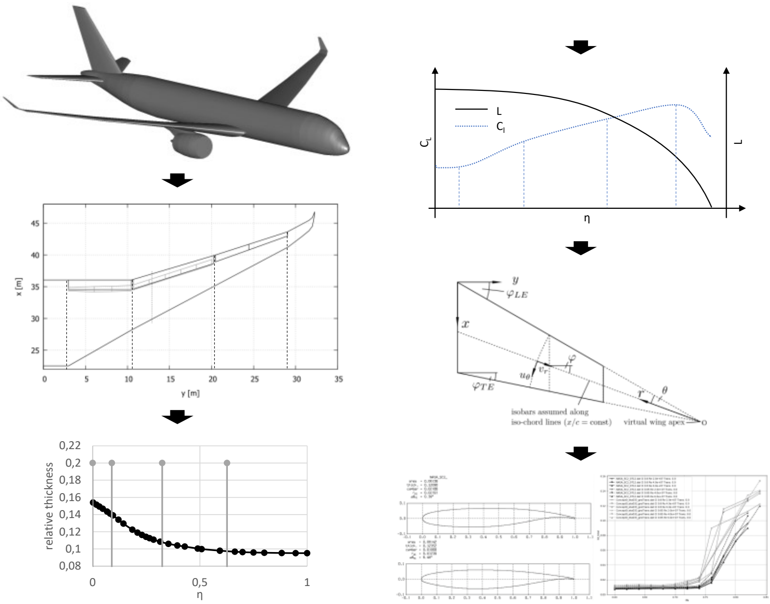

Figure 47: Approach for reference wing geometry derivation

This approach can be applied to other wing-focused technologies to derive a respective reference aircraft wing from existing aircraft. This process was devised by the author and presented at the DLRK 2019 in a presentation with Schültke et al. [105].

4.1.1 Derivation of Application Platform

Applying the presented method on a well-suited and feasible platform increases the meaningfulness of the results. Furthermore, it allows for focusing on the aerodynamic assessment while assuming that other factors (e.g. the weight of the ADHF kinematics) can be neglected for this thesis since they are already inherent to the application platform. Basing the reference aircraft on a real aircraft follows this purpose. As stated by several sources in section 2, the biggest potential for VC is expected for long-range aircraft. Furthermore, the trailing edge flight control surfaces must be able to be deployed during cruise without creating a gap [9] and ideally, it should already be proven to enable a VC operation. Only two large commercial airliners meet these criteria: the Airbus A350 [1] and the Boeing B787 [106–108]. The data availability for the Airbus A350 is better, and a closer exchange of the ILR with Airbus exists than with Boeing. Therefore, the Airbus A350 was selected as the basis for creating the reference aircraft. The Airbus A350 is a long-range commercial passenger aircraft launched at the 2006 Farnborough Airshow [109] and had its first flight on the 14th of June 2013. Due to the high cost of manufacturing and maintenance of high-lift systems, a trend for reducing the complexity of high-lift systems has been observed since the early 80s [9]. During the development of the Airbus A400M, several high-lift systems were extensively analysed, and several research programs supported the maturation of respective technology. Amongst them was the application of the dropped hinge flap concept, which was selected due to its low complexity and suitable performance for the Airbus A400M [110]. Therefore, a crucial technology necessary for the VC functionality, albeit changed for the ADHF, was mature enough to integrate into the Airbus A350 development. The key challenge for applying an ADHF is to achieve sufficiently high-lift coefficients while minimising the distance of the flap hinge point to the wing's lower surface to minimise system weight, fairing complexity, and drag [13]. The Airbus A350 employs an ADHF, enabling the in-flight deployment of its flap by several degrees while closing the gap with a respective spoiler deployment [1]. Sutcliff et al. describe the numerical and experimental tools used in the HICON research project, which played a major part in developing the ADHF [111]. The Airbus A350 variant used in this thesis is the -900 variant. The available data of the A350-900 were compiled and used to create a MIDADO aircraft design, fitting these data as closely as possible. Therefore, the MICADO design framework, described in section 3.1, was applied and calibrated to meet the Operational Empty Mass (OEM) and MTOM. The resulting aircraft will be referred to as ”reference aircraft” in this thesis and is shown in Figure 48.

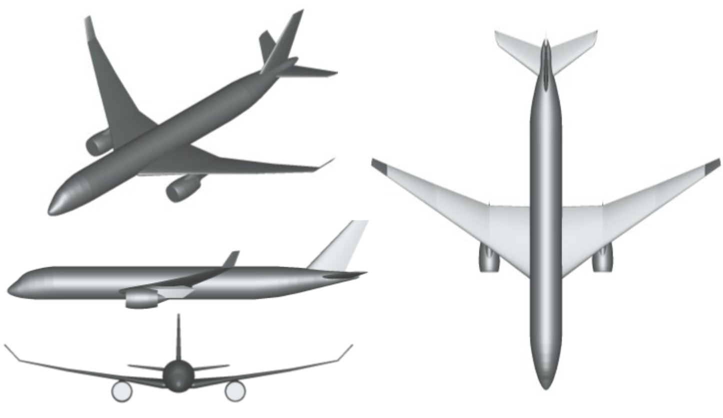

Figure 48: Reference aircraft configuration.

The key overall aircraft data are presented in Table 3. The values for the design mission (i.e. range and seating) were chosen based on the data provided by Strüber [13] for the Airbus A350-900 with 325 passengers on a design mission with a range of 8000 nmi.

Table 3: Reference aircraft key overall aircraft data.

Parameter	Unit	Value
W/S	kg/m²	606
T/W	-	0.285
MTOM	t	268
MLM	t	202
OME	t	135
S	m²	442
Span	m	64.75
Sea level specific thrust	kN	374
PAX	-	325
Payload	Kg	30,875
Design cruise speed	Ma	0.85
Design mission range	nmi	8,000
Design mission payload	t	31
Design mission trip fuel	t	94

4.1.2 Derivation of Wing Geometry

The plan-form of the wing was compiled from data available from Airbus in the ´Aircraft Characteristics Airport and Maintenance Planning" document [112] as well as the available digital 2D drawings on the Airbus homepage [113]. A top view of the wing is shown in Figure 49, with the control surface layout taken from Strüber [13].

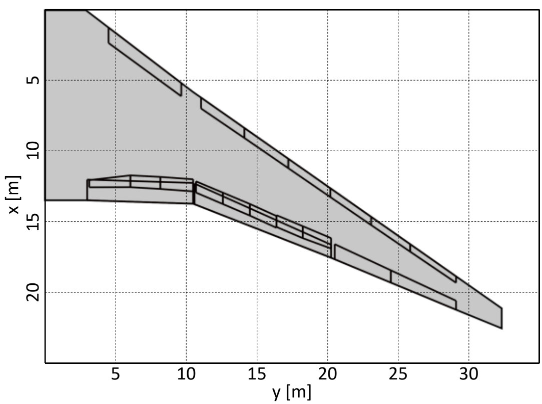

Figure 49: Top view of the reference aircraft wing.

In conceptual design, creating the wing out of segments between sections where the airfoils are defined is common. These segments are often chosen for areas with constant leading and trailing edge sweep angles. This is also the geometry structure in MICADO, which leads to 5 segments for the reference aircraft wing, including the winglet.

With the definition of the plan-form of the wing, the 3D flow conditions for the principal sections (outer kink, inner kink, and root) can be estimated. The 3D flow conditions are assumed for an approximated mid-cruise point, with an expected c_L of 0.5, a Ma of 0.85, International Standard Atmosphere (ISA) conditions, and an altitude of 390,000 ft. The 3D local lift coefficients are deducted by applying an elliptical lift distribution, as shown in Figure 50, dividing the local lift at each span position by the local chord length.

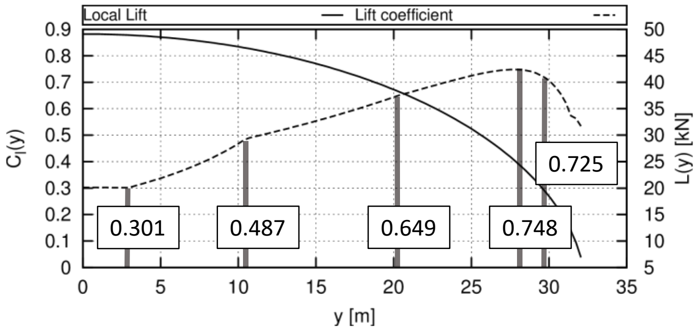

Figure 50: Local lift coefficients for the reference wing with an elliptical lift distribution [105].

The plan-form data and 3D flow conditions for the three main sections (between wing root and winglet) and the 2D conditions resulting from the application of the SST (see section 3.1.2.3) are given in Table 4.

Table 4: Plan-form data, 3D and initial 2D flow conditions for main reference wing sections.

parameter	unit	outer kink	inner kink	root
η	-	0.63	0.32	0.09
chord	m	4.89	7.91	13.5
ϕ_{LE}	°	35.0	35.0	37.3
ϕ_{25}	°	32.2	31.9	30.1
ϕ_{TE}	°	22.8	21.4	1.7
Re (rounded)	-	$3*10^7$	$4*10^7$	$8*10^7$
C_{l3D}	-	0.649	0.487	0.301
C_{l2D}	-	0.907	0.574	0.348
Ma_{3D}	-	0.85	0.85	0.85
Ma_{2D}	-	0.720	0.722	0.735

The derived 2D flow conditions will be used as initial values in section 4.1.3 for a shock position iteration, resulting in more accurate values for the subsequent airfoil assessment.

As stated in section 3.1.2.2 , intermediate segments are necessary due to the setup of the “calculate polar” module and to maximise similarity to the VCCTEF concept. The intermediate segments are added to the left and right of a flap as a connection and serve as the transition of the flap to the other wing segments, i.e. they change in form when the deployment angle of the flap changes. These segments are not added to the span, but additional sectional cuts are added, and the respective chords and thicknesses are interpolated to ensure that the 3D wing geometry is not changed. Three inserted segments are required at the position of the fuselage/inner flap, the inner/outer flap, and the outer flap/aileron section. During the introduction of these segments, it was found that they introduce discontinuities in the lift distribution calculated by LILI, which are strongly sensitive to the size of the inserted segments. Therefore, the size of the inserted segments should be selected with care, and the following compromise must be solved:

- larger segments deviate more from the original plan-form of the control surfaces and enlarge the area that cannot be fully deployed for the VC system
- smaller segments lead to higher spikes in lift distribution and produce errors that must be solved due to overlapping spoiler surfaces during wing scaling operations during the MICADO design loop

A study was performed with inserted segments of 0.5 %, 1.0 %, 1.5 %, 2.5 %, 5.0 % and 7.5 % of the original segment's span. As a compromise, the segments with 5 % of the segment size were selected since they did not produce extreme spikes in the lift distribution. The resulting inserted segments span 0.34 m, 0.48 m, and 0.46 m. As a comparison, the wing for the VCCTEF system presented by Urnes [66] includes 0.203 m flexible segments for the GTM, which has a total wing span of approximately 38 m, which is 1.7 times smaller than the reference aircraft wing span. Therefore, the size of the inserted segments was judged to be reasonable. Figure 51 shows the segmentation of the reference aircraft wing with the added segments.

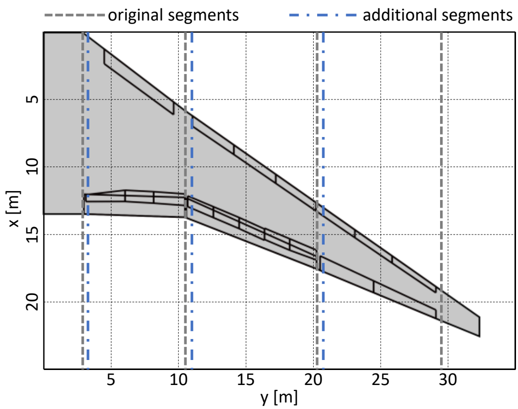

Figure 51: Reference aircraft wing segmentation.

Progressing from the plan-form to the thickness and twist distribution, similar data or estimates must be adapted since these data are often unavailable for existing aircraft in the public domain. The thickness distribution for the reference aircraft is taken from the NASA Common Research Model (CRM). The CRM is a generic aircraft configuration created for research purposes and published in 2008 by Vassberg et al. [114]. The general layout of the CRM is similar to the Boeing B777 [115], with a wing incorporating a contemporary transonic supercritical design. The design cruise Ma of the CRM is described to be 0.85 with a quarter chord line sweep of 35° [114]. The complete geometry of the CRM is publicly available at https://commonresearchmodel.larc.nasa.gov/. Due to the similar design conditions, the thickness and initial twist distribution were used for the reference aircraft. The data extracted from the geometry are shown in Figure 52 in combination with the position of the root, inner, and outer kink positions of the reference aircraft, which are indicated by vertical dashed lines. Several other data for thickness and twist distribution for existing aircraft are given by Obert [116].

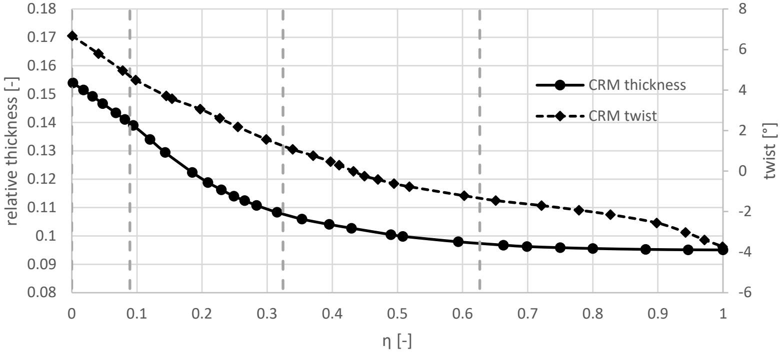

Figure 52: Relative thickness and twist distribution of the CRM.

The selected thickness distribution will not be changed since it reflects the aeroelastic compromise stated by the decreasing wing weight for increasing applied airfoil thicknesses and the higher drag associated with thicker airfoils. Since the structural assessment is outside this thesis's scope, and a specific optimisation is not conducted, the thickness ratio is adapted and kept constant. In contrast, the twist distribution has a strong interdependency with VC and will be changed according to the process described in section 4.1.4.

4.1.3 Airfoil Selection

In this thesis, the pressure distribution of airfoils is discussed in terms of the pressure coefficient (c_p). c_p in an airfoil pressure distribution quantifies local pressure variations and is defined by Equation (12) as defined by Anderson [117], where p is local pressure and p_∞ is freestream pressure. $c_p < 0$ indicates low pressure (suction) atop the airfoil, promoting lift. $C_p > 0$ signifies higher pressure below, contributing to downforce. Understanding c_p aids in optimising airfoil design for efficient aerodynamic performance.

$$c_p = \frac{p - p_\infty}{\frac{1}{2} * \rho * U^2} \tag{12}$$

Two sets of airfoils were assessed for application in the reference aircraft—those extracted from the CRM and the NASA supercritical airfoil family (NASA SC airfoils). The CRM was previously discussed. The airfoils are taken from the representative span positions, the kink (η = 0.33, with η being the relative span position), and an airfoil taken from a segment change at a relative span position of η = 0.77. The root airfoil was not taken from the CRM since the 2D analysis of a 3D root airfoil, as the one from the CRM, does not yield sensible results. Several features are included in the design of a 3D root airfoil (e.g. mitigation of the fuselage interference) that cannot be adequately represented in a 2D analysis. For the root airfoil, only the NASA SC airfoils will be considered. Furthermore, the relatively poor aerodynamic performance of the root airfoil is tolerated even in reality and is to be expected since root airfoil design compromises have to be accommodated [6]. The tip section will use the outer kink airfoil since the thickness-to-chord ratio change is sufficiently small. Since the CRM airfoils are extracted from the 3D wing geometry, they must be processed with the airfoil transformation to produce representative 2D geometries, which is accomplished by applying the inversion of Equation (7) and the data given for the outer and inner kink in Table 4. The selected 3D and 2D CRM airfoils are shown in Figure 53.

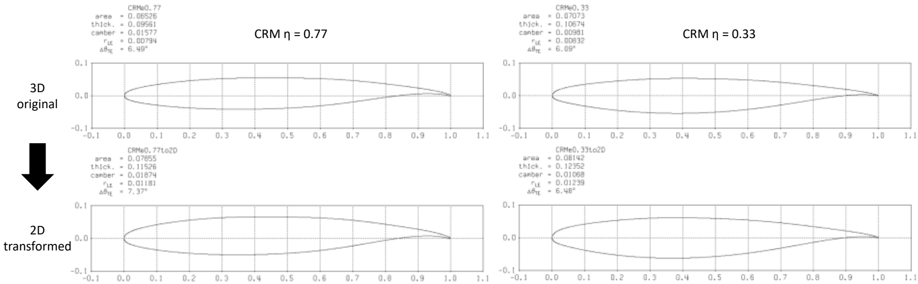

Figure 53: Extracted CRM airfoils and the transformed 2D geometry.

The following will discuss the NASA SC airfoils in more detail before the performance assessment of the CRM and NASA SC airfoils is conducted. During the 1960s and 1970s, NASA attempted to create a 2D airfoil family for the transonic regime with a high drag divergence Ma and good low-speed lift and stall characteristics. The airfoils of the first phase experienced drag creep. Improvement was achieved during phase 2 by employing wind tunnel tests and available transonic and viscous computational methods. The result was a family of airfoils that feature a drag rise Ma well below the critical Ma and a supersonic flow over a major portion of the upper surface, which were subsequently published by Harris in 1990 [118]. Harris provides tables with the coordinates that were used in this thesis. The notation of the family is a four-digit number, in which the first two digits are the design c_l of the airfoil, and the third and fourth digits stand for the relative thickness ratio. When directly analysed with either XFOIL or MSES, all NASA SC airfoils produced a very uneven “wavy” pressure distribution. XFOIL primarily employs computational methods based on potential flow theory to analyse and predict the aerodynamic characteristics of airfoils. Potential flow theory assumes that air behaves as an incompressible, inviscid fluid. The main computational method used by XFOIL is the panel method. In this approach, the airfoil surface is divided into panels, and the circulation (vorticity) distribution along these panels is determined to satisfy the no-flow-through boundary condition. This circulation distribution is then used to calculate the pressure distribution around the airfoil, providing information about lift, drag, and other aerodynamic characteristics. While this is insufficient for the aerodynamic performance assessment of the airfoil and the transonic application case of this thesis, XFOIL is valuable in assessing the smoothness of, e.g., the velocity distribution of an airfoil. The XFOIL tool provides a function named ´FILT´, which employs a Hanning window filter on the Fourier coefficients of the velocity distribution of the airfoil and modifies the airfoil geometry [56]. The Fourier coefficients are applied to express the velocity distribution of the flow over the airfoil as a periodic function, as a sum of sinusoidal functions (sines and cosines). Subsequently, the Hanning window filter applies a bell-shaped window function designed to taper the edges, reducing the velocity distribution changes. Multiple consecutive FILT applications on each airfoil were necessary for a satisfactory result. Each application leads to a further deviation of the airfoil geometry from the original data set. Therefore, a study was conducted to analyse the effects of FILT on the global airfoil parameters. An excerpt of the study for the NASA SC 0710 airfoil is displayed in Figure 54, showing the c_p over the relative x-coordinate of the airfoil for Ma 0.8 and c_l of 0.7.

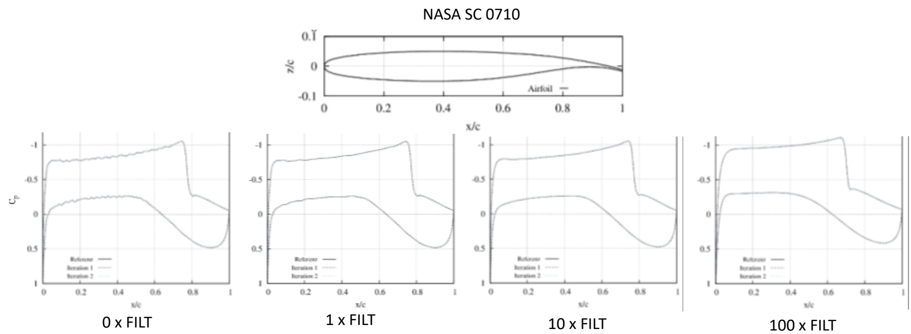

Figure 54: Effect of the XFOIL FILT command on the pressure distribution of the NASA SC 0712 airfoil.

The effect on the global airfoil parameters, a consecutive execution of the FILT command from zero to one hundred times, is listed in Table 5.

Table 5: Effect on the XFOIL FILT command on the NASA SC 0710 airfoil global parameters.

FILT	Chord	Thickness/Chord	L/D
0	13.3048	0.0998	31.62
1	13.3048	0.0996	31.64
10	13.3048	0.1006	30.96
100	13.3048	0.1108	19.91

The best compromise between alteration from the original airfoil geometry and smoothness of the pressure distribution was judged to be the ten-time application of FILT. This treatment was applied to all NASA SC airfoils analysed in this thesis. It must be pointed out that XFOIL was only used to check the smoothness of the pressure distribution and to use its geometry modification functions. All aerodynamic results in this thesis, including the pressure distribution in Figure 54, have been calculated with MSES.

The occurring thickness ratio and c_l must be considered to select the best-suited NASA SC airfoil family member for the flow condition at a given section of the reference aircraft wing. Table 6 lists the leading and trailing edge angles and the thickness to chord ratio for the reference wing's root, inner, and outer kink. The NASA SC airfoil family provides airfoils with 10 %, 12 % and 14 % thickness to chord ratios for several lift coefficients. The column “2D thickness to chord ratio” contains the thickness to chord ratios calculated by XFOIL and deviates from the ratio stated by the airfoil designation. As discussed in section 3.1.2.3, the transformation from 2D to 3D is done with Equation (7) for the airfoil geometry and hence relates the thickness to chord ratio of the 2D airfoil to the one of the 3D airfoil. The airfoils selected for the reference wing are marked in bold font and have been chosen based on the lowest delta from the target thickness to chord ratio given in the last column. The lift coefficients were selected due to estimates from previous studies' experience and were chosen conservatively to provide a sufficient margin for twist optimisation.

Table 6: NASA SC airfoil thicknesses before and after transformation from 2D to 3D.

span position	leading edge sweep angle [°]	trailing edge sweep angle [°]	target thickness to chord ratio	NASA SC airfoil	2D thickness to chord ratio	transformed 3D thickness to chord ratio	Δ [%]
o. kink	35.0	22.8	0.0968	0710	0.1008	0.0867	10.43
o. kink	**35.0**	**22.8**	**0.0968**	**0712**	**0.1209**	**0.1040**	**-7.41**
o. kink	35.0	22.8	0.0968	0714	0.1405	0.1208	-24.76
i. kink	35.0	21.4	0.1083	0710	0.1008	0.0871	19.58
i. kink	**35.0**	**21.4**	**0.1083**	**0712**	**0.1209**	**0.1045**	**3.51**
i. kink	35.0	21.4	0.1083	0714	0.1405	0.1214	-12.06
root	37.3	1.70	0.1380	0610	0.1008	0.0912	33.90
root	37.3	1.70	0.1380	0612	0.1210	0.1094	20.72
root	**37.3**	**1.70**	**0.1380**	**0614**	**0.1407**	**0.1270**	**7.99**
root	37.3	1.70	0.1380	0410	0.1007	0.0912	33.94
root	37.3	1.70	0.1380	0412	0.1210	0.1094	20.75
root	**37.3**	**1.70**	**0.1380**	**0414**	**0.1410**	**0.1274**	**7.72**

The respective NASA SC airfoils are shown in Figure 55 and Figure 56 with the original geometry, which will be used for the 2D analysis, and the 3D geometries derived according to the taper sweep theory.

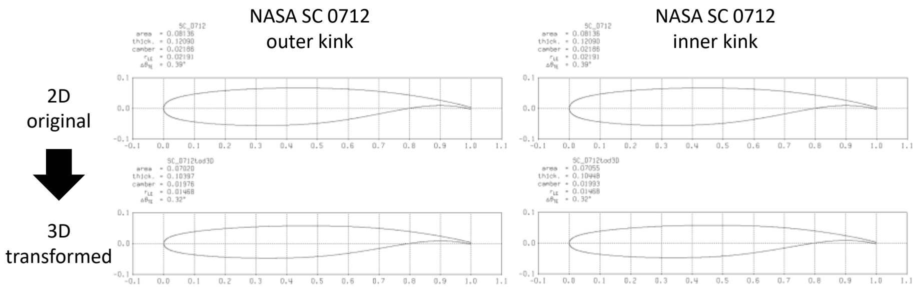

Figure 55: Airfoils from the NASA super critical family for the inner and outer kink comparison.

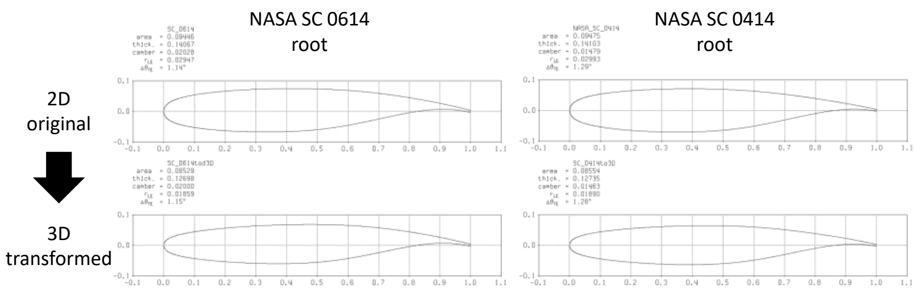

Figure 56: Airfoils from the NASA super critical family for the root comparison.

In addition to selecting the closest airfoil from the NASA SC airfoils, scaling could be conducted with, e.g. XFOIL. Harris gives as a rule of thumb that with each 0.01 reduction of airfoil thickness, a 0.01 increase in drag rise Ma can be achieved [118]. Since the airfoil design is considered outside this thesis's scope, it was decided not to change the original 2D airfoils. However, if an airfoil optimisation is conducted, scaling could be incorporated into the presented methodology with little effort, replacing the selection above.

One aspect that should be mentioned is the difference between the CRM airfoils and the NASA SC airfoils in terms of their thickness to chord ratio, i.e. 0.115 vs 0.121 for the inner kink and 0.124 vs 0.121 for the outer kink. A possibility to alleviate this difference would be a thickness scaling of the airfoils. Since this would change the original design of the airfoils and hence introduce uncertainty if this impacts the specific airfoil performance positively or negatively, it was chosen not to do this in this thesis.

After sets of the CRM airfoils and NASA SC airfoils have been selected, the flow conditions (i.e. Ma and C_l listed in Table 4) must be transformed from 3D to 2D with the SST. The transformation of the 3D flow conditions to 2D was discussed in section 3.1.2.3 and is best done with the local sweep angle at the shock position as a reference sweep angle. This, however, requires an iterative approach since the shock position changes with the assumed flow conditions. For this reason, an iteration strategy was devised and implemented using the MSES results, including the shock position for each point of the airfoil polar representing different 2D flow conditions. The process is shown in Figure 57. The 3D flow conditions are initially transformed with the sweep angle of the default shock position at 25 % chord. The results showed that a default position of 50 % would be advantageous. The resulting 2D flow conditions yield a new shock position and local sweep angle. The transformation is repeated with the new sweep angle. This process was repeated seven times, after which sufficient convergence was observed for all airfoils used in this thesis.

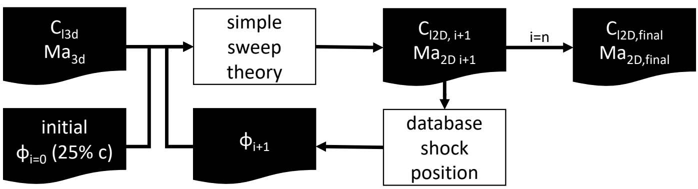

Figure 57: Shock position iteration for the 3D to 2D flow condition transformation.

Since the result of the shock position iteration determines the transformation of the flow condition, it will be decided per wing section if only the iteration result of one airfoil set is used for the transformation, or both will be analysed. The latter one will be applied if the convergence results differ strongly.

This process will be applied homogeneously to the three principal wing sections: outer kink, inner kink, and the root.

4.1.3.1 *Outer Kink*

Starting with the analysis of the outer kink, the results from this process are shown in Figure 58 for the NASA SC 0712 (see Figure 55), and the 2D-transformed CRM airfoil used for the outer kink (see Figure 53).

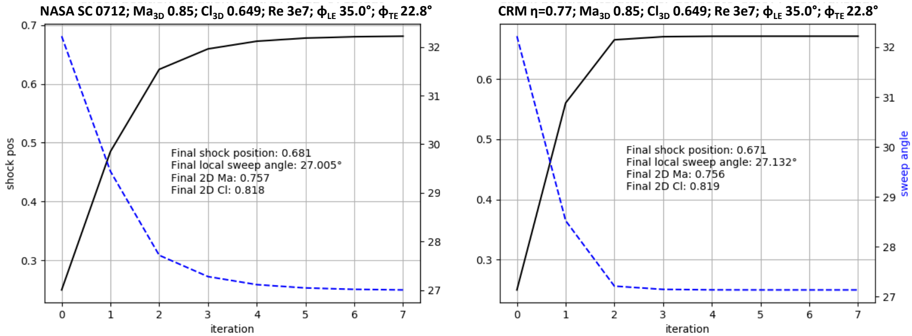

Figure 58: Shock position iteration and respective 2D flow conditions for the outer kink.

The left side of Figure 58 shows the iteration and the convergence for the NASA SC 0712 airfoil. Good convergence is reached, and the final shock position is at a relative chord of 0.681 with a respective local sweep angle of 27.0°. The resulting 2D flow conditions are a Ma_{2D} of 0.757 and a C_{l2d} of 0.818 for the NASA SC airfoil. Since the CRM airfoil's final 2D flow condition values are similar (see the right side of Figure 58), the values mentioned above will be used for the outer kink transformation.

The total drag versus Ma is shown in Figure 59. The CRM airfoil's name contains the eta position of the extraction from the CRM data set, not the eta position of the reference wing. The respective position of the reference wing is listed in Table 4.

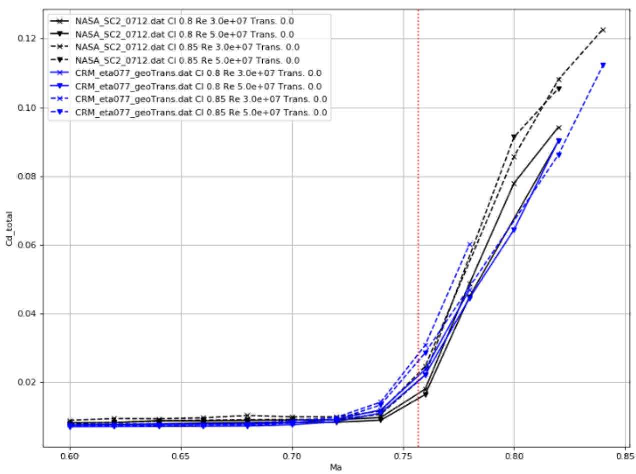

Figure 59: Reference airfoil comparison for total drag vs Ma for the outer kink.

As stated in section 3.1.2.4, all results in this thesis are for a fully turbulent flow, hence the information in the legend that the transition occurs at 0.0 relative chord length. Figure 59 contains the results for the C_l above and below the determined assessment point for the outer kink (0.818) and for a Re of $3*10^7$ and $5*10^7$ to analyse trends due to a change in Re. The vertical dashed line in red indicates the Ma assessment point of 0.757. The drag numbers for the CRM airfoil at the assessment point are higher than the NASA SC 0712 airfoil when similar flow conditions are assessed. Furthermore, it can be seen that the trends due to the shift in Re do not change, and the change in the magnitude of values is rather small. The assessment point is located in the drag rise for both airfoils, which shows that the 3D and the respective 2D flow conditions pose a challenging situation for both airfoil candidates.

The resulting performance in terms of L/D versus C_l is shown in Figure 60. The vertical dashed red line indicates the assessment lift coefficient, while the assessment Ma (0.757) is close to the dashed lines, representing a Ma of 0.76. For these values, the previously observed lower drag values of the NASA SC 0712 airfoil are translated into higher L/D, as could be expected. The L/D for the NASA SC airfoil for a Ma 0.76, Re $3*10^7$ and C_l 0.757 is approximately 41.3, which is rather low for a 2D airfoil L/D, resulting from the flow condition point in the drag rise.

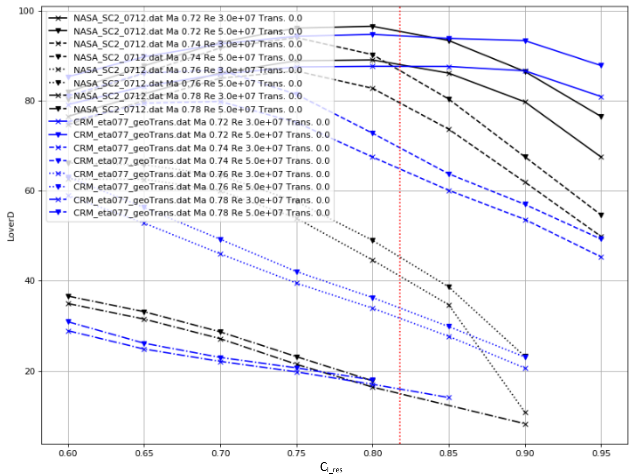

Figure 60: Reference airfoil comparison for L/D vs C_{l_res} for the outer kink.

Figure 61 shows the product of Ma and L/D versus Ma, which indicates the best-suited operational range of the airfoil with regard to Ma. The CRM airfoil is better suited for lower Ma, while the NASA SC 0712 airfoil has a slight advantage in the challenging flow conditions posed by the mid-cruise point and plan-form. Both airfoils are beyond their optimum operational range in terms of Ma, represented by the plateau below a Ma of approximately 0.72.

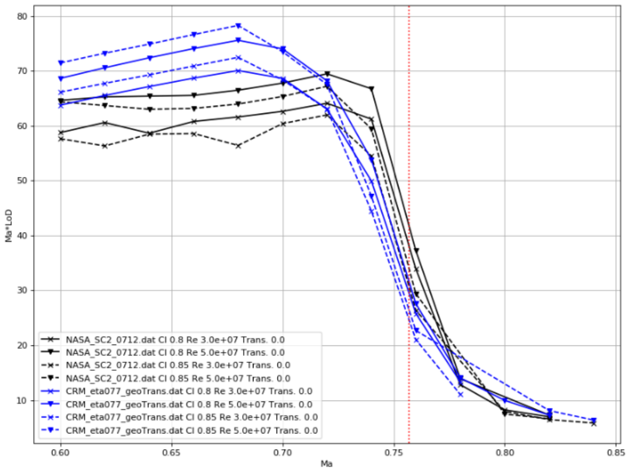

*Figure 61: Reference airfoil comparison for Ma*L/D vs Ma for the outer kink.*

The shock position on the upper airfoil surface at a relative chord position versus Ma is shown in Figure 62. It is used as a marker for the continuity and feasibility of the results. Both airfoils show a continuous shift of the shock position to the end of the airfoil until a Ma of approximately 0.76, after which the shock moves to the front. Again, a small impact of the change in Re can be observed.

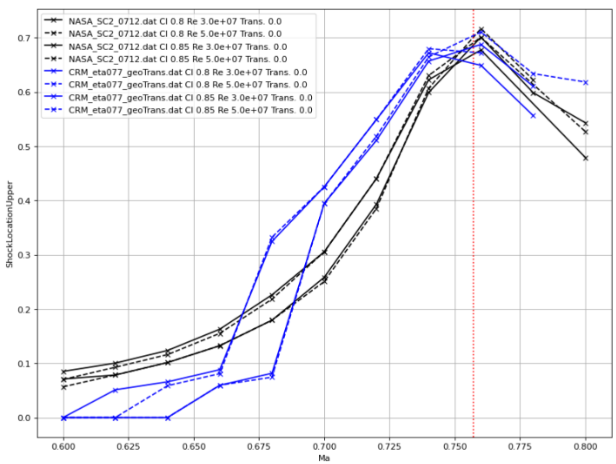

Figure 62: Reference airfoil comparison for shock location vs Ma for the outer kink.

Due to the better performance in terms of L/D, the NASA SC 0712 airfoil is selected for the outer kink section.

4.1.3.2 Inner Kink

The same process was applied to the airfoils under consideration for the inner kink, with the results shown in Figure 63. The NASAS SC airfoil displays a relatively far forward shock position of 0.181, shown on the left of Figure 63. This might result from specific flow conditions, e.g., comparably low C_l in comparison to the design C_l of 0.7 and will be examined in the later analysis. As expected, the resulting 2D flow conditions differ considerably for the NASA SC airfoil and the CRM airfoil. As before, the NASA SC airfoil 2D flow conditions (Ma_{2D} 0.714 and C_{l2D} 0.691) will be used as a primary reference, but the CRM values (Ma_{2D} 0.752 and C_{l2D} 0.622) will also be considered.

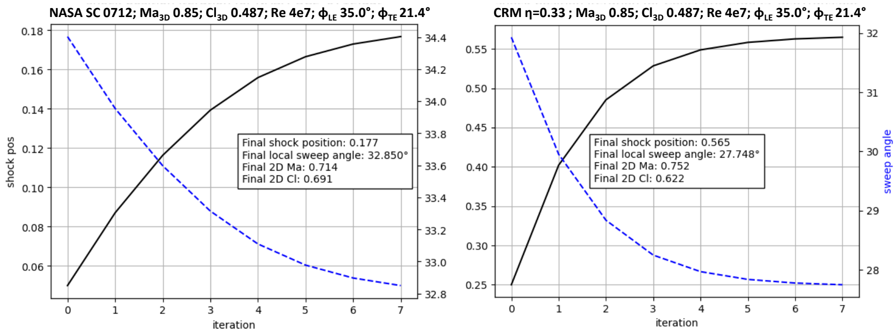

Figure 63: Shock position iteration and respective 2D flow conditions for the inner kink.

Figure 64 shows the total drag versus Ma; again, a slightly earlier drag rise for the CRM is visible. The assessment point deducted from the NASA SC 0712 shock iteration (Ma_{2D} 0.714 and C_{l2D} 0.691) is below the drag rise, while the assessment point from the CRM shock iteration (Ma_{2D} 0.752 and C_{l2D} 0.694) is again located at its start.

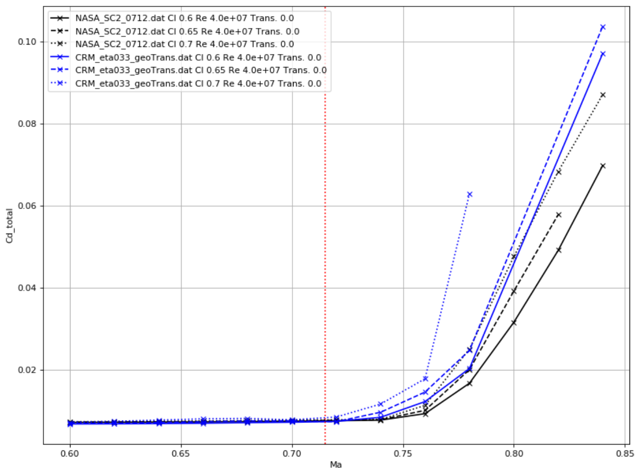

Figure 64: Reference airfoil comparison for total drag vs Ma for the inner kink.

The L/D versus C_{l_res} graph shown in Figure 65 does not yield a benefit for the NASA SC 0712 airfoil for low C_l and Ma. However, at the NASA SC 0712 assessment point, the CRM is at a slight disadvantage, while this disadvantage becomes large for the CRM assessment point due to the increased Ma.

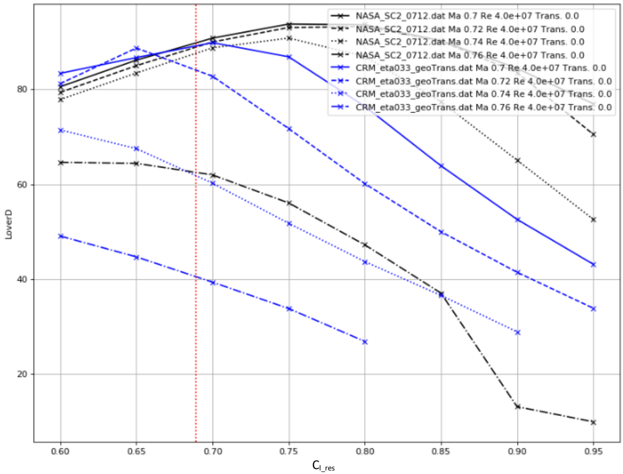

Figure 65: Reference airfoil comparison for L/D vs C_{l_res} for the inner kink.

The trend of the earlier degradation of the CRM in terms of Ma is also visible in the Ma*L/D versus Ma plot shown in Figure 66.

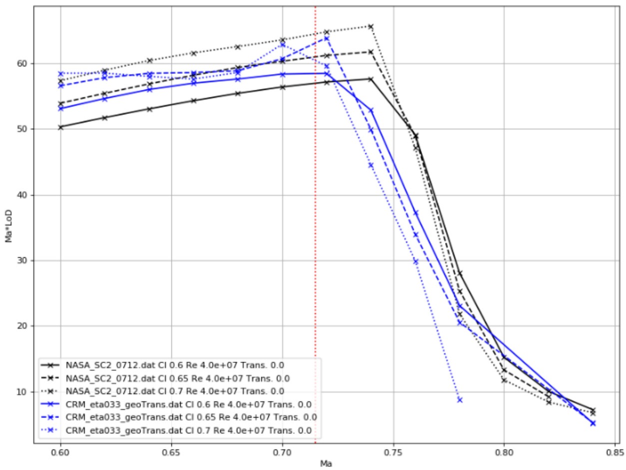

*Figure 66: Reference airfoil comparison for Ma*L/D vs Ma for the inner kink.*

The aforementioned relatively forward shock position of the NASA SC 0712 airfoil is confirmed in Figure 67. Since the chosen Re of $4*10^7$ for the inner kink is in between the previously examined Re for the outer kink ($3*10^7$ and $5*10^7$), the strong change in shock position can be accounted to the reduced C_l for the inner kink resulting from the elliptic lift distribution and plan-form. Hence, the lower loading of the inner kink section leads to a later onset of a supersonic flow plateau for the NASA SC airfoil. This effect is not visible for the CRM airfoil.

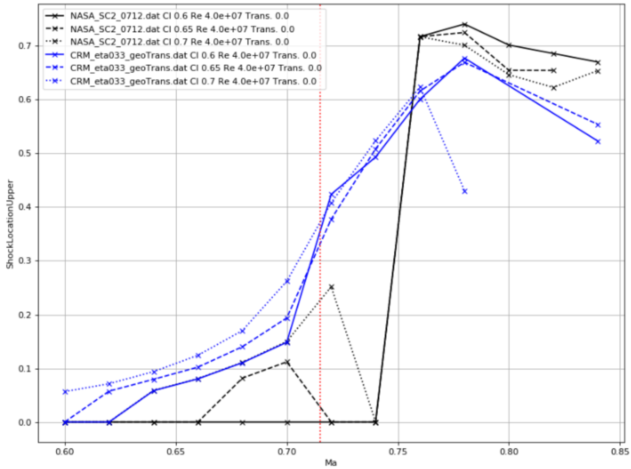

Figure 67: Reference airfoil comparison for shock location vs Ma for the inner kink.

Due to the better performance of the NASA SC 0712 for both assessment points, the NASA SC 0712 is chosen as the airfoil for the inner kink section.

4.1.3.3 Root

For the root section, only the NASA SC 0614 and the NASA SC 0414 will be considered due to the reasons stated at the beginning of section 4.1.3. The respective shock position iterations are shown in Figure 68. The resulting 2D flow conditions are a Ma_{2D} of 0.815 and a C_{l2D} 0.328 for the 0614, a Ma_{2D} of 0.811, and a C_{l2D} 0.330 for the 0414. The final shock position of the 0414 is forward of the 0614's, 0.647 for the 0614 and 0.614 for the 0414. For the root section, the shock position strongly influences the SST-results since ϕ_{TE} is 1.7°, which leads to very small transformational effects when the shock position approaches the trailing edge. Hence, the transformation angle becomes small. The results of the 0614 shock position iteration will be marked in the following plots, but the assessment point of the 0414 will also be discussed.

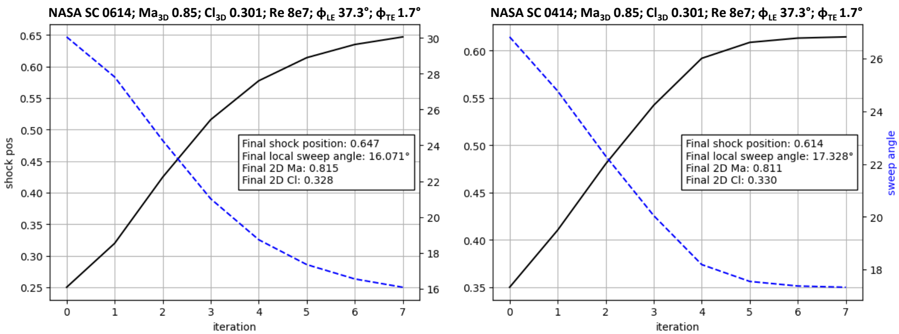

Figure 68: Shock position iteration and respective 2D flow conditions for the root section.

The drag rise of both root airfoils is shown in Figure 69.

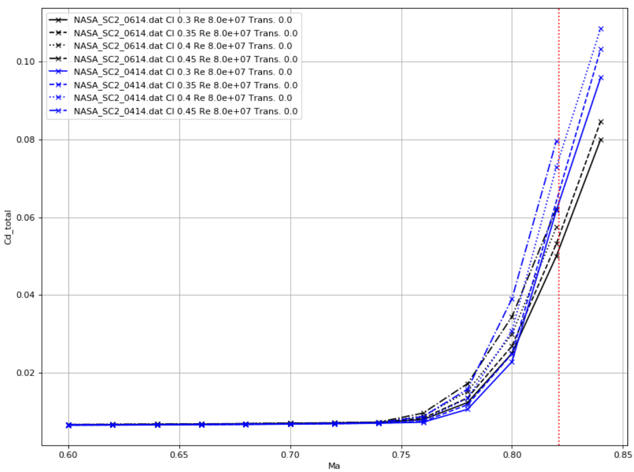

Figure 69: Reference airfoil comparison for total drag vs Ma for the root span position.

For the 0614 assessment point, both airfoils can be expected to have poor performance since the drag rise has fully developed. However, bad performance of the root airfoil is to be expected due to the reasons given at the beginning of this section. The 0414 assessment point lies marginally below that of the 0614 and therefore is also in the drag rise.

The performance in terms of L/D is displayed in Figure 70. The values for the 0614 assessment point are very low, in the order of 5 to 7, as is the case for the 0414 assessment point. It must be remembered that the better L/D performance of a specific assessment point does not mean a better performance of the respective airfoil. The performance of both airfoils on both assessment points is very similar, only showing a minor advantage of each airfoil at its specific assessment point. The 0614 airfoil has a much higher margin regarding higher C_l; thus, it is the conservative choice.

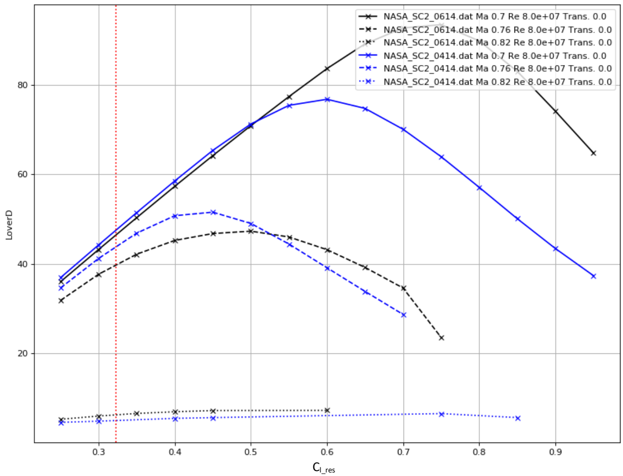

Figure 70: Reference airfoil comparison for L/D vs C_{l_res} for the root span position.

The similarity of the 0614 and 0414 performances is also visible in Figure 71.

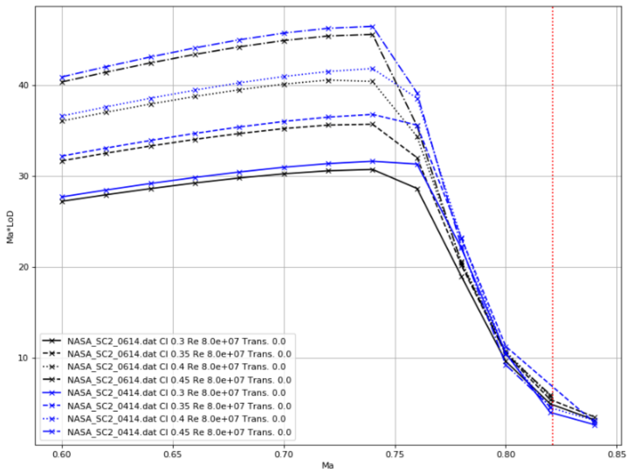

*Figure 71: Reference airfoil comparison for Ma*L/D vs Ma for the root span position.*

Confirmation of the small difference in shock positions between the two airfoils is given in Figure 72.

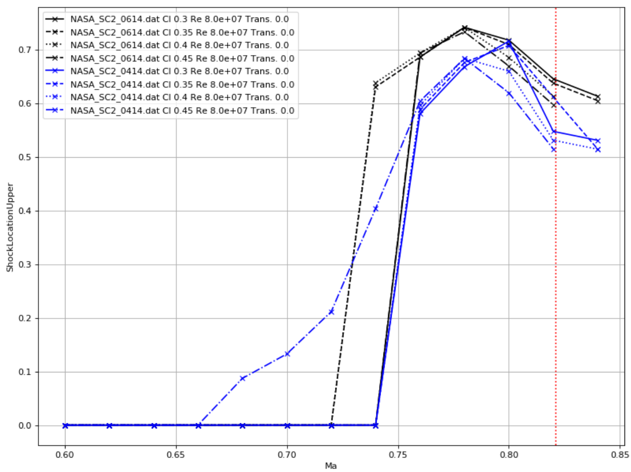

Figure 72: Reference airfoil comparison for shock location vs Ma for the root span position.

Due to the higher margin in terms of better performance for higher C_l, the 0614 airfoil is chosen for the root section of the reference wing.

4.1.4 Twist Distribution Adaptation Without Database Input

After airfoils have been chosen for each section of the reference wing, the twist distribution can be adjusted. In the first step, this will be applied to the aircraft without incorporating the MSES results described in section 3.1.2.3 but only using the handbook methods for friction and wave drag. Subsequently, the twist and lift distribution will be adapted to facilitate applying the MSES results.

The LDM, as described in section 3.3, was applied to the reference aircraft wing with the original segments (unsegmented) and the additional segmentation introduced in section 4.1.2 and displayed in Figure 51 (segmented). As the process description suggested, an elliptic lift distribution was used as the target lift distribution. The loop, shown in Figure 46, was executed for fifty instances. The LDM results are shown in Figure 73. The section-wise lift is shown on the left, and the lift coefficient is on the right. For the original twist, the sectional lift and lift coefficient are similar, except for the peak in the sectional lift caused by the additional segments. While not perfectly elliptical, the lift distributions produced by the LDM are much more an approximation of an elliptical distribution. The twist adjustment could somewhat mitigate the peak but not completely compensate for it. The target was achieved as close as possible for the wing without additional segments with limited control points (wing sections). At this stage, it can already be seen that the local lift coefficients for the elliptic lift distribution are very high on the outer parts of the wing. This is a direct outcome of the plan-form of the reference aircraft wing and the elliptic lift distribution and is practically independent of the presented methodology.

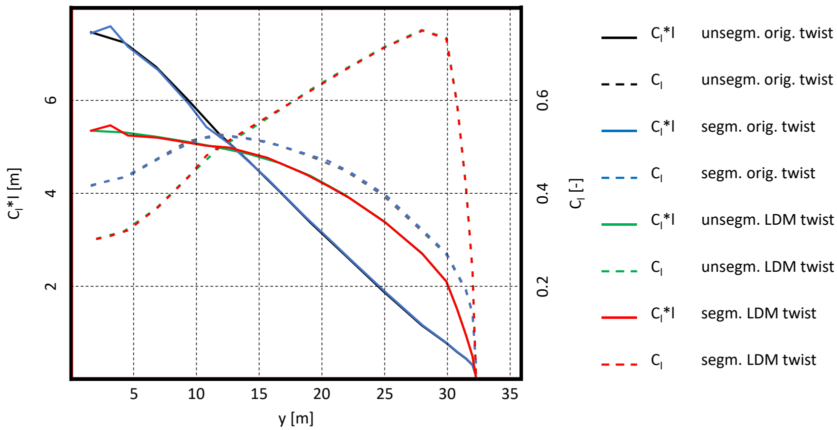

Figure 73: Lift distribution modifier result for the reference wing with and without additional segments.

The high local lift coefficients will impact the database's application since the lift coefficient range produced by MSES for the 2D airfoils is limited. A respective adaptation of the twist and lift coefficient will be performed in section 4.1.5.

Figure 74 shows the twist distribution produced by the LDM for the lift distributions above. While the original twist distributions show the predefined form typical for civil transportation aircraft, the LDM results show a reduced inboard twist and an increased outboard twist.

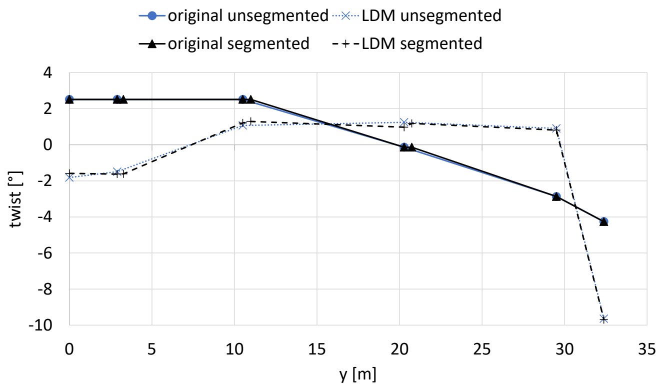

Figure 74: Lift distribution modifier results for the reference wing with and without additional segments.

It is important to state that for all calculations in the aerodynamic chain in this thesis (and MICADO in the current state), the geometric twist angle modified by the LDM is not used anymore once LILI has processed the geometry, including its twist, and has produced the lift distribution. The database access to incorporate the MSES results (see section 3.1.2) only uses lift coefficients extracted from the twist distribution. The geometric twist is not used as input into the database. Hence, a change in geometric twist distribution is acceptable if it achieves a superior lift distribution. It should be kept in mind that the produced geometry would affect any calculations with higher-order 3D methods, e.g. RANS simulations that are based on the geometry. Lane et al. [119] assumed in 2010 that the difference between the original and the LDM twist distribution is because lifting line theory only considers the airfoil's skeleton line and neglects the airfoil's thickness.

In conclusion, a comparison of significant aircraft level parameters of the reference wing with and without the additional segments, as well as the original twist distribution and the LDM-produced one, is given in Table 7. For the wing without as well as with additional segments, the LDM application has improved the L/D (13.7 % and 13.4 %). As expected, the modification of the lift distribution towards an elliptical distribution has reduced the drag fraction of the induced drag.

Table 7: Comparison of overall aircraft aerodynamic performance for reference wing geometries.

Parameter	**Reference AC w/o additional wing seg.**		**rel. Δ orig. vs LDM**	**Reference AC w additional wing seg.**		**rel. Δ orig. vs LDM**	**rel. Δ w/o vs w add. wing seg. orig. twist**	**rel. Δ w/o vs w add. wing seg. LDM twist**
	orig. twist	**LDM twist**		**orig. twist**	**LDM twist**			
$C_{L,opt}$ [-]	0.478	0.466	-2.5%	0.477	0.466	-2.3%	-0.21%	0.00%
L/D_{opt} [-]	18.82	21.39	13.7%	18.86	21.38	13.4%	0.21%	-0.05%
$C_{D,ind}$ fraction [-]	41.1%	31.3%	-23.8%	40.8%	31.3%	-23.3%	-0.73%	0.00%
$C_{D,visc}$ fraction [-]	55.5%	64.3%	15.9%	55.7%	64.3%	15.4%	0.36%	0.00%
$C_{D,wave}$ fraction [-]	3.4%	4.4%	29.4%	3.5%	4.4%	25.7%	2.94%	0.00%

The comparison of both LDM-modified wings shows a very similar L/D ratio. Hence, the impact of introducing the additional wing segments on the aerodynamic performance of the wing is negligible. Therefore, only the reference wing with the added segments will be considered for the remainder of this thesis.

4.1.5 Twist Distribution Adaptation With Database Input

This section will describe the results of applying the 2.5D process on the reference aircraft described in section 3.1.2.3. As described in the previous section, the adaptation towards an elliptical lift distribution reduced induced drag while increasing the local lift coefficient foremost for the outer wing. The first application of the 2.5D methods failed because the maximum value of occurring lift coefficients exceeded the maximum available lift coefficients for the 2D airfoils.
This is due to the elliptical lift distribution representing the induced drag minimum. The aero-structural optimum will incorporate drag components due to separation and compressible effect, as well as a reduction of wing structure mass due to an inboard shift of the lift and reduced wing root bending moment. Identifying the aero structural optimum requires a numerical wing mass calculation, which was unavailable at the time of the thesis. Instead, an approach was chosen that applied a generic and stepwise inboard shift of the elliptic lift distribution by using factors. Figure 75 shows these factors and their trend along the span. The notation η = 0 will be carried on with the factor designation to clarify that the value of the factor is the value applied to the η = 0 position. As shown in Figure 75, the other values for a specific factor deviate from the value it is named by.

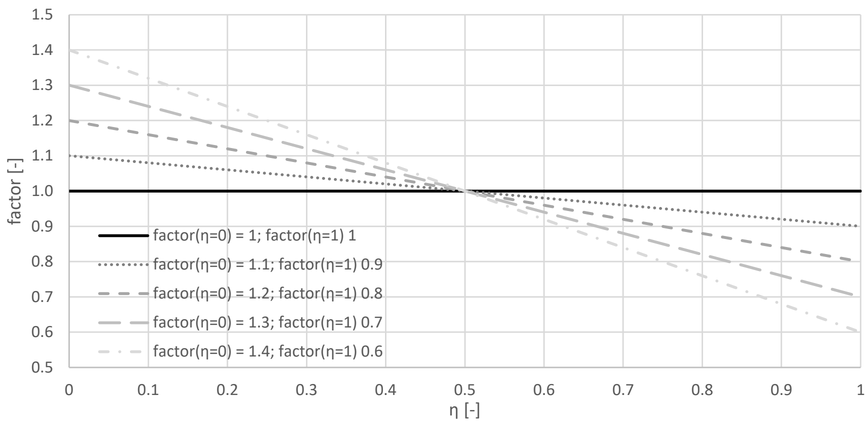

Figure 75: Generic lift coefficient scaling factors.

The resulting lift distributions can be seen in Figure 76. As desired, the lift shifts inboard for an increase of the factor (i.e., increase for $\eta < 0.5$, decrease for $\eta > 0.5$). This reduces the occurring maximum local lift coefficients (see Figure 73).

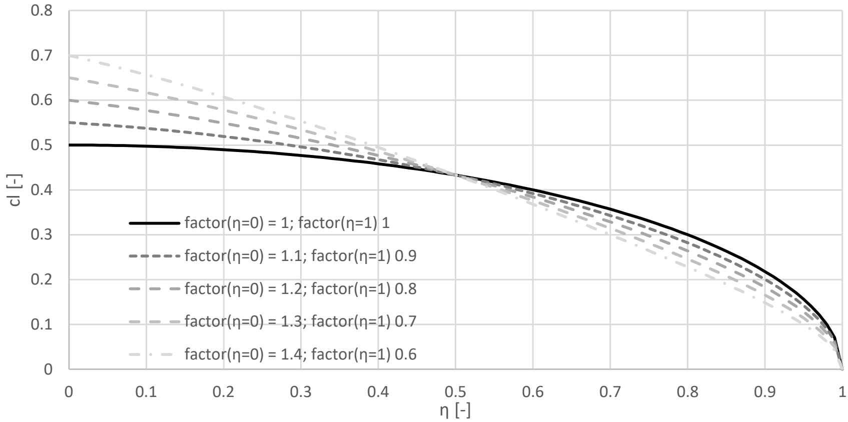

Figure 76: Resulting lift distributions by applying step wise inboard shift on elliptic distribution.

For the selection of the subsequently applied factor, two criteria must be fulfilled:

1. An application of the 2.5D method has to be feasible (i.e. sufficient reduction of maximum local lift coefficients)
2. If possible, selection of the aerodynamic optimum

For this purpose, the factors were applied to the reference aircraft, and the results were compared. Figure 77 displays the optimum L/D and the respective lift coefficient. The pure elliptical lift distribution is present for the factor(η=0)=1.0. No viable overall aircraft polar could be calculated, as previously mentioned for this case. A steady increase in the lift coefficient for which optimum L/D is achieved can be seen, while the maximum L/D occurs with a scaling factor of 1.2.

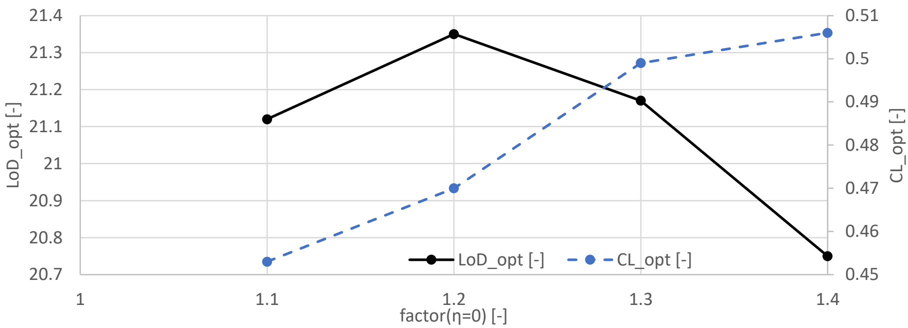

Figure 77: Lift to drag ratio and respective lift coefficient dependent on scaling factors.

The corresponding drag breakdown is shown in Figure 78. A clear rise in induced drag is seen for increasing scaling factors(η=0). This is the expected outcome as the deviation from the elliptic lift distribution becomes stronger with this increase. Furthermore, it is apparent that the combined drag also increases. However, the lift also rises due to the global lift coefficient at which the optimum L/D occurs. Hence, L/D is optimal for a factor(η=0) =1.2 (see Figure 77) while not having the lowest C_D in Figure 78.

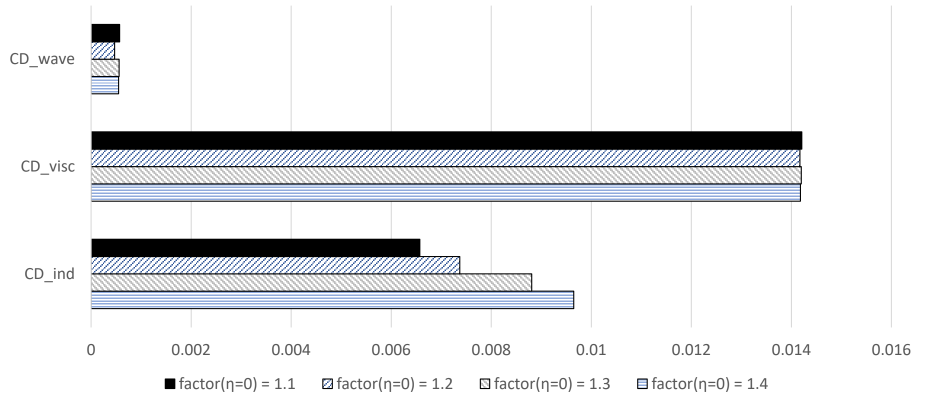

Figure 78: Drag breakdown for the optimum L/D flight condition dependent on scaling factors.

With the 2.5D database method active in the aerodynamic assessment, the aerodynamic characteristics naturally change compared to the results from applying the handbook methods (ref. Table 7). Table 8 compares the reference aircraft with the additional wing segments and the LDM-adapted twist, each for an ellipse shift factor(η=0) =1.2. The optimum L/D is slightly increased while occurring at a marginally higher lift coefficient. The drag reduction stems mainly from a decrease in wave drag.

Table 8: Comparison of overall aircraft aerodynamic performance handbook vs. 2.5D database.

Parameter	**Reference AC factor(η=0) =1.2 handbook**	**Reference AC factor(η=0) =1.2 2.5D database**	**rel. Δ handbook vs 2.5D database**
$C_{L,opt}$ [-]	0.466	0.469	0.6%
L/D_{opt} [-]	21.05	21.34	1.4%
$C_{D,ind}$ fraction [-]	33.0%	33.1%	0.3%
$C_{D,visc}$ fraction [-]	63.3%	64.6%	2.1%
$C_{D,wave}$ fraction [-]	3.7%	2.4%	-35.1%

For the remainder of this thesis, the term reference aircraft will be used for the aircraft resulting from an aerodynamic assessment applying the 2.5D database method and with an ellipse shift factor(η=0) =1.2.

4.2 Derivation of Variable Camber Airfoils

After the completion of the reference wing, the deployed VC airfoils can be created. This includes the creation of their geometry with the process described in section 3.2.1 a preliminary aerodynamic assessment before their integration in the wing and aircraft polars, respectively. The latter is executed to distinguish the causes and effects of airfoil performance and integration.

4.2.1 Geometry of Airfoils with Deployed Trailing Edges

As described in section 3.2.1, creating the deployed airfoils requires several geometric parameters. The source and values of these parameters for the three sections mentioned above used for the VC airfoil creation will be described.

The dimensions of the control surfaces (i.e. flaps and spoilers) were derived from their plan-form, as shown in Figure 49. Since the creation of the airfoils takes place in 2D, only the geometry in the x-z-plane of the specific section is relevant. All x-coordinates are defined as a percentage of the airfoil chord, and the z-coordinates as a percentage of the maximum airfoil thickness. For the spoiler, the leading and trailing edge positions are extracted. The other values necessary are determined by the default values given in section 3.2.1. The ADHF (i.e. the flap panel) size is defined by the leading edge position only since the trailing edge is assumed to be identical to the end of the airfoil. The other important ADHF characteristic is the hinge position. The ADHF hinge position data are the geometric data that carry the highest uncertainty of the geometric data used in this thesis. The applied data were derived from a sketch published by Strüber of the A350 ADHF [13]. However, this sketch was probably modified to protect Airbus intellectual property. Nonetheless, the data have to be used as published due to the lack of alternative data. The ADHF hinge position is defined by its position relative to the airfoil in the x- and z-direction. Another critical parameter for the VC assessment is the available deployment angle of the ADHF. Different values are given in the literature. Nguyen et al. analyse deployments from a downward 8° value for the wing root to a downward 5° at the most outboard flap [69]. Gerzanics states in his Airbus A350 flight test report a +/- deployment of 4° of the inner and outer flap for cruise optimisation [109]. Initial studies conducted before this thesis indicated deployments from +3° downward to -2° upward to provide aerodynamic beneficial results. Since the extent of deployments and the connected cases to be analysed are the main drivers for the computational effort, a deployment range from +4° to -2° with an increment of 0.5° was selected for this thesis. All the described parameters are listed for the specific sections in Table 9.

Table 9: Geometric data for the CDAG airfoil deployment.

parameter	unit	outer kink	inner kink	root
η	-	0.63	0.32	0.09
spoiler leading edge	% of chord	0.737	0.791	0.886
spoiler trailing edge	% of chord	0.891	0.892	0.928
ADHF leading edge	% of chord	0.742	0.803	0.884
ADHF hinge x-position	% of chord	0.754	0.816	0.894
ADHF hinge z-position	% of thickness	-0.094	-0.071	-0.041
downward deployment	°	+4	+4	+4
upward deployment	°	-2	-2	-2
deployment increment	°	0.5	0.5	0.5

The airfoils produced by the CDAG were subsequently processed with the XFOIL PANE command. The PANE command sets the number of panels to 140 and redistributes these according to the curvature. This supports a quicker convergence during the MSES calculations. In some instances, the merged airfoils produced by the CDAG contained two coordinate points close to the merging points of the airfoil, spoiler, and flap. The smoothing algorithm in PANE produced large waves around these points. To avoid this strong geometry deformation, the coordinate with the lower x-coordinate was deleted, eliminating the problem. Further, it must be mentioned that for the application of the CDAG, the native 2D airfoils were incorporated in the reference wing geometry without a 2D to 3D transformation. While this was done to integrate the aircraft performance, this is not necessary for the application of the CDAG since, subsequently, to the CDAG application, an inverse transformation from 3D to 2D would be conducted. Hence, a transformation is not required in the first place. The only impact takes place on the ADHF hinge position. Due to the uncertainty of the hinge position geometry, it was decided not to apply the transformations solely to capture this effect. The most upward and downward deployments of the created airfoils for each span position are depicted in Figure 79. The apparent decrease of deployment from the outboard kink to the root section is due to the abovementioned constant chord of the flap surface. This leads to an increase in the relative chord length of the flap, as well as a different hinge position. Hence, there is an increase in relative deployment for the smaller outer chord of the outer kink compared to the root section.

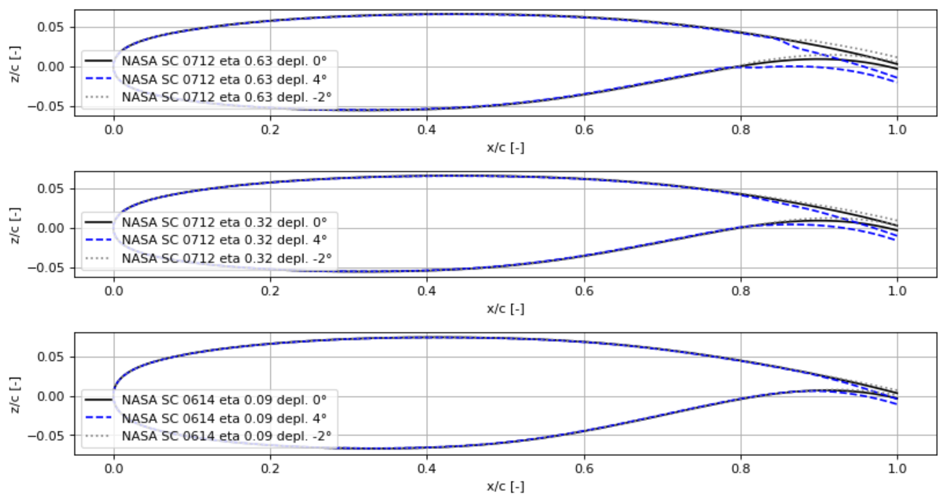

Figure 79: Airfoils created by the CDAG for most upward and downward deployment.

4.2.2 Aerodynamic Assessment of Deployed Airfoils

After the derivation of the deployed airfoil geometries, an assessment of their aerodynamic 2D properties is conducted. This assessment is described in this section and executed for the three spanwise positions (i.e. outer and inner kink and root), focusing on the 2D flow conditions obtained in section 4.1.3.

4.2.2.1 Outer Kink

The first characteristic being considered is the pressure distribution and the impact of the airfoil deployment on it. For the undeployed airfoil and the maximum and minimum deployment, the pressure distribution is shown in Figure 80. On the left ordinate, c_p is given, while the value on the abscissa is the relative x-coordinate of the airfoil, and on the right ordinate, the relative z-coordinate. The airfoil geometry is shown for orientation.

A typical supersonic plateau can be seen for all three airfoils. The plateau extends further back with increasing downward flap deployment while the overall height of the plateau decreases. This is caused by the increased rear loading of an airfoil with increased downward deployment. The aft shift of the shock position and the increase of rear loading with an increase of camber were also described by Szodruch (see comments on [32] in section 2). For the 4° downwards deployed airfoil, a sharp gradient in the pressure distribution can be seen at the position of the spoiler leading edge due to the strong change in airfoil geometry. This area is prone to separation (see Szodruch [34] in section 2) but did not cause separation in this case. However, reducing this gradient would be a target for optimising the airfoil geometry. As the lift coefficient is constant, all airfoils produce the same lift, i.e., the area between the upper and lower cp lines is identical.

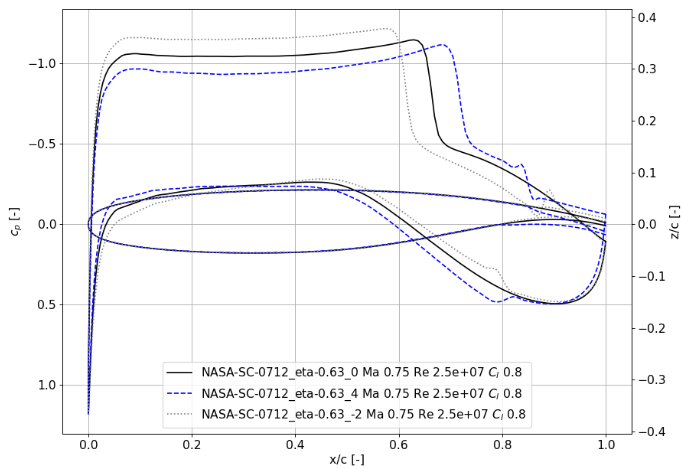

Figure 80: Pressure distribution of deployed airfoils for the outer kink.

The undeployed airfoil with a zero behind the span position (eta) is the airfoil geometry produced by applying the CDAG as described in section 3.2.1 without any deployment applied. The resulting pressure distribution, as shown in Figure 80, was compared to the original NASA SC 0712 airfoil that the CDAG did not process to guarantee consistency. No difference in these pressure distributions could be found, which assures that the introduced changes are only due to the deployment.

The second characteristic is the drag breakdown derived from the MSES calculations. For the reference flow conditions of the outer kink, as displayed in Figure 80, and for all deployments. This breakdown is given in Figure 81. While the total drag coefficient has its minimum for the 1° deployment (i.e. 7.8 % reduction compared to the undeployed airfoil), an almost monotonous trend can be seen for the wave and viscous drag. With the downward deployment of the flap, the wave drag is reduced, and the viscous drag is increased. The reduction of wave drag can be explained by the overall decrease in maximum Ma for increased deployment angles, as seen from the pressure distributions. This leads, in turn, to a weaker shock and lower wave drag. A probable reason for the increase in viscous drag is the increasing extent of the supersonic plateau in a chordwise direction. The effect of a shift of the shock position is described in several papers. Richter and Rosemann describe the lift enhancement by a downstream shifted shock position [120].

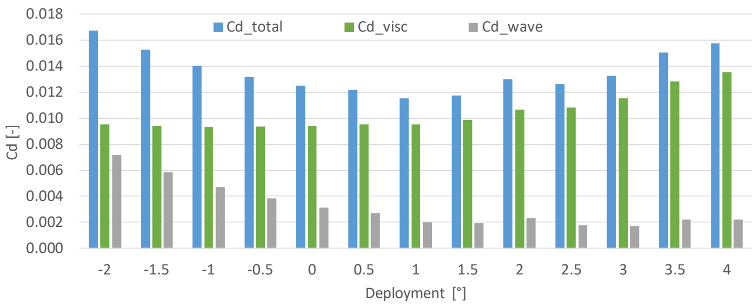

Figure 81: Drag breakdown for the outer kink, C_l 0.8 Ma 0.75 Re 2.5e+07.

The third characteristic that is analysed is the behaviour of the drag in relation to the produced lift, which is shown in Figure 82 with the lift coefficient on the ordinate and the drag coefficient on the abscissa for all created deployments. The red dashed horizontal line indicates the 2D C_l reference value of 0.818, determined in section 4.1.3.1. The expected effect of the deployment is a rotation around a cross-over point, as described by Hilbig et al. [30] and shown in Figure 9, as well as described by other sources (e.g. Krenz [6] and Bolonkin [62]). Although not as focused as in Figure 9, the principal effect can be observed by a gradual cross-over of the lines from -2° to 3.5°, albeit the crossover does not happen at coinciding points but for higher lift coefficients for increasing downward deployment. This effect means a lower drag of higher lift coefficients for higher downward deployment.

While discussing the results of the different deployments for the span positions, it should be stated that deployment degrees are only valid for single explicit airfoils. A flap panel will always be deployed in the subsequent integration with the same deployment angle at its inboard and outboard sections. Hence, the deployment of a panel will be determined by combining the performance of the inner and outer sections.

Due to the availability of drag values for all deployments at the reference lift coefficient in this example, it can be stated that for these specific flow conditions, and if only considering the outer kink sections, the data point of the 1° downward deployed flap offers the best performance.

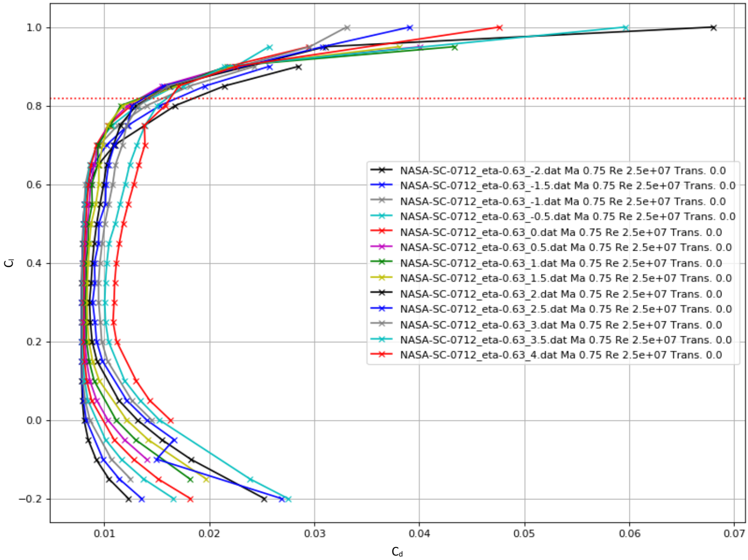

Figure 82 Drag over lift coefficient for all deployments on the outer kink.

For the specific reference flow conditions shown in Figure 82 (i.e. Re and Ma), it can be deduced that downward deployments larger than 2° would not be advantageous for the specific airfoil due to their inferior drag characteristic. These deployments will, however, be implemented in the overall aircraft polar since they might be favourable in different flow conditions.

4.2.2.2 Inner Kink

The pressure distribution for the respective 2D flow conditions (see section 4.1.3.2) of the maximum and minimum airfoil deployment at the inner kink position is shown in Figure 83. The same trend can be seen for the outer root, which comprises a lower maximum pressure difference, shorter supersonic plateau, and higher rear loading for an increase in downward deployment. The well-visible suction peak increases in height with stronger downward deployments, as already described by Gaspari et al. [59] (see section 2). Due to the reduced Ma, the extent of the supersonic plateau is much smaller. The plateau changes its form for the 4° downward deployment, which might appear to have little or no supersonic region.

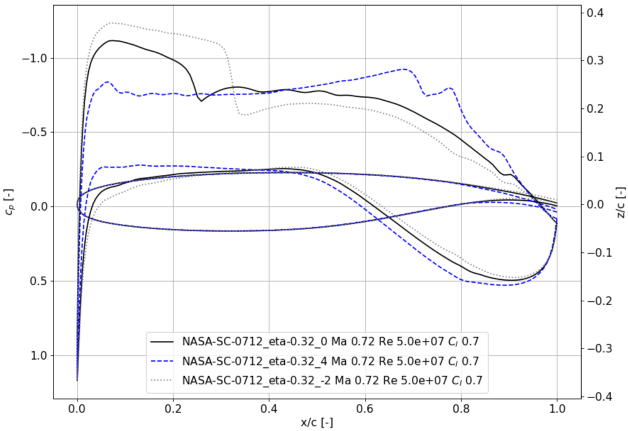

Figure 83: Pressure distribution of deployed airfoils for the inner kink.

To test this assumption, the Ma distributions for these cases are shown in Figure 84. It can be seen that for the 4° downward deployment, Ma 1 is actually reached close to the leading edge. However, the velocity is just over Ma 1.0, and no recompression shock occurs until approximately 70 % chord, and only the second shock at 80 % chord leads to a deceleration under Ma 1.

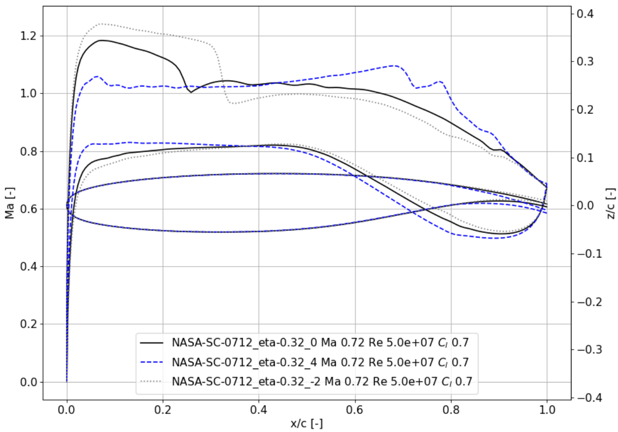

Figure 84: Mach number distribution of deployed airfoils for the inner kink.

In Figure 85, the influence of the reduced Ma is visible in the strongly reduced wave drag. Again, wave drag reduces and viscous drag increases with increasing deployment. The lowest total drag occurs for 0° deployment.

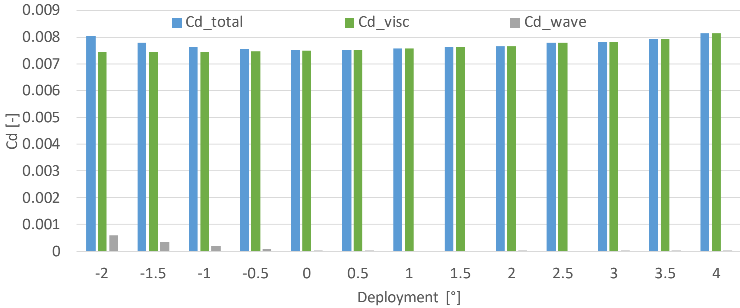

Figure 85: Drag breakdown for the outer kink, C_l 0.7 Ma 0.72 Re 5.0e+07.

Figure 86 shows the C_l over C_d plot for the inner kink with the indicated reference 2D C_l of 0.689. The outer kink crossover occurs at multiple points. Again, for these specific flow conditions, the deployment most beneficial in this particular section can be predicted, and in this case, it is 0° deployment (undeployed).

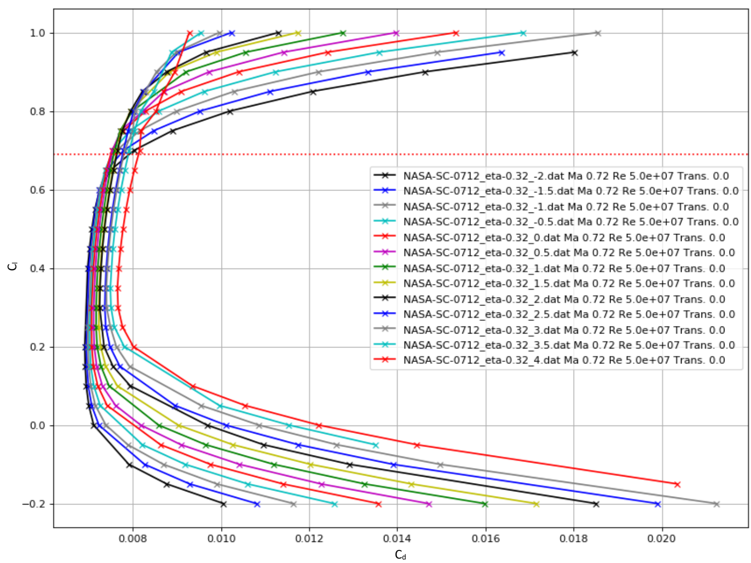

Figure 86: Drag over lift coefficient for all deployments on the inner kink.

4.2.2.3 Root

Figure 87 shows the maximum and minimum deployed airfoils' pressure distribution for the root section. As expected, the difference between the deployments is smaller than for the other span sections due to the smaller absolute change in geometry. However, the same trend can be observed, showing the reduction of maximum pressure difference and an increase in rear loading.

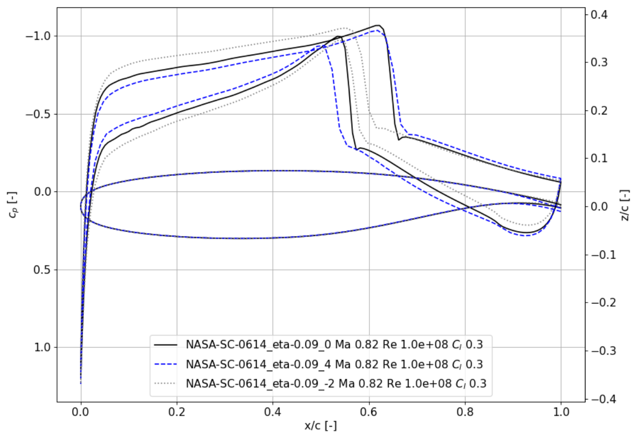

Figure 87: Pressure distribution of deployed airfoils for the root.

The drag breakdown in Figure 88 exhibits gaps for several deployments because it was impossible to achieve convergence in the MSES calculations for several flow conditions and deployments. Nonetheless, the available results show a strong drag increase compared to the outer and inner kink. The trade between wave and viscous drag is still observable but less pronounced and not monotonous. The lowest total drag occurs for the 4° deployment, with a reduction of 6.8 % compared to the undeployed airfoil.

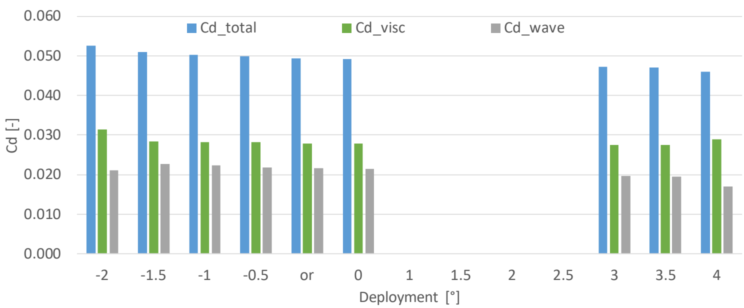

Figure 88: Drag breakdown for the root, C_l 0.3 Ma 0.82 Re 1.0e+08.

The drag characteristics for the reference flow conditions for the root section for all deployments are shown in Figure 89. The difficult convergence behaviour of the root airfoil for the reference flow conditions is reflected in the much less dense distribution of points. Furthermore, it is visible that the drag characteristics feature a rather steep optimum compared to the other sections. In addition, the reference 2D lift coefficient of 0.328 is above the optimum for all deployment angles. This could be expected due to the challenging 2D flow conditions (e.g. Ma) resulting from this airfoil and the shortcomings of a 2.5D method at the root. The 4° downward deployed airfoil has the lowest drag for the reference 2D Cl. However, it has to be pointed out that due to the proximity of the results and the strong fragmentation of the achieved convergence, it is possible that strong and or frequent deployment changes for the root segment could occur during the mission, which might not reflect a real trend in the data.

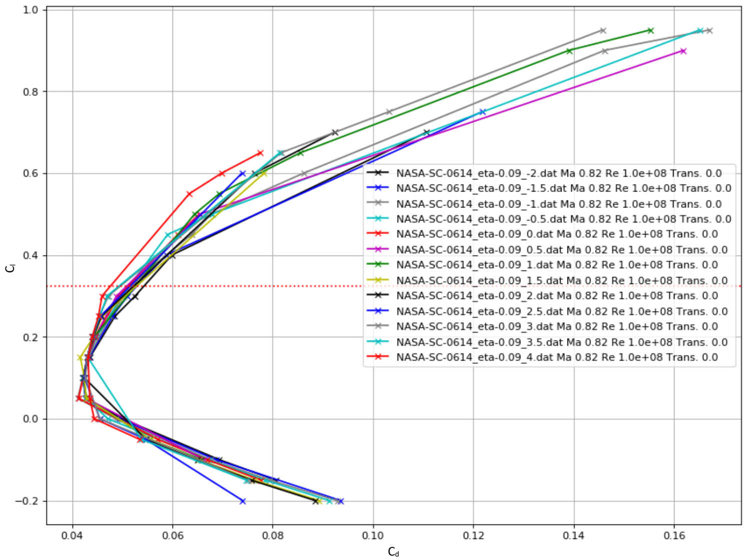

Figure 89: Drag over lift coefficient for all deployments on the root.

The characteristics of the presented section are only a small excerpt from the aerodynamic data created, resulting from the deployments and flow conditions. The database contains data for more Reynolds numbers and more 2D Mach numbers.

4.3 Incorporation of Deployed Airfoils and Polar Merging

This section describes how the deployed airfoils derived in the previous section are incorporated into the merged overall aircraft polars.

4.3.1 Creation of Wing Geometry Permutations

The listed deployment angles in Table 9 for the inner and outer flap (+4° to -2°, 0.5° increments) create a total of $13^2 = 169$ permutations of wing geometries. While it is expected that some combinations can be ruled out beforehand due to, e.g., strong differences in deployment, all permutations were analysed to give a basis for this hypothesis. Figure 90 shows the inner and outer flaps for the highest upward, downward, and zero deployment for the inner and outer flaps.

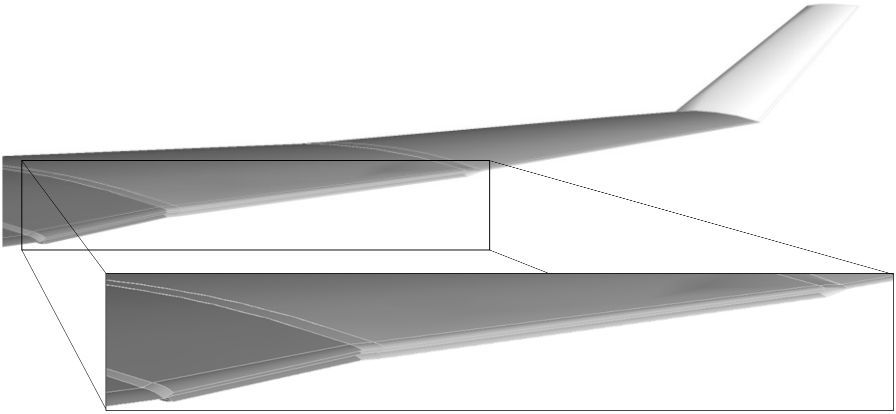

Figure 90: Wing trailing edge with highest/lowest and zero deployment.

The permutations lie within these outer boundaries. The created wing geometries are accurate. However, the aerodynamic performances of the airfoils in the database are accessed by the airfoil file name that is defined in the aircraft.xml (see section 3.1.1). Based on these airfoil names, the 2D aerodynamic data are selected from the database and incorporated into the 2.5D assessment process. Therefore, scripts were written to automatically produce all permutations with the respective deployment angles, wing section airfoils, and aircraft.xml files in which these airfoil names are written in the correct wing geometry definition. Each of the resulting 169 aircraft.xml files is then run through the 2.5D assessment, yielding a 3D wing and overall aircraft polar for that specific set of flap deployment angles.

Since the merged polars are a combination of these, a preview of the behaviour to be expected can be created. For that reason, an excerpt of the permutations is shown in Figure 91. Segment 3 is the inner flap, and segment 5 is the outer flap (see Figure 51). For this excerpt, identical inner and outer flap deployments were chosen. As expected, the maximum L/D for a specific polar occurs at a higher lift coefficient when the camber increases. However, the maximum L/D compared to the polars is highest for the wing without deployed trailing edges. This implies that high deployment angles will most likely not be part of the merged polar since they do not seem to yield a performance increase for the maximum L/D of the entire C_L range.

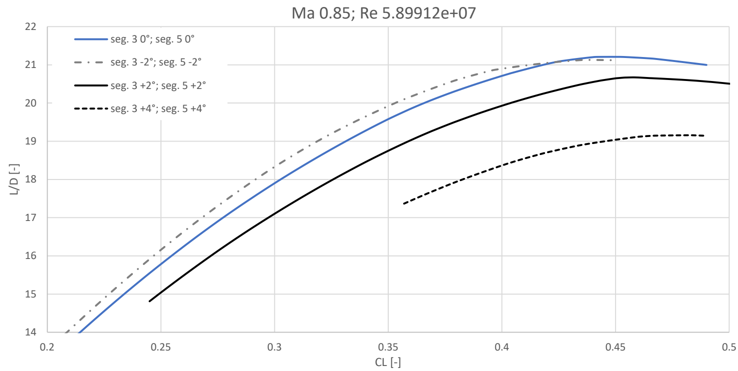

Figure 91: Excerpt of 3D aircraft polars for 4 sets of deployments.

4.3.2 Assessment of Merged Polars

After the 3D polars of all permutations are available, the polar merger (see 3.2.2) is applied. For each point (flight condition) in the polar, the polar (deployment set) is selected with the lowest drag, stored in the merged polar, and the originating polar's flap setting is stored. Figure 92 visualises the number of points selected from combinations of the inner flap (abscissa) and outer flap (ordinate) for a Ma 0.85 and a Re 5.9 * 10^7. A large number of points is selected from the combinations with negative deployments, especially for an inboard deployment of -2° in combination with -2° to -1°. For the outer flap, no deployments larger than 2° are used. As proof of the above-given hypothesis, it can be observed that no combination of upward and downward deployments was selected, which would allow for a strong reduction in the number of analysed permutations in future studies.

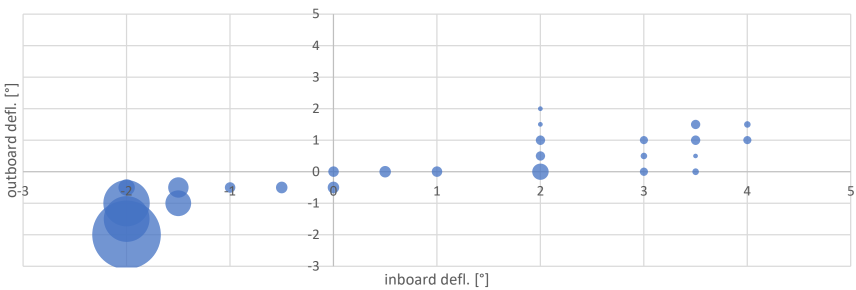

Figure 92: number of used data points for merged polar for deployment set combination.

Figure 93 shows for which lift coefficients the respective deployment combinations have been selected and the resulting L/D. The proximity of the L/D of the merged and the undeployed polar forecasts a very moderate performance increase by the merged polar, hence the application of this specific case of VC incorporation. Furthermore, the representation in Figure 92 contains many points irrelevant to the performance during the cruise segment of the flown mission for which the VC assessment is restricted in this thesis, i.e., outside of the occurring lift coefficients.

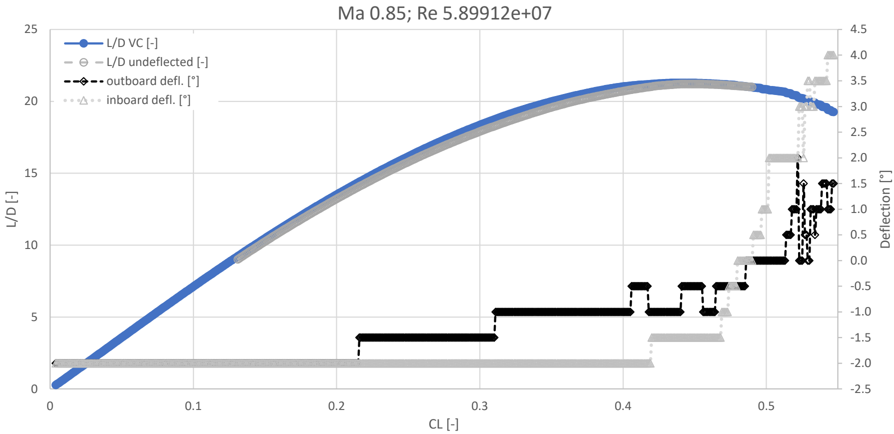

Figure 93: 3D aircraft polar with selected deployment combinations for all lift coefficients

Therefore, Figure 94 shows an excerpt of Figure 93 with a lift coefficient between 0.4 and 0.5, which is the expected band of lift coefficients utilised during the cruise segment of the mission. The scaling of the ordinate has to be considered so as not to overestimate the L/D improvement. The maximum L/D of the undeployed polar is 21.21 versus 21.28 for the merged polar, which is a 0.35 % increase.

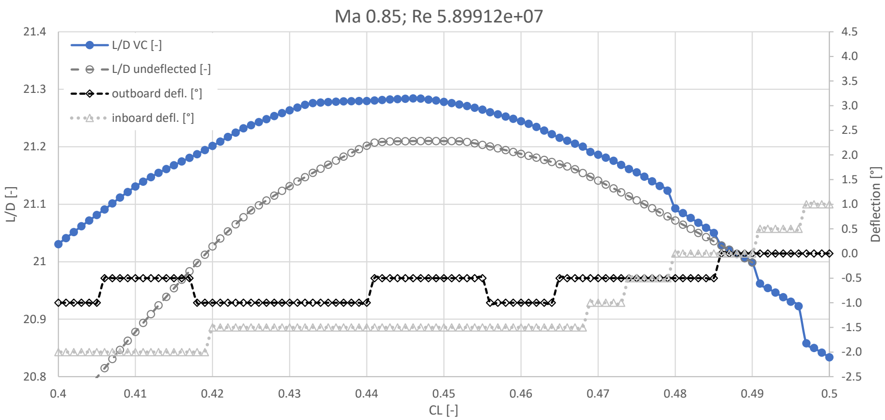

Figure 94: 3D aircraft polar with selected deployment combinations for relevant lift coefficients excerpt

A flatter optimum can be observed, which was also observed by Hilbig et al. [30] (see Section 2 and Figure 11). Both trends represent the expected results but have a low magnitude. The deployment of the inboard flap monotonously increases the deployment angle with an increasing lift coefficient. This is not the case for the outboard flap. An explanation for this could be the non-monotonous results for the outer kink 2D airfoil data for the deployed airfoils (see Figure 82), which in turn could be an outcome of the non-ideal pressure distributions resulting from larger deployments of the outer flap (see Figure 80).

4.4 Performance Assessment on Aircraft Level

This section assesses the aircraft's performance change by incorporating the VC polars for different mission scenarios.

The previous section derived a limited aerodynamic performance impact, which relates to the absolute small fuel changes in this section. For the iteration in the aircraft design loop applied for this section, the convergence limit for the studies executed in this section was set to $1*10^{6}$. This causes the design loop to continue until the change of major parameters (e.g. MTOM and block fuel) is smaller than this convergence limit. This ensures that for delta studies, differences of below 0.1 kg of fuel are not affected by intermediate values occurring during iterations of the studies.

During the execution of the mission analysis tool, it became apparent that the highest available lift coefficients for Ma, 0.85 in the polar of the wing with undeployed flaps (i.e., the reference aircraft), are at 0.49. This is a severe limit regarding the possibility of exploring different mission options. If this limited availability of lift coefficients is due to physical reasons, e.g. stall occurring at parts of the wing and thereby an inability to achieve higher lift coefficients, or MSES could not be brought to convergence, albeit there should be a physical result for these high lift coefficients, it cannot be determined in the scope of this thesis and requires higher fidelity methods. Although substantial efforts have been made at the ILR to expedite the convergence of MSES to high lift coefficients with several strategies, the latter reason cannot be ruled out. Therefore, the undeployed polar has been extended with the merged polar data for lift coefficients upwards of 0.49. As can be seen in the course of this section, these values are only accessed for the reference aircraft in the most extreme missions and only for a short time during runs of the design loop before convergence. Therefore, this extension mainly mitigates the limitations of intermediate results that occur during convergence and does not impact the trends stated in this section, which always represent converged results.

4.4.1 Design Mission Performance

The first application case is the comparison based on the design mission (range 8,000 nmi, payload 30,875 kg, see Table 3). This is done in a two-step fashion, starting with a fixed trajectory and subsequently enabling the trajectory optimisation options of the mission analysis tool (see section 3.1.3).

For the fixed trajectory, both the reference and VC-equipped aircraft travel the same trajectory. Figure 95 shows the altitude and lift coefficient along the range of the mission. The resulting trip fuel for the reference aircraft is 93,832 kg and 93,134 kg for the VC aircraft, which is a 0.74 % reduction. The comparably small fuel benefit is, however small, in the same order of magnitude as the aerodynamic performance increase (see section 4.3.2). In accordance with the moderate difference in trip fuel and hence take-off weight, the graph of the lift coefficient of the reference and VC aircraft is practically identical. The values for all comparisons of this section are tabulated at the end of this section.

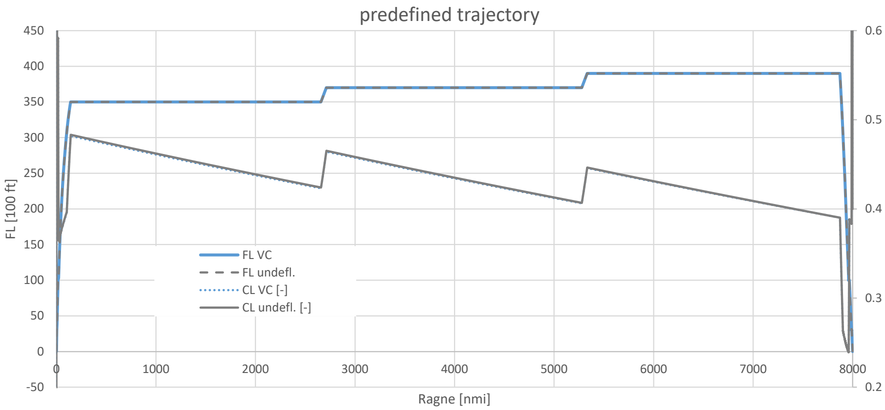

Figure 95: Altitude and C_L for the predefined trajectory for the reference and the VC aircraft.

In the second step, the trajectory is optimised by an optimum selection of the ICA and the optimisation of the flight level changes, which results in the trajectories shown in Figure 96. A reduction of the ICA has been selected for both aircraft, from FL 350 to FL 340 for the reference aircraft and FL 330 for the VC aircraft. Correspondingly, the resulting lift coefficients are higher for the reference aircraft. Trip fuel calculated for the reference aircraft is 93,484 kg and 93,078 kg for the VC aircraft, resulting in a relative decrease of 0.43%. The reduction in fuel difference when enabling trajectory optimisation can be attributed to the possibility of the reference aircraft altering cruise altitude and thereby better avoiding unfavourable lift coefficient ranges.

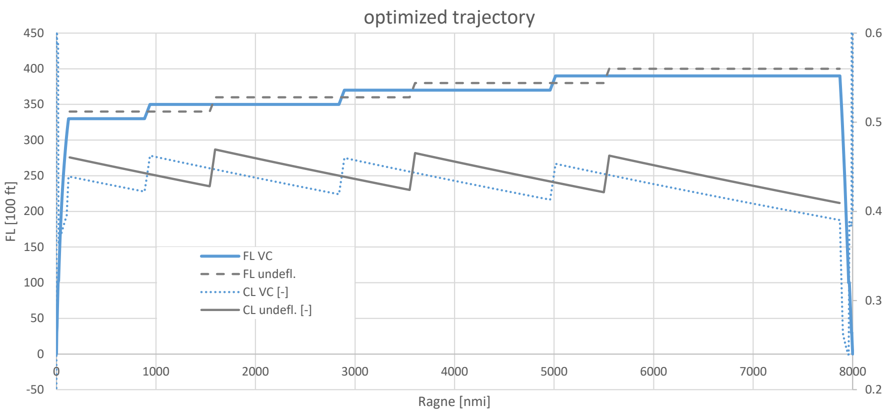

Figure 96: Altitude and C_L for optimised ICA and fixed FL selection for the reference and the VC aircraft.

The flap deployment for the predefined and optimised trajectory and the respective lift coefficients are shown in Figure 97. The deployments track with the lift coefficient values. An increase in camber of the inboard flap can be observed for the slightly higher lift coefficient values occurring for the predefined trajectory. The maximum deployment for the outboard flap during cruise of the predefined mission is 0°, while for the optimised mission, it is -1.5°. This shows that the VC aircraft must use a wider range of the available flap deployments for the predefined trajectory.

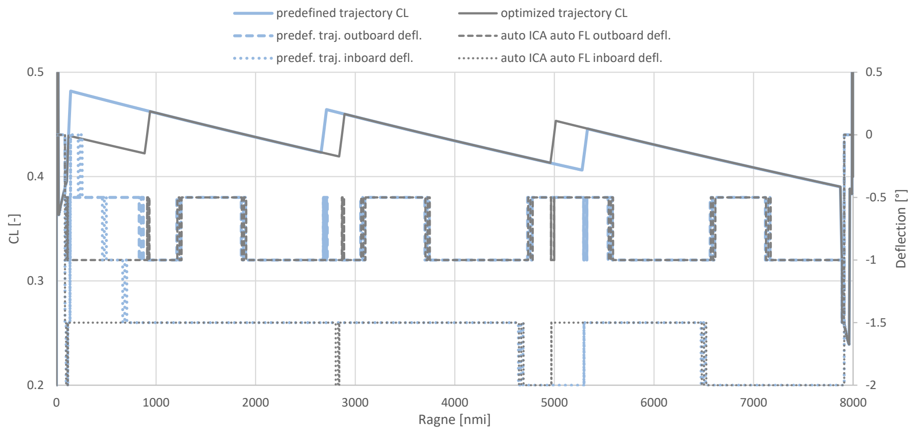

Figure 97: Design mission flap deployments and lift coefficients for predefined and optimised trajectory.

The results from the design mission analysis are comprised in Table 10.

Table 10: Performance parameters of the predefined and optimised design mission.

	trip fuel [kg]	min C_L cruise [-]	max C_L cruise [-]	aver. C_L cruise [-]	min IB depl. [°]	max IB depl. [°]	aver. IB depl. [°]	min OB depl. [°]	max OB depl. [°]	aver. OB depl. [°]
predefined trajectory, undepl.	93832	0.390	0.483	0.435	-	-	-	-	-	-
predefined trajectory, VC	93134	0.390	0.482	0.435	-2.0	0.0	-1.567	-1.0	-0.5	-0.783
rel. Δ undepl. Vs VC	**-0.74%**	0.00%	-0.26%	-0.18%	-	-	-	-	-	-
optimised trajectory, undepl.	93484	0.409	0.469	0.442	-	-	-	-	-	-
optimised trajectory, VC	93078	0.379	0.462	0.431	-2.0	-1.5	-1.609	-1.0	-0.5	-0.828
rel. Δ undepl. Vs VC	**-0.43%**	-7.35%	-1.48%	-2.42%	-	-	-	-	-	-

4.4.2 Performance with Enforced Flight Level Change

As stated before, VC holds the potential to increase operational flexibility. A scenario discussed for several years as a contrail reduction possibility, and thereby the effect on the climate, is the avoidance of specific atmospheric areas that promote contrail creation [121]. The concept is that if conditions are met that are likely to cause contrail creation, a flight level change could negate that and, despite the possible increased fuel consumption, reduce the climate impact of that flight. Avila et al. [122] have published research indicating that with an altitude increase of 2000 ft for such conditions, net radiative forcing could be reduced by 63 %. For a rise of 4000 ft, the reduction was 92 %. This will be taken as a case study, and the performance of the reference and VC aircraft will be compared for the design mission with a flat cruise (i.e., a predefined trajectory).

A flat cruise, and even more so a flat cruise at a suboptimal altitude, will increase fuel demand compared to an optimised trajectory. For this reason, applying this study to the design mission is infeasible since the MTOM would be exceeded due to the necessary fuel. Therefore, the study is used on the average mission length of the A350-900 fleet (see section 3.2.3), which is 2600 nmi. The optimised trajectory for the reference aircraft has been calculated with the design payload to establish a valid baseline cruise altitude. They result in a flat cruise at FL 400 (see Figure 98). Hence, this FL is chosen as a baseline for this section's studies. The service ceiling of the A350-900 is 43.100 ft. Consequently, only the increase of 2000 ft will be analysed. Several circumstances could lead to an unavailability of an increase in cruise altitude (e.g. traffic conflict). For that reason, the alternation of cruise altitude is also executed, decreasing the altitude with several vertical steps. Figure 98 shows the typical missions' optimised trajectory and flat cruise for FL 420 and FL 320, for example, being the highest and lowest analysed flight levels.

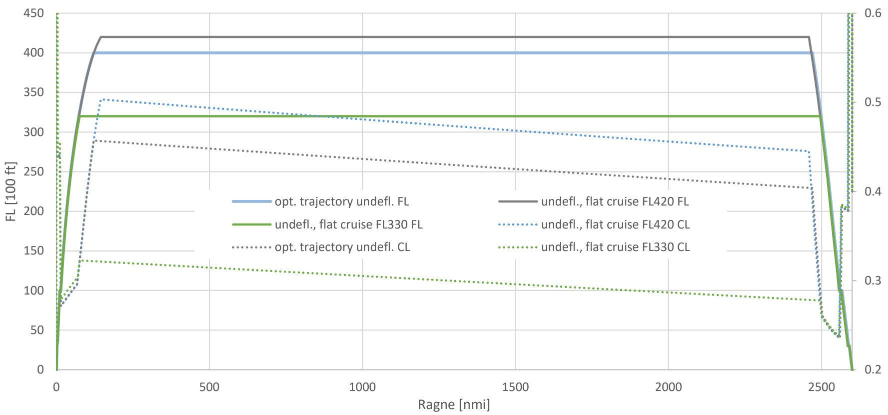

Figure 98: Typical mission altitude and lift coefficient with optimised trajectory and flat cruise examples.

Subsequently, the same flat cruise missions have been executed with the VC aircraft. The inboard and outboard flap deployments for the missions with FL 420 and FL 320 are shown in Figure 99. As expected, the extreme trajectories and corresponding lift coefficients lead to a strong variation in flap deployments. The high lift coefficients that occur in the FL 420 mission result in a wider spread of deployments ranging from -1.5° to 2.0° for the inboard flap, thereby utilising the available deployment span (-2° to 4°, see Table

9) to a large degree. The outboard flap deployments range from -0.5° to 2.0°. In both cases, high values in lift coefficient correlate with high (positive) deployments, leading to an increase in camber.

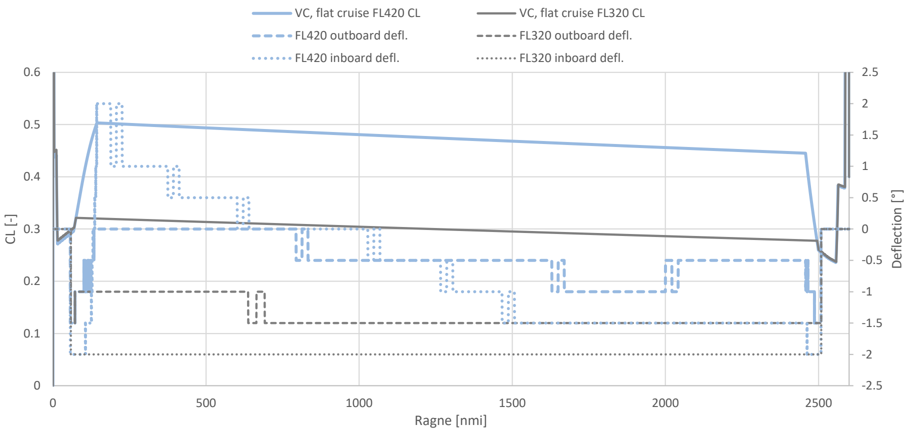

Figure 99: VC Flap deployments and lift coefficients for the flat cruise for FL 430 and FL 330.

Table 11 lists the performance parameters for the typical mission for the optimised trajectory, the flat cruise with FL 420, and the one with FL 320. The optimised trajectories specific to the reference and VC aircraft result in the lowest trip fuel, the relative delta being 0.39 %. Both aircraft commenced a flat cruise for this mission, the aircraft without deployment at FL 400 and the VC aircraft at FL 390. Both aircraft required more fuel for the flat cruise mission at FL 420. The relative delta is small, with 0.23 %. The flat cruise mission with FL 320 is further away in terms of cruise altitude from the optimum trajectory. Hence, trip fuel values for both aircraft increase strongly. Also, the relative delta between the reference and the VC aircraft increased to 2.06 %.

Table 11: Typical mission performance parameters for optimised trajectory and flat cruise examples.

	trip fuel [kg]	min C_L cruise [-]	max C_L cruise [-]	aver. C_L cruise [-]	min IB depl. [°]	max IB depl. [°]	aver. IB depl. [°]	min OB depl. [°]	max OB depl. [°]	aver. OB depl. [°]
optimised trajectory, undepl.	27883	0.404	0.457	0.430	-	-	-	-	-	-
optimised trajectory, VC	27775	0.374	0.436	0.410	-2.0	-1.5	-1.846	-1.0	-0.5	-0.883
rel. Δ undepl. Vs VC	-0.39%	-7.37%	-4.66%	-4.68%	-	-	-	-	-	-
flat cruise FL420, undepl.	28053	0.445	0.503	0.474	-	-	-	-	-	-
flat cruise FL420, VC	27989	0.445	0.503	0.473	-1.5	2.0	-0.583	-1.0	0.0	-0.436
rel. Δ undepl. Vs VC	-0.23%	0.00%	-0.02%	-0.05%	-	-	-	-	-	-
flat cruise FL320, undepl.	32367	0.278	0.323	0.300	-	-	-	-	-	-
flat cruise FL320, VC	31700	0.277	0.321	0.299	-2.0	-2.0	-2.000	-1.5	-1.0	-1.378
rel. Δ undepl. Vs VC	-2.06%	-0.08%	-0.40%	-0.25%	-	-	-	-	-	-

The results for the entire range of cruise altitudes analysed are shown in Table 12. The trend for the whole range of cruise altitudes is visualised in Figure 100. The trend is monotonous over the entire range.

Table 12: Enforced flat cruise fuels for reference and VC aircraft at different altitudes.

	FL 420	FL 400 opt. traj. undepl.	FL 390 opt. traj. VC	FL 380	FL 360	FL 340	FL 320
undepl. trip fuel [kg]	28,053	27,883	28,077	28,420	29,359	30,755	32,367
VC trip fuel [kg]	27,989	27,695	27,775	28,021	28,864	30,149	31,700
Rel. delta [-]	-0.23%	-0.67%	-1.08%	-1.40%	-1.69%	-1.97%	-2.06%

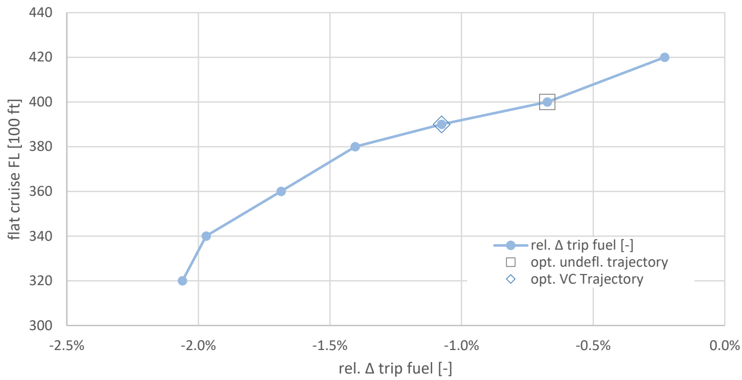

Figure 100: Fuel reduction by VC integration for optimised trajectories and different flat cruise altitudes.

Although the trip fuel reductions by the VC incorporation remain small, they are larger for enforcing suboptimal flight levels. This indicates that VC is better suited to increase operational flexibility rather than improve the basic performance of the reference aircraft. Considering the limited suitability of the baseline airfoil for a VC application, larger benefits by VC are possible if a VC-optimised airfoil is used. Hence, VC could be a key technology for reducing climate impact by contrail avoidance implemented by flight level change.

4.4.3 Impact of System Failure on Fuel Planning

As described in section 3.2.3, for the VC system failure impact assessment on fuel planning, the polar will be changed at specific points of the typical mission at the VC aircraft's optimum flight level (FL 390). The polar that will be activated for the system failure corresponds to the respective flap settings given by the merged VC polar for the flight conditions at this mission point. The analysis will be done for failures at 25 %, 50 % and 75 % of the mission range. The respective data are shown in Table 13.

Table 13:Flight conditions and flap settings for the system failure analysis points.

failure point [% of range]	range [nmi]	altitude [FL]	CL [-]	IB deployment [°]	OB deployment [°]
25	650	390	0.42	-1.50	-1.00
50	1300	390	0.41	-2.00	-0.50
75	1950	390	0.40	-2.00	-1.00

The failure emulates a jam of the VC system, fixing the flap setting to the position at the time of the failure for the remainder of the mission (see the last two columns in Table 13). This could be caused by an asymmetric deployment detected by the asymmetric position pick-off unit and inhibited by the wing tip brakes. Once engaged, the wing tip brakes cannot be released during flight. The corresponding deployment of flaps for the mission with a fully functional VC system and the three failure scenarios are depicted in Figure 101. The red vertical lines indicate the range at which the failures are simulated. The flaps remain in their respective positions after the failure point. It can also be seen that several deployment changes are omitted for the 25 % failure point. For the 50 % failure point, only deployments of the outboard flap are omitted. For the 75 % failure point, no deployment change is omitted. Hence, no impact during the cruise will be observable.

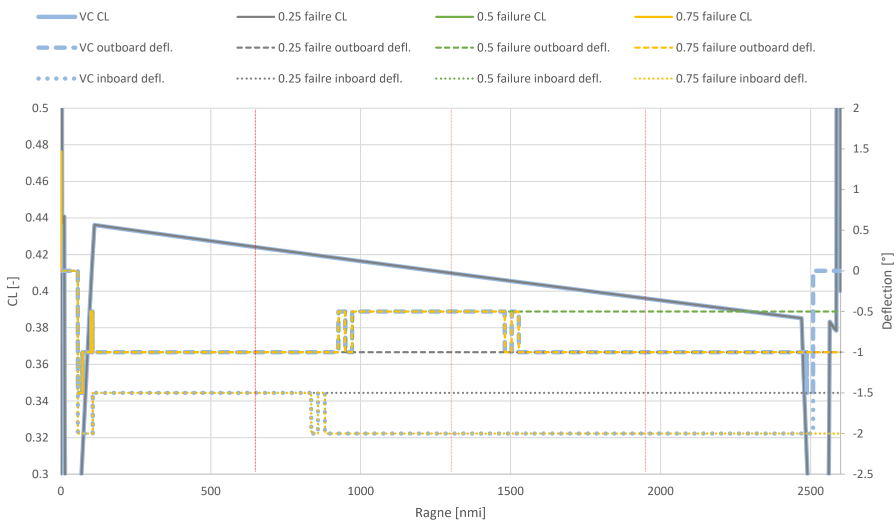

Figure 101: VC Flap deployments and lift coefficients of the system failure simulation.

Table 14 lists the impact of system failures on trip fuel. Since the effects of the VC system were small in the first place, its failure's impact on the short typical mission is also small. The trend, however, is as expected. The 25 % range system failure causes a higher trip fuel than the 50 % range system failure. The 75 % range system failure does not cause any trip fuel difference since it did not alter the flap deployment. In the second last column of Table 14, the absolute delta of the failure simulation versus the fully VC functional mission is listed. These values represent the additional fuel necessary to be carried on board as an additional reserve to account for a respective system failure. It must be pointed out that such a small amount of additional reserve could most likely be covered by the reserves included in conventional fuel planning for adverse weather conditions or similar complications.

Table 14: Fuel impact of system failure for the analysed ranges.

mission specifics	trip fuel [kg]	rel. delta vs no failure [-]	abs. delta vs no failure [kg]	abs. delta vs undeployed [kg]
undeployed flaps	28,077	-	-	-
VC fully functional	27,775	0.00%	-	302
failure at 25% range	27,818	0.15%	43	259
failure at 50% range	27,786	0.04%	11	291
failure at 75% range	27,775	0.00%	0	302

5 Conclusion and Outlook

Conclusion

An extensive literature review showed that VC has been in aviation research and application for over 100 years. The results for applying VC vary between 1 and 10 % drag reduction. A systematic approach to assess VC in conceptual aircraft design was found to be lacking in the current state of the art. Therefore, a respective methodology for assessing VC in conceptual aircraft design has been devised to assess ADHF as VC system architecture.

A reference aircraft has been selected based on the Airbus A350-900 due to its application of the ADHF high-lift system. Substantial efforts were made to prepare this reference aircraft to ensure its suitability for a solid assessment basis. Foremost, this comprised the selection of baseline airfoils suitable for the occurring flow conditions and the optimisation of the twist to achieve an appropriate lift distribution with the analysis methods employed. The former was a challenging task for the airfoils available in the public domain. This became especially clear when the 2.5D method was applied, incorporating compressibility effects, showing the value of these methods' application for this case.

Subsequently, the methodology was applied to the prepared reference aircraft. The derivation of the ADHF geometries from the limited data available on the wing, available in conceptual design, worked as planned. The application of the 2.5D method showed that the selected baseline airfoils were not ideal in their pressure distribution for the VC application. Since the optimisation of the baseline airfoils themselves was out of the scope of this thesis, this limits the suitability of this thesis for the quantification of the absolute benefit to be expected of VC for this specific application case (i.e. this reference aircraft with these baseline airfoils). Information on suggested pressure distributions for VC airfoils has been provided in the literature review section.

The trends originating from the deployment of the 2D airfoils and their succeeding 2.5D integration into, first, the wing and, secondly, the overall aircraft polars showed to be consistent and in line with expectations and literature statements. The concluding assessment on the mission level continued this consistent propagation and yielded small block fuel reductions, which were in line with the pure aerodynamic results. Due to the limited impact of the specific VC implementation, the study on system failure showed a small equivalent impact. Nonetheless, these results again showed the desired behaviour and suitability of the proposed methodology.

The presented methodology was shown to be able to develop an assessment of VC in the form of an ADHF originating from the limited data available in conceptual aircraft design and incorporating crucial aspects in terms of compressibility effects during the aerodynamic evaluation. This assessment was consistent up until the integrated level of the mission analysis. This capability is especially relevant since quantifying operational flexibility (i.e., forced alternative flight levels) is likely to become common practice for contrail avoidance.

Outlook

This section will describe different application cases and possible continuation of the presented methods.

With the presented method, comprehensive studies can be conducted. This could include a clean sheet design of existing aircraft and retrofit aspects. Examples of promising topics could be:

- Reduction of wing area due to the capability to achieve necessary high wing loadings by increased wing camber as necessary for high aircraft masses, i.e. high payload and fuel loads. This could improve performance on ranges below the design range, as they are most common for commercial aviation. This could also be extended to study a family of aircraft, which is often a main factor in defining the wing area.
- An increase in the wing aspect ratio often yields a narrower L/D optimum. An aspect ratio optimisation with and without VC could show the effect of the flattened optimum of L/D of the aircraft.
- A reduction of wing sweep, as suggested in [27], could yield different results with a VC system. The movement of the shock position and severity were also seen in this thesis. Hence, this influence could be leveraged as a respective performance increase due to VC.
- A further segmentation of the trailing edge devices to more finely tune, e.g., the lift distribution, may increase the benefit of VC but has to be assessed, including the possible drawbacks such as weight. (currently, under investigation at ILR, see [123])
- The analysis of different actuation solutions is also an active field of research. Options include conventional hydraulic, electro-hydraulic, and electromechanical actuation and the application of piezoelectric actuators and shape memory alloys. At the German Aerospace Centre, morphing wing elements have been studied intensively since the early 1990s; an overview is given by Sinapius et al. [124]. In 2000, two Ph.D. theses about actuation concepts for the deformation of the wing trailing edge were published. Müller presented the “Hornkonzept” (direct translation: horn concept), which features a tusk-like body inside the flap structure that deforms the flap body by rotation [125]. Monner did a detailed design and testing of the “Fingerkonzept” (direct translation: finger concept), where several segments are combined by rotational joints and covered by skin with a sliding connection [126]. Both concepts were realised in an up-to-scale test rig for the application case of an Airbus A340 and proved feasible. An approach that was based on the finger concept, according to Ricci et al. [127], was developed during the EU SARISTU project and employs similar segmentation but features servo rotary load-bearing actuators with sensing elastic beams for the implementation of signal feedback and individual control of each rib [128]. In further development for the VCCTEF, NASA is specifically looking at shaped memory alloy actuators for the inner flap segments and postulating a large actuation weight reduction [64]. The outer flap segments require a higher actuation speed and are recommended to be actuated electromechanically. The US Air Force Research Laboratory developed a recent conformal mechanism presented by Joo et al., enabling the deformation of non-stretchable skin [129]. The VCCTEF concept is further developed within the FlexSys company, which successfully conducted flight tests on a Gulfstream III and is planning a test on an Air Force Boeing KC-135 [12, 130]. A similar design is presented by Pankonien et al. using shaped memory alloy actuators in combination with piezo-driven actuators for fast actuation [131]. A different actuation approach was proposed by Wildshek et al., featuring a morphing split flap that can act as an aileron, split and crocodile flap [132]. Barbarino et al. give a more extensive overview of research activities in the field of morphing devices [133]. Morphing devices could play a key role in enabling larger control surfaces while allowing for shaping to accommodate design for, e.g. favourable shock location. Larger control surfaces, in turn, could leverage the potential of VC.

Further development options for the methodology are:

- A dedicated variable camber airfoil design would identify the maximum potential of VC. Literature offers several guidelines and examples for a VC-optimised pressure distribution [134, 35, 135, 27]. Wedler also discusses the impact of the spoiler hinge line on the shock position and wave drag [136].
- Next to cruise drag minimisation, Urnes and Nguyen describe additional functionalities for the VCCTEF [66]. This includes compensation for the reduced flutter margin of a flexible wing, the use of VCCTEF for all high-lift flight conditions, and the use of the VCCTEF aft section for roll control and aeroservoelastic control.
- Recently, a method for an integrated aero-structural assessment of the wing was implemented in MICADO. This enables the incorporation of the compromise that must be found for the wing design and can further increase the credibility of the attained optimal wing shapes. Reckzeh states a reduction of "several hundred kilograms wing weight" in the Airbus A350 development by applying an ADHF [1]. Burdette et al. claim a 708 kg wing mass and a 0.36% block fuel reduction with a redesigned wing with morphing trailing edge load relief for manoeuvre load cases applied on the CRM [137]. Rodriguez et al. also identified an increased potential for more flexible wings for the VCCTEF concept compared to a wing with conventional stiffness [104]. Respective wind tunnel experiments backed these results described by Nguyen et al. and Precup et al. [138–140]. Burdette et al. claimed that most of the 5% fuel burn benefit from their study on the CRM stemmed from the wing weight reduction enabled by load inboard shifting for the 2.5g load case [141]. ILR has published preliminary studies in this direction [142–144].
- Several technologies have been suggested to yield strong synergies with VC. The applicability of laminar or hybrid laminar airfoil design was enhanced by VC application [37, 145, 146, 30, 38, 134, 146–148, 136]. Furthermore, the combination of shock control via shock bumps provided a higher potential than these technologies applied on their own [149]. Additional potential for a drag reduction by VC can be expected using the more parabolic deployment shape of the VCCTEF [68]. These aspects would have to be incorporated into the methodology to find the global optimum of the specific technologies.
- The assessment of additional aspects, such as maintenance and reliability, would expand the extent of the operational impact. Vaziry-Zanjany selected VC as a typical high-risk technology in his PhD in 1996 and suggested respective models [47].

6 References

[1] Reckzeh, D., “Multifunctional Wing Moveables: Design Of The A350xwb And The Way To Future Concepts,” *29th Congress of the International Council of the Aeronautical Sciences*, 2014.

[2] Peter, F. N., Risse, K., Schueltke, F., and Stumpf, E., “Variable Camber Impact on Aircraft Mission Planning,” *53rd AIAA Aerospace Sciences Meeting*, 2015.

[3] Peter, F., Stumpf, E., Carossa, G. M., Kintscher, M., Dimino, I., Concilio, A., Pecora, R., and Wildschek, A., “Morphing Value Assessment on Overall Aircraft Level,” *Smart Intelligent Aircraft Structures (SARISTU),* edited by P. C. Wölcken and M. Papadopoulos, 1st ed., Springer International Publishing, Cham, s.l., 2016, pp. 859–871.

[4] Peter, F., and Stumpf, E., “The Development of Morphing Aircraft Benefit Assessment,” *Morphing wing technologies,* edited by A. Concilio, et al., BH Butterworth-Heinemann an imprint of Elsevier, Oxford, Cambridge, MA, 2018, pp. 103–121.

[5] Renken, J. H., and Messerschmitt-Bölkow-Blohm GmbH, “Integration of a Variable Wing Camber Function into an EFCS of a Transport Aircraft,” *Aircraft Design, Systems and Operations Meeting*, 1987.

[6] Krenz, and G., “Transonic Configuration Design,” *Special Course on Subsonic/Transonic Aerodynamic Interference for Aircraft,* AGARD, Neuilly-sur-Seine, 1983.

[7] Schmitt, D., “Die aerodynamische Auslegung des Airbus A300-600,” *DGLR Jahrbuch 1983,* edited by DGLR, 83-123, 1983.

[8] Fielding, J. P., and Vaziry-Zanjany, M. A. F., “Reliability, maintainability and development cost implications of variable camber wings,” *The Aeronautical Journal*; Vol. 1996, May 1996, pp. 183–195.

[9] Rudolph, P., *High-Lift Systems on Commercial Subsonic Airliners*, National Aeronautics and Space Administration, Ames Research Center, 1996.

[10] AIRBUS S.A.S., “A350 high-lift devices combine simplicity with fuel savings,” https://www.airbus.com/newsroom/news/en/2007/08/a350-high-lift-devices-combine-simplicity-with-fuel-savings.html, [retrieved 2 August 2020].

[11] Nguyen, N. T., Precup, N., Livne, E., Urnes, J. M., Dickey, E., Nelson, C., Chiew, J., Rodriguez, D. L., Ting, E., and Lebofsky, S., “Wind Tunnel Investigation of a Flexible Wing High-Lift Configuration with a Variable Camber Continuous Trailing Edge Flap Design,” *33rd AIAA Applied Aerodynamics Conference*, 2015.

[12] Warwick, G., “Morphing Wings Are Still A Long Way From Reality: The promise of morphing aircraft has yet to be realized,” http://aviationweek.com/commercial-aviation/morphing-wings-are-still-long-way-reality, [retrieved 20 January 2016].

[13] Strüber, H., “THE AERODYNAMIC DESIGN OF THE A350 XWB-900 HIGH LIFT SYSTEM,” *29th Congress of the International Council of the Aeronautical Sciences*, 2014.

[14] Culick, F., “Wright Brothers: First Aeronautical Engineers And Test Pilots,” *Forty-Fifth Annual Symposium The Society of Experimental Test Pilots*, 2001.

[15] Parker, H. F., “The Parker Variable Camber Wing: NACA Technical Report 77,” National Advisory Committee for Aeronautics, 1920.

[16] Siewert, R. F., and Whitehead, R. E., “Analysis Of Advanced Variable Camber Concepts,” *AGARD CONFERENCE PROCEEDINGS No. 241*, 1977.

[17] Ferris, J. C., “Wind-Tunnel Investigation of a Variable Camber and Twist Wing,” NASA-TN-D-8475, August 1977.

[18] Boltz, F. W., and Pena, D. F., “Aerodynamic Characteristics of an F-8 Aircraft Configuration with a Variable Camber Wing at Mach Numbers from 0.7 to 1.15,” National Aeronautics and Space

Administration, December 1977, http://ntrs.nasa.gov/archive/nasa/casi.ntrs.nasa.gov/19780007113.pdf, [retrieved 5 February 2016].
[19] Painter, W. D., and Caw, L. J., "Design and Physical Characteristics of the Transonic Aircraft Technology (TACT) Research Aircraft," NASA-TM-56048, Januar 1979, http://www.nasa.gov/centers/dryden/pdf/87897main_H-976.pdf, [retrieved 4 March 2016].
[20] Hardy, R., "AFTI/F-111 mission adaptive wing technology demonstration program," *Aircraft Prototype and Technology Demonstrator Symposium*, 1983, pp. 121–126.
[21] DeCamp, R. W., Hardy, R., and Gould, D. K., "Mission-Adaptive Wing," *International Pacific Air and Space Technology Conference and Exposition*, Vol. 6, SAE International, Warrendale, PA, United States, 1987, pp. 1795–1801.
[22] Goecke Powers, S., Webb, L. D., Friend, E. L., and Lokos, W. A., "Flight Test Results From a Supercritical Mission Adaptive Wing With Smooth Variable Camber: NASA Technical Memorandum 4415," NASA, 1992.
[23] Gilbert, W. W., "Mission Adaptive Wing System for Tactical Aircraft," *Journal of Aircraft*; Vol. 18, No. 7, 1981, pp. 597–602. doi: 10.2514/3.57533.
[24] Gilyard, G., and España, M., "On the Use of Controls for Subsonic Transport Performance Improvement: Overview and Future Directions," National Aeronautics and Space Administration, NASA Technical Memorandum, 1994.
[25] DeCamp, R., and Hardy, R., "Mission adaptive wing advanced research concepts," *11th Atmospheric Flight Mechanics Conference*, 1984, pp. 465–470.
[26] Renken, J. H., "Mission-adaptive wing camber control systems for transport aircraft," *3rd Applied Aerodynamics Conference*, 1985.
[27] Boeing Preliminary Design Deptartment, "Assessment of Variable Camber for Application to Transport Aircraft," National Aeronautics and Space Administration, NASA Technical Report, November 1980, https://ntrs.nasa.gov/archive/nasa/casi.ntrs.nasa.gov/19810003508.pdf, [retrieved 15 July 2017].
[28] Mantel, J., "Leistungssteigernde Modifikationen an transsonischen Tragflügeln von Verkehrsflugzeugen," *Jahrestagung*, DGLR-NR. 82-031, 1982.
[29] Ewald, B. Szodruch, J., "Die aerodynamische Technologieentwicklung für zivile Großflugzeuge," *Luftfahrtforschung und Luftfahrttechnologie*, Vol. 1, 1983, pp. 53–106.
[30] Hilbig, H., Wagner, H., and Messerschmitt-Bölkow-Blohm GmbH/Vereinigte Flugtechnische Werke GmbH, "Variable Wing Camber Control for Civil Transport Aircraft," *14th Congress of the International Council of the Aeronautical Sciences*, 1984, pp. 243–248.
[31] Renken, J., Carl, U., "Konzeptuntersuchungen zu Steuerungssystemen des Tragflügels variabler Wölbung," *Luftfahrtforschung und Luftfahrttechnologie*, 1986, pp. 153–192.
[32] Szodruch, J., "The influence of camber variation on the aerodynamics of civil transport aircraft," *23rd Aerospace Sciences Meeting*, 1985.
[33] Szodruch, J., and Hilbig, R., "Variable wing camber for transport aircraft," *Progress in Aerospace Sciences*; Vol. 25, No. 3, 1988, pp. 297–328. doi: 10.1016/0376-0421(88)90003-6.
[34] Szodruch, J., *Fortschrittliche Tragflügelaerodynamik für Verkehrsflugzeuge*, 1986.
[35] Greff, E., "Aerodynamic Design and Integration of a Variable Camber Wing for a New Generation Long/Medium Range Aircraft," *16th Congress of the International Council of the Aeronautical Sciences*, 1988.
[36] Greff, E., *Funktionsintegrierte Hochauftriebsstrukturen. Anforderungen und Handlungsfelder*, Braunschweig, 30 September 2010.

[37] Greff, E., “The Development and design integration of a variable camber wing for long/medium range aircraft,” *AERONAUTICAL JOURNAL*; Vol. 94, No. 939, 1990, pp. 301–312.
[38] McAvoy, C., and Gopalarathnam, A., “Automated Trailing-Edge Flap for Airfoil Drag Reduction over a Large Lift-Coefficient Range,” *20th AIAA Applied Aerodynamics Conference*, 2002.
[39] Trippensee, G. A., and Lux, D. P., “X-29A Forward-Swept-Wing Flight Research Program Status,” National Aeronautics and Space Administration, NASA Technical Memorandum, November 1987.
[40] Hilbig, R., and Szodruch, J., “The Intelligent Wing - Aerodynamic Developments for Future Transport Aircraft,” *27th Aerospace Sciences Meeting*, 1989.
[41] Monner, H. P., Bein, T., Hanselka, H., and Breitbach, E., “Design Aspects of the Adaptive Wing - The Elastic Trailing Edge and the Local Spoiler Bump,” *RAeS - Multidisciplinary Design and Optimisation Conference*, 1998, 15-1 - 15-9.
[42] Bauer, C., Martin, W., Siegling, H.-F., and Schuermann, H., “A new structural approach to variable camber wing technology of transport aircraft,” *39th AIAA/ASME/ASCE/AHS/ASC Structures, Structural Dynamics, and Materials Conference and Exhibit*, 1998.
[43] Spillman, J. J., “The use of variable camber to reduce drag, weight and costs of transport aircraft,” *AERONAUTICAL JOURNAL*; Vol. 96, No. 951, 1992, pp. 1–9.
[44] Abbott, I. H., and Doenhoff, A. E. von, *Theory of Wing Sections - Including a Summary of Airfoil Data*, Dover Publications, New York, 1959.
[45] Macci, S. H. M., *Structural and Mechanical Feasibility Study of a Variable Camber Wing (VCW) for a transport Aircraft. Ph. D Thesis*, 1992.
[46] Fielding, J. P., Macci, S. H. M., Maclcinnon, A. V., and Stollery, J. L., “The Aerodynamic and Structural Design of a Variable Camber,” *18th Congress of the International Council of the Aeronautical Sciences*, 1992.
[47] Vaziry-Zanjany, M. A. F., *Aircraft Conceptual Design Modelling, Incorporating Reliability, and Maintainability Predictions*, Cranfield University, 1996.
[48] Fielding, J. P., “Design Investigation Of Variable-Camber Flaps For High-Subsonic Airliners,” *22nd Congress of the International Council of the Aeronautical Sciences*, 2000.
[49] Siclari, M., Austin, F., van Nostrand, W., and Volpe, G., “Optimization of segmented flaps for in-flight transonic performance enhancement,” *35th Aerospace Sciences Meeting and Exhibit*, 1997.
[50] Martins, A. L., Catalano F. M., “Viscous Drag Optimization for a Transport Aircraft Mission Adaptive Wing,” *21st Congress of the International Council of the Aeronautical Sciences*, 1998.
[51] Martins, A. L., and Catalano, F. M., “Drag Optimization for Transport Aircraft Mission Adaptive Wing,” *38th Aerospace Sciences Meeting and Exhibit*, 2000.
[52] Martins, A. L., and Catalano, F. M., “Aerodynamic optimization study of a mission adaptive wing for transport aircraft,” *15th Applied Aerodynamics Conference*, 1997.
[53] Martins, A. L., and Ribeiro, R. S., “Aircraft Induced Drag Minimization Using a Constrained Optimization Method,” *20th Congress of the International Council of the Aeronautical Sciences*, 1996, pp. 2549–2557.
[54] Martins, A. L., and Catalano, F. M., “Drag optimization for transport aircraft Mission Adaptive Wing,” *Journal of the Brazilian Society of Mechanical Sciences and Engineering*; Vol. 25, No. 1, 2003, pp. 1–8. doi: 10.1590/S1678-58782003000100001.
[55] Gaspari, A. de, and Ricci, S., “A Two-Level Approach for the Optimal Design of Morphing Wings Based On Compliant Structures,” *Journal of Intelligent Material Systems and Structures*; Vol. 22, No. 10, 2011, pp. 1091–1111. doi: 10.1177/1045389X11409081.
[56] Drela, M., and Youngren, H., “XFOIL User Manual,” http://web.mit.edu/aeroutil_v1.0/xfoil_doc.txt, [retrieved 9 August 2020].

[57] Drela, M., “XFOIL: An Analysis and Design System for Low Reynolds Number Airfoils,” Mueller T.J. (eds) Low Reynolds Number Aerodynamics. Lecture Notes in Engineering vol 54, 1989.

[58] Gaspari, A. de, Ricci, S., Travaglini, L., Cavagna, L., Antunes, A., Odaguil, F., and Lima, G., “Active Camber Morphing Wings Based on Compliant Structures: an Aeroelastic Assessment,” *53rd AIAA Aerospace Sciences Meeting*, 2015.

[59] Gaspari, A. de, Ricci, S., and Riccobene, L., “Design, Manufacturing and Wind Tunnel Test of a Morphing Wing Based on Compliant Structures,” *AIAA Science and Technology Forum and Exposition*, 2016.

[60] Mertens, J., “Next Steps Envisaged to Improve Wing Performance of Commercial Aircrafts,” *Aerodynamic drag reduction technologies,* Springer, Berlin, 2001, pp. 246–255.

[61] Dargel, G., Hansen, H., Wild, J., Streit, T., Rosemann, H., and Richter, K., “Aerodynamische Flügelauslegung mit multifunktionalen Steuerflächen,” *DGLR Jahrbuch 2002,* edited by DGLR, Vol. 1, DGLR, 2002, p. 1605.

[62] Bolonkin, A., and Gilyard, G. B., “Estimated Benefits of Variable-Geometry Wing Camber Control for Transport Aircraft,” NASA/TM-1999-206586, October 1999.

[63] Nguyen, N., “Elastically Shaped Future Air Vehicle Concept,” NASA Ames Research Center, 8 Oct. 2010.

[64] Urnes, Jim, Sr., Nguyen, N., and Dykman, J., *Development of Variable Camber Continuous Trailing Edge Flap System*, Cleveland, OH, United States, 13 March 2012.

[65] Ippolito, C. A., Nguyen, N. T., Totah, J., Trinh, K., and Ting, E. B., “Initial Assessment of a Variable-Camber Continuous Trailing-Edge Flap System for Drag-Reduction of Non-Flexible Aircraft in Steady-State Cruise Condition,” *AIAA Infotech@Aerospace (I@A) Conference*, 2013.

[66] Urnes, J., and Nguyen, N., “A Mission Adaptive Variable Camber Flap Control System to Optimize High Lift and Cruise Lift to Drag Ratios of Future N+3 Transport Aircraft,” *51st AIAA Aerospace Sciences Meeting including the New Horizons Forum and Aerospace Exposition*, 2013.

[67] Lebofsky, S., Ting, E., and Nguyen, N. T., “Multidisciplinary Drag Optimization of Reduced Stiffness Flexible Wing Aircraft With Variable Camber Continuous Trailing Edge Flap,” *56th AIAA/ASCE/AHS/ASC Structures, Structural Dynamics, and Materials Conference*, 2015.

[68] Kaul, U. K., and Nguyen, N. T., “Drag Optimization Study of Variable Camber Continuous Trailing Edge Flap (VCCTEF) Using OVERFLOW,” *32nd AIAA Applied Aerodynamics Conference,* American Institute of Aeronautics and Astronautics, 2014.

[69] Nguyen, N., Lebofsky, S., Ting, E., Kaul, U., Chaparro, D., and Urnes, J., “Development of Variable Camber Continuous Trailing Edge Flap for Performance Adaptive Aeroelastic Wing,” *SAE 2015 AeroTech Congress & Exhibition,* SAE International400 Commonwealth Drive, Warrendale, PA, United States, 2015.

[70] Gundlach, J. F., Tetrault, P.-A., Gern, F. H., Nagshineh-Pour, A. H., Ko, A., Schetz, J. A., Mason, W. H., Kapania, R. K., Grossman, B., and Haftka, R. T., “Conceptual Design Studies of a Strut-Braced Wing Transonic Transport,” *Journal of Aircraft*; Vol. 37, No. 6, 2000, pp. 976–983. doi: 10.2514/2.2724.

[71] Bartels, R. E., Stanford, B., and Waite, J., “Performance Enhancement of the Flexible Transonic Truss-Braced Wing Aircraft Using Variable-Camber Continuous Trailing-Edge Flaps,” *AIAA Aviation 2019 Forum,* American Institute of Aeronautics and Astronautics, 2019.

[72] Xiong, J., Bartels, R. E., and Nguyen, N. T., “Aerodynamic Optimization of Mach 0.745 Transonic Truss-BracedWing Aircraft with Variable-Camber Continuous Trailing-Edge Flap,” *AIAA Science and Technology Forum and Exposition,* American Institute of Aeronautics and Astronautics, 2021.

[73] Reist, T. A., Koo, D., and Zingg, D. W., “Aircraft Cruise Drag Reduction Through Variable Camber Using Existing Control Surfaces,” *Journal of Aircraft*; Vol. 59, No. 6, 2022, pp. 1406–1415. doi: 10.2514/1.C036754.

[74] Risse, K., Anton, E., Lammering, T., Franz, K., and Hoernschemeyer, R., "An Integrated Environment for Preliminary Aircraft Design and Optimization," *53rd AIAA/ASME/ASCE/AHS/ASC Structures, Structural Dynamics and Materials Conference*, 2012.

[75] Risse, K., *Preliminary Overall Aircraft Design with Hybrid Laminar Flow Control*, Shaker Verlag GmbH, Aachen, 2016.

[76] Raymer, D. P., *Aircraft Design: A Conceptual Approach*, American Institute of Aeronautics and Astronautics, Washington, DC, 1992.

[77] Roskam, J., *Airplane design*, DARcorporation, Lawrence, Kan, 1985.

[78] Torenbeek, E., *Synthesis of subsonic airplane design. An introduction to the preliminary design, of subsonic general aviation and transport aircraft, with emphasis on layout, aerodynamic design, propulsion, and performance*, Delft University Press; Nijhoff; Sold and distributed in the U.S. and Canada by Kluwer Boston, Delft, The Hague, Hingham, MA, 1982.

[79] Horstmann, K.-H., *Ein Mehrfach-Traglinienverfahren und seine Verwendung für Entwurf und Nachrechnung nichtplanarer Flügelanordnungen. engl: A multi-lifting line method and its application on design and analysis of nonplanar wing configurations*, Braunschweig, 1987.

[80] Böhnke, D., *A Multi-Fidelity Workflow to Derive Physics-Based Conceptual Design Methods*, Hamburg, 2015.

[81] Lammering, T., Anton, E., and Henke, R., "Validation of a Method for Fast Estimation of Transonic Aircraft Polars and its Application in Preliminary Design," *Aerodynamics Conference 2010*, 2010.

[82] Liersch, C., Wunderlich, and Tobias, "A Fast Aerodynamic Tool for Preliminary Aircraft Design," *12th AIAA/ISSMO Multidisciplinary Analysis and Optimization Conference*, 2008.

[83] Göthert, B. H., "Ebene und räumliche Strömung bei hohen Unterschallgeschwindigkeiten," Jahrbuch der Deutschen Luftfahrtforschung Vol. 1941, No.1, 1941.

[84] Schlichting, H., and Truckenbrodt, E., "Aerodynamik des Flugzeuges: Erster Band: Grundlagen aus der Strömungstechnik Aerodynamik des Tragflügels (Teil I)," 3rd edn., Springer Berlin Heidelberg, Berlin, Heidelberg, 2001, http://dx.doi.org/10.1007/978-3-642-56911-1.

[85] Schlichting, H., and Truckenbrodt, E. A., *Aerodynamik des Flugzeuges. Aerodynamik des Tragflügels (Teil II), des Rumpfes, der Flügel-Rumpf-Anordnung und der Leitwerke,* 3rd edn., Springer, Berlin, 2001.

[86] Busemann, A., "Aerodynamischer Auftrieb bei Überschallgeschwindigkeit," *5th Volta Conference*, 1935.

[87] McLean, D., *Understanding aerodynamics. Arguing from the real physics*, Wiley, Chichester, West Sussex, U.K, 2013.

[88] Boppe, C. W., "Aircraft Drag Analysis Methods: Special Course on Engineer- ing Methods in Aerodynamic Analysis and Design of Aircraft," NATO AGARD Vol. AGARD-R-783, 1992.

[89] Lock, R. C., "An Equivalence Law Relating Three- and Two-Dimensional Pressure Distributions," Aeronautical Research Council Reports and Memoranda Vol. 3346, 1962.

[90] Boppe, C. W., "Computational Aerodynamic Design: X-29, the Gulfstream Series and a Tactical Fighter," SAE Tech. Rep. TP 851789, 1985.

[91] Kaups, K., and Cebeci, T., "Compressible Laminar Boundary Layers with Suction on Swept and Tapered Wings," *Journal of Aircraft*; Vol. 14, No. 7, 1977, pp. 661–667.

[92] Wendt, J. F., and Anderson, J. D., *Computational Fluid Dynamics - An introduction*, Springer, Berlin, Heidelberg, 2009.

[93] Drela, M., *Two-Dimensional Transonic Aerodynamic Design and Analyis using the Euler Equations*, 1985.

[94] Drela, M., "Design and Optimization Method for Multi-Element Airfoils," *Aerospace Design Conference*, 1993.

[95] Drela, M., “A User's Guide to MSES 3.05,” MIT Department of Aeronautics and Astronautics, Juli 2007.
[96] Drela, M., “MSES Multielement Airfoil DesignAnalysis Software - Summary,” Massachusetts Institute of Technology, 1994, https://acdl.mit.edu/drela/msessum.ps.
[97] Schültke, F., and Stumpf, E., “Implementation of an Airfoil Information Database for Usage in Conceptual Aircraft Wing Design Process,” *AIAA Science and Technology Forum and Exposition*, 2019.
[98] Anton, E., Lammering, T., and Henke, R., “A comparative analysis of operations towards fuel efficiency in civil aviation,” *Aerodynamics Conference 2010*, 2010.
[99] Yutko, B. M., and Hansman, R. J., “Approaches To Representing Aircraft Fuel Efficiency Performance For The Purpose Of A Commercial Aircraft Certification Standard,” Massachusetts Institute of Technology International Center for Air Transportation (ICAT), May 2011.
[100] Dorbath, F., *A flexible wing modeling and physical mass estimation system for early aircraft design stages*, Technische Universität Hamburg-Harburg, 2014.
[101] Boever, L., *Prozess zur Auslegung von HLFC-Profilen im Flugzeugvorentwurf*, Aachen, 20 November 2013.
[102] Drela, M., and Youngren, H., “Athena Vortex Lattice (AVL) 3.35 User Guide,” 2013.
[103] AIRBUS S.A.S., “Getting to grips with ETOPS,” 1998.
[104] Rodriguez, D. L., Aftosmis, M. J., Nemec, M., and Anderson, G. R., “Optimized Off-Design Performance of Flexible Wings with Continuous Trailing-Edge Flaps,” *56th AIAA/ASCE/AHS/ASC Structures, Structural Dynamics, and Materials Conference*, 2015.
[105] Schültke, F., Peter, F., Stumpf, E., and Hornung, M., “Prozess zur Profilauswahl für die Flügelauslegung am Beispiel eines A350-900: presentation,” *67. Deutscher Luft- und Raumfahrtkongress*, 2018.
[106] NIU, W., Zhang, Y., Chen, H., and ZHANG, M., “Numerical study of a supercritical airfoil/wing with variable-camber technology,” *Chinese Journal of Aeronautics*; Vol. 33, No. 7, 2020, pp. 1850–1866. doi: 10.1016/j.cja.2020.01.008.
[107] Nelson, T., “787 Systems and Performance,” Boeing Commercial Airplanes, 2005.
[108] Goldhammer, M., *The Next Decade in Commercial Aircraft Aerodynamics Aircraft Aerodynamics. A Boeing Perspective*, Madrid, Spain, 2011.
[109] MIKE GERZANICS, “FLIGHT TEST: Airbus A350-1000 takes growth in its stride,” *Flight Global*.
[110] Reckzeh, D., “Aerodynamic Design of the A400M High-Lift System,” *26th Congress of the International Council of the Aeronautical Sciences*, 2008.
[111] Sutcliffe, M., Reckzeh, D., and Fischer, M., “Hicon Aerodynamics - High Lift Aerodynamic Design For The Future,” *25th Congress of the International Council of the Aeronautical Sciences,* Optimage Ltd, Edinburgh, 2006.
[112] AIRBUS S.A.S., “A350 A350 Aircraft Characteristics Airport and Maintenance Planning,” AIRBUS S.A.S., 1 Jun. 2018, https://www.airbus.com/content/dam/corporate-topics/publications/backgrounders/techdata/aircraft_characteristics/Airbus-Commercial-Aircraft-AC-A350-900-1000.pdf.
[113] Airbus Customer Services, “Airport Operations - AutoCAD 3 view aircraft drawings,” https://www.airbus.com/aircraft/support-services/airport-operations-and-technical-data/autocad-3-view-aircraft-drawings.html.
[114] Vassberg, J., Dehaan, M., Rivers, M., and Wahls, R., “Development of a Common Research Model for Applied CFD Validation Studies,” *26th AIAA Applied Aerodynamics Conference*, 2008.

[115] Kenway, G., Kennedy, G., and Martins, J., “Aerostructural optimization of the Common Research Model configuration,” *AIAA Aviation,* [publisher not identified], [Place of publication not identified], 2014.

[116] Obert, E., *Aerodynamic Design of Transport Aircraft*, IOS Press, Amsterdam, 2009.

[117] Anderson, J. D., *Fundamentals of aerodynamics*, McGraw-Hill Education, New York, NY, 2017.

[118] Harris, C. D., “NASA Supercritical Airfoils: A Matrix of Family-Related Airfoils,” NASA Langley Research Center, 1990.

[119] Lane, K., Marshall, D., and McDonald, R., “Lift Superposition and Aerodynamic Twist Optimization for Achieving Desired Lift Distributions,” *48th AIAA Aerospace Sciences Meeting including the New Horizons Forum and Aerospace Exposition,* [American Institute of Aeronautics and Astronautics], [Reston, VA], 2010.

[120] Richter, K., and Rosemann, K., “Experimental investigation of trailing-edge devices at transonic speeds,” *The Aeronautical Journal* [online], Vol. 106, No. 1058, 2002, pp. 185–193, http://journals.cambridge.org/article_S0001924000012987.

[121] Yin, F., Grewe, V., Frömming, C., and Yamashita, H., “Impact on flight trajectory characteristics when avoiding the formation of persistent contrails for transatlantic flights,” *Transportation Research Part D: Transport and Environment*; Vol. 65, 2018, pp. 466–484. doi: 10.1016/j.trd.2018.09.017.

[122] Avila, D., Sherry, L., and Thompson, T., “Reducing global warming by airline contrail avoidance: A case study of annual benefits for the contiguous United States,” *Transportation Research Interdisciplinary Perspectives*; Vol. 2, 2019, p. 100033. doi: 10.1016/j.trip.2019.100033.

[123] Stephan, R., Schneiders, N., Schueltke, F., Peter, F., and Stumpf, E., “Evaluation of a Distributed Variable-Camber Trailing-Edge Flap System at Preliminary Aircraft Design Stage,” *AIAA AVIATION 2022 Forum,* American Institute of Aeronautics and Astronautics, 2022.

[124] Sinapius, M., Monner, H. P., Kintscher, M., and Riemenschneider, J., “DLR's Morphing Wing Activities within the European Network,” *Procedia IUTAM*; Vol. 10, 2014, pp. 416–426. doi: 10.1016/j.piutam.2014.01.036.

[125] Müller, D., *Das Hornkonzept. Realisierung eines formvariablen Tragflügelprofils zur aerodynamischen Leistungsoptimierung zukünftiger Verkehrsflugzeuge*, Universität Stuttgart, 2000.

[126] Monner, H. P., *Erzielung einer optimierten Tragflügelverwölbungdurch den Einsatz formvariabler Klappenstrukturen*, Braunschweig, Januar 2000.

[127] Ricci, S., Scotti, A., and Terraneo, M., “Design, Manufacturing and Preliminary Test Results of an Adaptive Wing Camber Model,” *47th AIAA/ASME/ASCE/AHS/ASC Structures, Structural Dynamics, and Materials Conference*, 2006.

[128] Pecora, R., Concilio, A., Dimino, I., and Ciminello, M., “Structural Design of an Adaptive Wing Trailing Edge for Enhanced Cruise Performance,” *AIAA Science and Technology Forum and Exposition*, 2016.

[129] Joo, J. J., Marks, C. R., Zientarski, L., and Culler, A. J., “Variable Camber Compliant Wing - Design,” *23nd AIAA/AHS Adaptive Structures Conference*, 2015.

[130] Herrera, C. Y., Spivey, N. D., Ervin, G., and Flick, P., “Aeroelastic Airworthiness Assessment of the Adaptive Compliant Trailing Edge Flaps,” *46th SFTE Annual International Symposium*, 2015.

[131] Pankonien, A. M., Gamble, L., Faria, C., and Inman, D. J., “Synergistic Smart Morphing Aileron: Capabilites Identification,” *AIAA Science and Technology Forum and Exposition*, 2016.

[132] Wildschek, A., Havar, T., and Plötner, K., “An all-composite, all-electric, morphing trailing edge device for flight control on a blended-wing-body airliner,” *Proceedings of the Institution of Mechanical Engineers, Part G: Journal of Aerospace Engineering*; Vol. 224, No. 1, 2009, pp. 1–9. doi: 10.1243/09544100JAERO622.

[133] Barbarino, S., Bilgen, O., Ajaj, R. M., Friswell, M. I., and Inman, D. J., "A Review of Morphing Aircraft," *Journal of Intelligent Material Systems and Structures*; Vol. 22, No. 9, 2011, pp. 823–877. doi: 10.1177/1045389X11414084.

[134] Edi, P., "The Application of Hybrid Laminar Flow Control and Variable Camber Flap as a Flow Control on the Wing for Regional Aircraft Family," *23rd Congress of the International Council of the Aeronautical Sciences*, 2002.

[135] Lyu, Z., and Martins, J. R. R. A., "Aerodynamic Shape Optimization of an Adaptive Morphing Trailing-Edge Wing," *Journal of Aircraft*; Vol. 52, No. 6, 2015, pp. 1951–1970. doi: 10.2514/1.C033116.

[136] Wedler, S., "Analyses regarding Variable Cambering with Spoiler Tracking: Effect of the Flap Hinge Line Location on the Aerodynamic at Transonic Speeds," *64. Deutscher Luft- und Raumfahrtkongress*, 2015.

[137] Burdette, D. A., Kenway, G. K., Lyu, Z., and Martins, J., "Aerostructural Design Optimization of an Adaptive Morphing Trailing Edge Wing," *56th AIAA/ASCE/AHS/ASC Structures, Structural Dynamics, and Materials Conference*, 2015.

[138] Nguyen, N. T., Ting, E., and Lebofsky, S., "Aeroelastic Analysis of Wind Tunnel Test Data of a Flexible Wing with a Variable Camber Continuous Trailing Edge Flap (VCCTEF)," *56th AIAA/ASCE/AHS/ASC Structures, Structural Dynamics, and Materials Conference*, 2015.

[139] Nguyen, N. T., Precup, N., Urnes, J. M., Nelson, C., Lebofsky, S., Ting, E., and Livne, E., "Experimental Investigation of a Flexible Wing with a Variable Camber Continuous Trailing Edge Flap Design," *32nd AIAA Applied Aerodynamics Conference,* American Institute of Aeronautics and Astronautics, 2014.

[140] Precup, N., Livne, E., and Mor, M., "Design, Construction, and Tests of an Aeroelastic Wind Tunnel Model of a Variable Camber Continuous Trailing Edge Flap (VCCTEF) Concept Wing," *32nd AIAA Applied Aerodynamics Conference,* American Institute of Aeronautics and Astronautics, 2014.

[141] Burdette, D. A., Kenway, G. K., and Martins, J., "Performance Evaluation of a Morphing Trailing Edge Using Multipoint Aerostructural Design Optimization," *AIAA Science and Technology Forum and Exposition*, 2016.

[142] Effing, T., Peter, F., Stumpf, E., and Hornung, M., "Approach for the Aerodynamic Optimization of the Twist Distribution of Arbitrary Wing Geometries on Conceptual Aircraft Design Level," *70. Deutscher Luft- und Raumfahrtkongress*, 2021.

[143] Effing, T., Stephan, R., and Stumpf, E., "Influence of a Detailed Mass Estimation for a Wing with known Flight Shape in Conceptual Overall Aircraft Design," *72. Deutscher Luft- und Raumfahrtkongress*, 2023.

[144] Effing, T., Schmitz, V., Schültke, F., Peter, F., and Stumpf, E., "Combined Application of Hybrid Laminar Flow Control and Variable Camber in Preliminary Aircraft Design," *33th Congress of the International Council of the Aeronautical Sciences*, 2022.

[145] Edi, P., and Fielding, J. P., "Civil-Transport Wing Design Concept Exploiting New Technologies," *Journal of Aircraft*; Vol. 43, No. 4, 2006, pp. 932–940. doi: 10.2514/1.15556.

[146] Hetrick, J., Osborn, R., Kota, S., Flick, P., and Paul, D., "Flight Testing of Mission Adaptive Compliant Wing," *48th AIAA/ASME/ASCE/AHS/ASC Structures, Structural Dynamics, and Materials Conference*, 2007.

[147] Youngren, H., "Multi-Point Design and Optimization of an Natural Laminar Flow Airfoil for a Mission Adaptive Compliant Wing," *46th AIAA Aerospace Sciences Meeting and Exhibit*, 2008.

[148] Kota, S., Osborn, R., Ervin, G., Maric, D., Flick, P., and Paul, D., "Mission Adaptive Compliant Wing – Design, Fabrication and Flight Test," FlexSys Inc.; Air Force Research Laboratory, 2009.

[149] Stanewsky, E., and Rosemann, H., "Aspects of Shock Control and Adaptive Wing Technology," *Aerodynamic drag reduction technologies,* Springer, Berlin, 2001, pp. 221–228.

7 Annex

7.1 Variable Camber Airfoil Coordinates

This section contains the coordinates of the airfoils created by the CDAG. The naming contains the original NASA SC airfoil designation, followed by the span position in which it was placed in the reference aircraft, and it concludes with the deployment angle applied to the ADHF for that specific set of coordinates.

NASA-SC-0614_eta-0.09_0.0	
1.00000	0.00330
0.98933	0.00605
0.97259	0.01021
0.95512	0.01437
0.93707	0.01847
0.91846	0.02247
0.89941	0.02649
0.87995	0.03039
0.86016	0.03419
0.84012	0.03788
0.81992	0.04143
0.79961	0.04483
0.77925	0.04808
0.75887	0.05115
0.73848	0.05404
0.71809	0.05676
0.69774	0.05928
0.67744	0.06161
0.65717	0.06372
0.63691	0.06561
0.61659	0.06728
0.59621	0.06874
0.57570	0.07000
0.55508	0.07109
0.53435	0.07200
0.51350	0.07273
0.49252	0.07331
0.47144	0.07374
0.45028	0.07404
0.42911	0.07421
0.40796	0.07425
0.38690	0.07415
0.36591	0.07390
0.34506	0.07350
0.32438	0.07297
0.30397	0.07229
0.28383	0.07144
0.26405	0.07044
0.24471	0.06930
0.22596	0.06804
0.20795	0.06668
0.19083	0.06523
0.17470	0.06370
0.15964	0.06211
0.14570	0.06049
0.13287	0.05886
0.12113	0.05723
0.11041	0.05560
0.10064	0.05398
0.09171	0.05238
0.08354	0.05080
0.07606	0.04924
0.06919	0.04769
0.06285	0.04615
0.05699	0.04463
0.05157	0.04310
0.04653	0.04156
0.04183	0.04001
0.03745	0.03843
0.03337	0.03682
0.02954	0.03517
0.02597	0.03346
0.02264	0.03169
0.01953	0.02987
0.01664	0.02798
0.01396	0.02602
0.01151	0.02397
0.00928	0.02184
0.00729	0.01961
0.00553	0.01730
0.00401	0.01493
0.00275	0.01249
0.00174	0.01000
0.00096	0.00750
0.00042	0.00498
0.00011	0.00248
0.00003	0.00124
0.00000	0.00000
0.00010	-0.00240
0.00039	-0.00478
0.00088	-0.00719
0.00160	-0.00960
0.00252	-0.01199
0.00368	-0.01434
0.00507	-0.01664
0.00669	-0.01886
0.00852	-0.02102
0.01058	-0.02308
0.01285	-0.02506
0.01533	-0.02696
0.01800	-0.02878
0.02088	-0.03052
0.02396	-0.03221
0.02724	-0.03384
0.03074	-0.03541
0.03448	-0.03694
0.03846	-0.03842
0.04271	-0.03986
0.04726	-0.04128
0.05212	-0.04266
0.05735	-0.04403
0.06296	-0.04538
0.06902	-0.04673
0.07556	-0.04809
0.08266	-0.04945
0.09037	-0.05081
0.09877	-0.05219
0.10792	-0.05357
0.11792	-0.05495
0.12883	-0.05633
0.14069	-0.05769
0.15356	-0.05903
0.16744	-0.06032
0.18230	-0.06154
0.19807	-0.06268
0.21467	-0.06371
0.23198	-0.06462
0.24987	-0.06539
0.26823	-0.06602
0.28695	-0.06649
0.30592	-0.06680
0.32505	-0.06696
0.34424	-0.06695
0.36345	-0.06676
0.38262	-0.06639
0.40173	-0.06584
0.42069	-0.06512
0.43946	-0.06419
0.45806	-0.06304
0.47648	-0.06165
0.49480	-0.05997
0.51307	-0.05804
0.53132	-0.05582
0.54961	-0.05331
0.56803	-0.05050
0.58664	-0.04741
0.60547	-0.04404
0.62454	-0.04045
0.64383	-0.03663
0.66334	-0.03260
0.68305	-0.02841
0.70285	-0.02415
0.72252	-0.01990
0.74183	-0.01580
0.76065	-0.01189
0.77888	-0.00825
0.79647	-0.00493
0.81343	-0.00197
0.82978	0.00059
0.84561	0.00273
0.86098	0.00442
0.87598	0.00569
0.89066	0.00651
0.90508	0.00689
0.91929	0.00682
0.93337	0.00629
0.94738	0.00527
0.96143	0.00374
0.97560	0.00166
0.99007	-0.00106
1.00000	-0.00330

NASA-SC-0614_eta-0.09_0.5	
1.00000	0.00237
0.98942	0.00520
0.97312	0.00940
0.95657	0.01350
0.94002	0.01745
0.92340	0.02111
0.90616	0.02491
0.88822	0.02868
0.86969	0.03231
0.85057	0.03590
0.83107	0.03941
0.81131	0.04283
0.79139	0.04610
0.77135	0.04923
0.75124	0.05219
0.73109	0.05499
0.71094	0.05761
0.69082	0.06004
0.67071	0.06227
0.65062	0.06430
0.63052	0.06611
0.61037	0.06770
0.59012	0.06909
0.56976	0.07029
0.54929	0.07132
0.52872	0.07218
0.50805	0.07287
0.48725	0.07339
0.46635	0.07379
0.44540	0.07405
0.42444	0.07420
0.40352	0.07421
0.38268	0.07408
0.36192	0.07380
0.34130	0.07340
0.32087	0.07284
0.30067	0.07214
0.28075	0.07127
0.26119	0.07025
0.24207	0.06910
0.22354	0.06784
0.20575	0.06648
0.18883	0.06503
0.17289	0.06349
0.15800	0.06191
0.14421	0.06029
0.13154	0.05867
0.11993	0.05704
0.10932	0.05542
0.09965	0.05380
0.09080	0.05220
0.08271	0.05062
0.07530	0.04906
0.06848	0.04751
0.06219	0.04598
0.05638	0.04445
0.05100	0.04292
0.04600	0.04138
0.04134	0.03983
0.03700	0.03825
0.03294	0.03663
0.02915	0.03497
0.02562	0.03326
0.02231	0.03150
0.01923	0.02967
0.01637	0.02779
0.01372	0.02582
0.01130	0.02378
0.00910	0.02165
0.00714	0.01942
0.00540	0.01713
0.00392	0.01476
0.00269	0.01234
0.00170	0.00988
0.00094	0.00740
0.00041	0.00491
0.00010	0.00244
0.00003	0.00122
0.00000	0.00000
0.00010	-0.00241
0.00039	-0.00480
0.00089	-0.00722
0.00161	-0.00965
0.00255	-0.01205
0.00372	-0.01442
0.00513	-0.01674
0.00678	-0.01899
0.00865	-0.02116
0.01076	-0.02324
0.01308	-0.02523
0.01561	-0.02715
0.01834	-0.02899
0.02129	-0.03075
0.02444	-0.03246
0.02782	-0.03409
0.03142	-0.03568
0.03524	-0.03723
0.03937	-0.03873
0.04376	-0.04019
0.04846	-0.04161
0.05351	-0.04302
0.05893	-0.04440
0.06477	-0.04579
0.07109	-0.04716
0.07793	-0.04854
0.08537	-0.04993
0.09346	-0.05132
0.10230	-0.05271
0.11195	-0.05412
0.12249	-0.05553
0.13400	-0.05692
0.14652	-0.05829
0.16006	-0.05963
0.17462	-0.06092
0.19013	-0.06211
0.20653	-0.06320
0.22372	-0.06418
0.24156	-0.06503
0.25991	-0.06573
0.27867	-0.06627
0.29772	-0.06666
0.31698	-0.06688
0.33633	-0.06694
0.35573	-0.06682
0.37511	-0.06652
0.39444	-0.06604
0.41364	-0.06538
0.43269	-0.06452
0.45155	-0.06344
0.47024	-0.06211
0.48881	-0.06051
0.50730	-0.05864
0.52576	-0.05648
0.54425	-0.05403
0.56283	-0.05127
0.58159	-0.04821
0.60055	-0.04489
0.61973	-0.04132
0.63912	-0.03752
0.65873	-0.03350
0.67852	-0.02932
0.69842	-0.02504
0.71823	-0.02076
0.73776	-0.01659
0.75682	-0.01261
0.77534	-0.00889
0.79323	-0.00547
0.81048	-0.00241
0.82713	0.00025
0.84322	0.00247
0.85883	0.00425
0.87404	0.00557
0.88888	0.00644
0.90343	0.00679
0.91785	0.00664
0.93215	0.00603
0.94640	0.00490
0.96069	0.00324
0.97512	0.00103
0.98983	-0.00186
1.00000	-0.00422

NASA-SC-0614_eta-0.09_-0.5	
1.00000	0.00422
0.98945	0.00685
0.97305	0.01077
0.95612	0.01465
0.93892	0.01842
0.92148	0.02209
0.90335	0.02583
0.88451	0.02958
0.86521	0.03331
0.84560	0.03696
0.82574	0.04049
0.80575	0.04389
0.78568	0.04714
0.76555	0.05023
0.74540	0.05314
0.72524	0.05588
0.70510	0.05845
0.68500	0.06082
0.66494	0.06298
0.64489	0.06494
0.62482	0.06668
0.60468	0.06819
0.58444	0.06953
0.56408	0.07067
0.54362	0.07165
0.52304	0.07245
0.50234	0.07309
0.48153	0.07358
0.46063	0.07394
0.43968	0.07417
0.41874	0.07428
0.39786	0.07424
0.37703	0.07407
0.35634	0.07376
0.33578	0.07331
0.31542	0.07272
0.29534	0.07197
0.27556	0.07107
0.25615	0.07002
0.23724	0.06884
0.21896	0.06755
0.20146	0.06617
0.18486	0.06470
0.16926	0.06316
0.15473	0.06157
0.14131	0.05996
0.12897	0.05834
0.11767	0.05673
0.10736	0.05513
0.09795	0.05353
0.08934	0.05195
0.08145	0.05038
0.07421	0.04884
0.06754	0.04732
0.06140	0.04580
0.05571	0.04428
0.05042	0.04277
0.04551	0.04124
0.04093	0.03970
0.03666	0.03814
0.03266	0.03653
0.02892	0.03489
0.02543	0.03319
0.02216	0.03144
0.01912	0.02962
0.01629	0.02774
0.01367	0.02579
0.01126	0.02375
0.00908	0.02163
0.00712	0.01942
0.00541	0.01713
0.00393	0.01477
0.00269	0.01236
0.00170	0.00990
0.00094	0.00742
0.00042	0.00493
0.00010	0.00245
0.00003	0.00123
0.00000	0.00000
0.00010	-0.00242
0.00040	-0.00483
0.00090	-0.00727
0.00163	-0.00971
0.00259	-0.01212
0.00377	-0.01449
0.00518	-0.01681
0.00683	-0.01906
0.00871	-0.02122
0.01082	-0.02331
0.01314	-0.02529
0.01567	-0.02720
0.01840	-0.02903
0.02134	-0.03079
0.02448	-0.03249
0.02784	-0.03412
0.03142	-0.03571
0.03524	-0.03724
0.03932	-0.03873
0.04369	-0.04018
0.04835	-0.04160
0.05336	-0.04300
0.05873	-0.04438
0.06452	-0.04575
0.07077	-0.04712
0.07754	-0.04849
0.08489	-0.04987
0.09289	-0.05125
0.10162	-0.05265
0.11114	-0.05404
0.12156	-0.05543
0.13292	-0.05683
0.14528	-0.05820
0.15868	-0.05953
0.17309	-0.06082
0.18849	-0.06202
0.20479	-0.06313
0.22188	-0.06412
0.23966	-0.06498
0.25797	-0.06571
0.27670	-0.06627
0.29575	-0.06667
0.31503	-0.06691
0.33440	-0.06700
0.35383	-0.06690
0.37323	-0.06662
0.39259	-0.06615
0.41183	-0.06551
0.43091	-0.06467
0.44979	-0.06363
0.46848	-0.06233
0.48705	-0.06076
0.50553	-0.05892
0.52399	-0.05679
0.54246	-0.05438
0.56102	-0.05166
0.57975	-0.04864
0.59870	-0.04534
0.61789	-0.04179
0.63731	-0.03800
0.65696	-0.03400
0.67683	-0.02981
0.69683	-0.02552
0.71677	-0.02121
0.73642	-0.01701
0.75560	-0.01299
0.77424	-0.00923
0.79222	-0.00577
0.80956	-0.00267
0.82629	0.00003
0.84247	0.00229
0.85819	0.00412
0.87353	0.00548
0.88862	0.00640
0.90348	0.00695
0.91804	0.00706
0.93241	0.00668
0.94667	0.00579
0.96094	0.00438
0.97534	0.00241
0.98999	-0.00020
1.00000	-0.00238

NASA-SC-0614_eta-0.09_1.5	
1.00000	0.00051
0.98928	0.00358
0.97276	0.00814
0.95589	0.01262
0.93899	0.01694
0.92189	0.02085
0.90438	0.02495
0.88657	0.02887
0.86809	0.03246
0.84892	0.03606
0.82933	0.03958
0.80942	0.04301
0.78930	0.04631
0.76905	0.04946
0.74871	0.05243
0.72832	0.05524
0.70791	0.05787
0.68752	0.06032
0.66716	0.06255
0.64680	0.06457
0.62643	0.06637
0.60600	0.06794
0.58545	0.06930
0.56480	0.07049
0.54405	0.07148
0.52317	0.07231
0.50219	0.07296
0.48108	0.07346
0.45988	0.07382
0.43865	0.07406
0.41744	0.07416
0.39626	0.07412
0.37516	0.07394
0.35418	0.07362
0.33335	0.07315
0.31273	0.07254
0.29238	0.07176
0.27234	0.07081
0.25269	0.06972
0.23356	0.06851
0.21509	0.06718
0.19745	0.06576
0.18077	0.06425
0.16513	0.06266
0.15061	0.06103
0.13722	0.05938
0.12495	0.05773
0.11375	0.05608
0.10353	0.05443
0.09422	0.05280
0.08572	0.05119
0.07794	0.04960
0.07080	0.04803
0.06424	0.04647
0.05819	0.04492
0.05259	0.04337
0.04741	0.04181
0.04258	0.04023
0.03809	0.03864
0.03390	0.03701
0.02999	0.03534
0.02634	0.03362
0.02294	0.03184
0.01977	0.03000
0.01683	0.02809
0.01411	0.02611
0.01162	0.02405
0.00936	0.02190
0.00734	0.01966
0.00556	0.01734
0.00403	0.01495
0.00276	0.01250
0.00174	0.01000
0.00096	0.00749
0.00042	0.00497
0.00011	0.00247
0.00003	0.00124
0.00000	0.00000
0.00010	-0.00238
0.00038	-0.00474
0.00087	-0.00714
0.00157	-0.00953
0.00249	-0.01191
0.00364	-0.01426
0.00502	-0.01655
0.00663	-0.01878
0.00846	-0.02094
0.01051	-0.02301
0.01279	-0.02499
0.01527	-0.02690
0.01796	-0.02873
0.02084	-0.03049
0.02394	-0.03218
0.02724	-0.03381
0.03077	-0.03540
0.03454	-0.03693
0.03856	-0.03843
0.04285	-0.03987
0.04745	-0.04130
0.05237	-0.04269
0.05765	-0.04407
0.06335	-0.04543
0.06949	-0.04680
0.07613	-0.04817
0.08334	-0.04954
0.09118	-0.05091
0.09973	-0.05230
0.10905	-0.05369
0.11923	-0.05508
0.13033	-0.05646
0.14241	-0.05783
0.15550	-0.05916
0.16959	-0.06045
0.18464	-0.06167
0.20058	-0.06279
0.21732	-0.06380
0.23473	-0.06469
0.25271	-0.06543
0.27113	-0.06603
0.28987	-0.06647
0.30885	-0.06676
0.32797	-0.06689
0.34714	-0.06685
0.36632	-0.06663
0.38547	-0.06623
0.40453	-0.06566
0.42345	-0.06490
0.44221	-0.06394
0.46078	-0.06275
0.47921	-0.06130
0.49753	-0.05958
0.51583	-0.05759
0.53410	-0.05532
0.55244	-0.05275
0.57089	-0.04989
0.58952	-0.04674
0.60838	-0.04333
0.62745	-0.03970
0.64671	-0.03585
0.66618	-0.03181
0.68580	-0.02763
0.70545	-0.02338
0.72494	-0.01918
0.74407	-0.01513
0.76271	-0.01128
0.78077	-0.00770
0.79819	-0.00444
0.81499	-0.00156
0.83118	0.00093
0.84683	0.00299
0.86200	0.00461
0.87672	0.00580
0.89105	0.00652
0.90510	0.00659
0.91913	0.00616
0.93310	0.00528
0.94708	0.00391
0.96113	0.00201
0.97534	-0.00044
0.98986	-0.00356
1.00000	-0.00608

NASA-SC-0614_eta-0.09_-1.5	
1.00000	0.00606
0.98934	0.00852
0.97265	0.01220
0.95525	0.01587
0.93724	0.01948
0.91879	0.02315
0.90024	0.02672
0.88160	0.03029
0.86269	0.03396
0.84335	0.03752
0.82373	0.04099
0.80390	0.04434
0.78397	0.04755
0.76396	0.05060
0.74390	0.05347
0.72382	0.05620
0.70378	0.05873
0.68374	0.06107
0.66374	0.06321
0.64374	0.06514
0.62373	0.06686
0.60366	0.06836
0.58346	0.06967
0.56315	0.07080
0.54275	0.07176
0.52223	0.07255
0.50160	0.07318
0.48086	0.07366
0.46003	0.07401
0.43917	0.07424
0.41831	0.07434
0.39751	0.07429
0.37676	0.07413
0.35615	0.07381
0.33567	0.07336
0.31538	0.07276
0.29535	0.07201
0.27561	0.07111
0.25625	0.07006
0.23737	0.06888
0.21911	0.06760
0.20162	0.06623
0.18503	0.06476
0.16943	0.06321
0.15488	0.06163
0.14142	0.06001
0.12906	0.05839
0.11774	0.05677
0.10739	0.05516
0.09795	0.05356
0.08932	0.05197
0.08141	0.05040
0.07415	0.04885
0.06747	0.04733
0.06131	0.04580
0.05561	0.04429
0.05032	0.04276
0.04540	0.04124
0.04082	0.03969
0.03654	0.03811
0.03255	0.03650
0.02881	0.03485
0.02532	0.03315
0.02206	0.03139
0.01901	0.02957
0.01619	0.02768
0.01357	0.02573
0.01118	0.02368
0.00901	0.02156
0.00706	0.01935
0.00535	0.01707
0.00389	0.01471
0.00266	0.01229
0.00168	0.00984
0.00093	0.00737
0.00041	0.00490
0.00010	0.00244
0.00002	0.00122
0.00000	0.00000
0.00010	-0.00240
0.00039	-0.00479
0.00089	-0.00721
0.00161	-0.00963
0.00254	-0.01203
0.00371	-0.01439
0.00510	-0.01671
0.00674	-0.01895
0.00860	-0.02111
0.01068	-0.02319
0.01298	-0.02518
0.01549	-0.02709
0.01820	-0.02893
0.02112	-0.03069
0.02425	-0.03239
0.02759	-0.03403
0.03116	-0.03561
0.03496	-0.03715
0.03902	-0.03865
0.04337	-0.04010
0.04801	-0.04153
0.05299	-0.04293
0.05834	-0.04431
0.06410	-0.04569
0.07033	-0.04705
0.07707	-0.04843
0.08438	-0.04981
0.09234	-0.05119
0.10102	-0.05258
0.11050	-0.05398
0.12085	-0.05538
0.13214	-0.05677
0.14444	-0.05814
0.15775	-0.05948
0.17207	-0.06077
0.18738	-0.06198
0.20356	-0.06310
0.22054	-0.06410
0.23820	-0.06497
0.25639	-0.06570
0.27501	-0.06628
0.29396	-0.06669
0.31312	-0.06695
0.33240	-0.06706
0.35173	-0.06698
0.37105	-0.06672
0.39033	-0.06628
0.40951	-0.06566
0.42855	-0.06486
0.44739	-0.06385
0.46605	-0.06259
0.48457	-0.06107
0.50300	-0.05928
0.52140	-0.05721
0.53980	-0.05485
0.55828	-0.05219
0.57690	-0.04923
0.59573	-0.04600
0.61477	-0.04250
0.63405	-0.03879
0.65353	-0.03485
0.67322	-0.03073
0.69304	-0.02648
0.71285	-0.02219
0.73247	-0.01799
0.75171	-0.01393
0.77042	-0.01011
0.78857	-0.00658
0.80611	-0.00338
0.82306	-0.00057
0.83949	0.00181
0.85550	0.00376
0.87114	0.00524
0.88668	0.00626
0.90210	0.00704
0.91706	0.00746
0.93174	0.00736
0.94624	0.00673
0.96070	0.00556
0.97525	0.00383
0.99004	0.00147
1.00000	-0.00054

NASA-SC-0614_eta-0.09_1.0	
1.00000	0.00144
0.98929	0.00441
0.97268	0.00884
0.95564	0.01322
0.93846	0.01743
0.92104	0.02132
0.90322	0.02538
0.88500	0.02926
0.86613	0.03292
0.84669	0.03654
0.82690	0.04008
0.80686	0.04350
0.78666	0.04679
0.76635	0.04992
0.74599	0.05288
0.72560	0.05566
0.70520	0.05827
0.68485	0.06068
0.66450	0.06288
0.64418	0.06486
0.62383	0.06662
0.60341	0.06817
0.58289	0.06950
0.56224	0.07065
0.54150	0.07163
0.52064	0.07243
0.49967	0.07306
0.47857	0.07354
0.45739	0.07389
0.43618	0.07410
0.41498	0.07419
0.39384	0.07414
0.37279	0.07394
0.35183	0.07359
0.33106	0.07311
0.31049	0.07247
0.29019	0.07168
0.27020	0.07072
0.25064	0.06963
0.23161	0.06840
0.21327	0.06706
0.19577	0.06563
0.17922	0.06411
0.16373	0.06252
0.14935	0.06090
0.13610	0.05925
0.12396	0.05761
0.11288	0.05596
0.10278	0.05432
0.09356	0.05270
0.08515	0.05109
0.07744	0.04951
0.07038	0.04794
0.06387	0.04639
0.05787	0.04484
0.05232	0.04330
0.04717	0.04175
0.04238	0.04018
0.03792	0.03858
0.03375	0.03696
0.02987	0.03529
0.02624	0.03357
0.02285	0.03180
0.01970	0.02996
0.01677	0.02806
0.01406	0.02608
0.01158	0.02402
0.00933	0.02188
0.00732	0.01965
0.00555	0.01733
0.00403	0.01494
0.00276	0.01249
0.00174	0.01000
0.00096	0.00749
0.00042	0.00497
0.00011	0.00247
0.00003	0.00124
0.00000	0.00000
0.00010	-0.00238
0.00038	-0.00475
0.00087	-0.00715
0.00158	-0.00954
0.00250	-0.01192
0.00365	-0.01427
0.00503	-0.01657
0.00663	-0.01880
0.00847	-0.02095
0.01052	-0.02302
0.01279	-0.02500
0.01527	-0.02690
0.01795	-0.02873
0.02084	-0.03048
0.02392	-0.03217
0.02722	-0.03381
0.03074	-0.03540
0.03450	-0.03693
0.03851	-0.03841
0.04279	-0.03987
0.04736	-0.04129
0.05227	-0.04267
0.05754	-0.04405
0.06321	-0.04542
0.06933	-0.04678
0.07594	-0.04814
0.08312	-0.04951
0.09092	-0.05088
0.09942	-0.05226
0.10870	-0.05365
0.11883	-0.05504
0.12987	-0.05642
0.14189	-0.05778
0.15492	-0.05912
0.16895	-0.06041
0.18394	-0.06163
0.19983	-0.06276
0.21653	-0.06377
0.23391	-0.06467
0.25186	-0.06542
0.27024	-0.06603
0.28897	-0.06648
0.30793	-0.06678
0.32704	-0.06691
0.34622	-0.06688
0.36539	-0.06667
0.38454	-0.06628
0.40361	-0.06572
0.42253	-0.06498
0.44129	-0.06402
0.45987	-0.06284
0.47829	-0.06142
0.49662	-0.05972
0.51489	-0.05775
0.53315	-0.05549
0.55147	-0.05294
0.56990	-0.05010
0.58853	-0.04696
0.60736	-0.04358
0.62641	-0.03996
0.64567	-0.03612
0.66513	-0.03209
0.68475	-0.02792
0.70442	-0.02367
0.72394	-0.01946
0.74311	-0.01540
0.76181	-0.01153
0.77992	-0.00793
0.79741	-0.00464
0.81426	-0.00172
0.83052	0.00079
0.84624	0.00288
0.86150	0.00453
0.87633	0.00576
0.89078	0.00652
0.90496	0.00669
0.91907	0.00638
0.93311	0.00562
0.94711	0.00437
0.96118	0.00259
0.97540	0.00026
0.98991	-0.00272
1.00000	-0.00515

NASA-SC-0614_eta-0.09_-1.0	
1.00000	0.00515
0.98939	0.00768
0.97275	0.01151
0.95536	0.01534
0.93735	0.01911
0.91885	0.02289
0.90015	0.02662
0.88121	0.03029
0.86200	0.03401
0.84246	0.03760
0.82268	0.04110
0.80276	0.04446
0.78275	0.04767
0.76269	0.05072
0.74261	0.05359
0.72250	0.05630
0.70244	0.05883
0.68241	0.06117
0.66241	0.06330
0.64242	0.06522
0.62242	0.06692
0.60232	0.06841
0.58213	0.06971
0.56182	0.07083
0.54141	0.07178
0.52088	0.07256
0.50023	0.07318
0.47949	0.07366
0.45865	0.07399
0.43775	0.07421
0.41690	0.07431
0.39609	0.07426
0.37535	0.07408
0.35473	0.07376
0.33426	0.07330
0.31398	0.07269
0.29398	0.07194
0.27428	0.07102
0.25494	0.06996
0.23612	0.06879
0.21792	0.06749
0.20050	0.06611
0.18399	0.06464
0.16848	0.06310
0.15403	0.06151
0.14067	0.05990
0.12840	0.05829
0.11717	0.05667
0.10690	0.05507
0.09753	0.05348
0.08896	0.05189
0.08111	0.05032
0.07389	0.04878
0.06726	0.04726
0.06113	0.04574
0.05546	0.04423
0.05020	0.04271
0.04530	0.04119
0.04074	0.03965
0.03648	0.03808
0.03250	0.03648
0.02878	0.03482
0.02529	0.03312
0.02204	0.03137
0.01901	0.02956
0.01619	0.02767
0.01358	0.02572
0.01119	0.02368
0.00902	0.02156
0.00707	0.01936
0.00536	0.01708
0.00390	0.01472
0.00268	0.01231
0.00169	0.00986
0.00094	0.00738
0.00041	0.00490
0.00010	0.00244
0.00003	0.00122
0.00000	0.00000
0.00010	-0.00241
0.00040	-0.00481
0.00089	-0.00724
0.00162	-0.00967
0.00256	-0.01207
0.00374	-0.01444
0.00514	-0.01676
0.00678	-0.01900
0.00865	-0.02117
0.01074	-0.02325
0.01306	-0.02524
0.01558	-0.02714
0.01830	-0.02898
0.02122	-0.03074
0.02436	-0.03243
0.02771	-0.03407
0.03128	-0.03565
0.03509	-0.03719
0.03916	-0.03869
0.04351	-0.04014
0.04816	-0.04156
0.05315	-0.04296
0.05851	-0.04434
0.06428	-0.04571
0.07052	-0.04708
0.07727	-0.04845
0.08459	-0.04983
0.09256	-0.05121
0.10126	-0.05260
0.11076	-0.05401
0.12112	-0.05540
0.13244	-0.05679
0.14476	-0.05816
0.15811	-0.05950
0.17246	-0.06079
0.18780	-0.06200
0.20403	-0.06311
0.22106	-0.06410
0.23876	-0.06497
0.25701	-0.06570
0.27568	-0.06627
0.29468	-0.06668
0.31389	-0.06693
0.33321	-0.06703
0.35258	-0.06694
0.37195	-0.06667
0.39127	-0.06622
0.41049	-0.06559
0.42953	-0.06478
0.44839	-0.06374
0.46707	-0.06247
0.48562	-0.06093
0.50408	-0.05912
0.52249	-0.05702
0.54093	-0.05464
0.55945	-0.05195
0.57813	-0.04897
0.59701	-0.04570
0.61614	-0.04218
0.63550	-0.03843
0.65507	-0.03446
0.67487	-0.03030
0.69484	-0.02601
0.71479	-0.02171
0.73446	-0.01749
0.75370	-0.01346
0.77238	-0.00966
0.79046	-0.00617
0.80791	-0.00301
0.82474	-0.00026
0.84105	0.00206
0.85691	0.00395
0.87240	0.00537
0.88772	0.00634
0.90284	0.00700
0.91760	0.00726
0.93211	0.00701
0.94649	0.00626
0.96084	0.00496
0.97531	0.00312
0.99002	0.00063
1.00000	-0.00146

NASA-SC-0614_eta-0.09_2.5	
1.00000	-0.00136
0.98959	0.00182
0.97378	0.00649
0.95799	0.01099
0.94248	0.01530
0.92709	0.01905
0.91137	0.02293
0.89520	0.02679
0.87872	0.03032
0.86136	0.03359
0.84323	0.03697
0.82453	0.04029
0.80535	0.04356
0.78588	0.04673
0.76618	0.04976
0.74633	0.05266
0.72640	0.05539
0.70642	0.05796
0.68644	0.06035
0.66647	0.06253
0.64650	0.06451
0.62651	0.06627
0.60644	0.06782
0.58627	0.06917
0.56599	0.07035
0.54562	0.07135
0.52513	0.07217
0.50453	0.07284
0.48381	0.07334
0.46301	0.07372
0.44215	0.07397
0.42130	0.07410
0.40049	0.07409
0.37976	0.07394
0.35911	0.07366
0.33860	0.07324
0.31829	0.07267
0.29821	0.07195
0.27843	0.07108
0.25900	0.07005
0.24001	0.06889
0.22163	0.06764
0.20399	0.06626
0.18722	0.06481
0.17144	0.06328
0.15670	0.06170
0.14305	0.06009
0.13050	0.05846
0.11900	0.05684
0.10850	0.05522
0.09891	0.05361
0.09015	0.05203
0.08213	0.05045
0.07478	0.04889
0.06801	0.04735
0.06177	0.04583
0.05601	0.04431
0.05066	0.04278
0.04570	0.04124
0.04107	0.03969
0.03675	0.03812
0.03272	0.03651
0.02896	0.03485
0.02544	0.03314
0.02215	0.03139
0.01909	0.02956
0.01625	0.02767
0.01362	0.02571
0.01121	0.02367
0.00902	0.02155
0.00707	0.01934
0.00536	0.01705
0.00389	0.01469
0.00266	0.01228
0.00168	0.00983
0.00093	0.00736
0.00040	0.00489
0.00010	0.00243
0.00003	0.00122
0.00000	0.00000
0.00010	-0.00244
0.00040	-0.00487
0.00092	-0.00733
0.00166	-0.00979
0.00264	-0.01223
0.00386	-0.01463
0.00532	-0.01698
0.00701	-0.01927
0.00896	-0.02145
0.01113	-0.02356
0.01353	-0.02558
0.01614	-0.02751
0.01897	-0.02935
0.02202	-0.03113
0.02529	-0.03285
0.02878	-0.03451
0.03252	-0.03611
0.03651	-0.03767
0.04078	-0.03917
0.04536	-0.04065
0.05027	-0.04209
0.05555	-0.04352
0.06124	-0.04492
0.06738	-0.04632
0.07404	-0.04772
0.08127	-0.04913
0.08915	-0.05055
0.09775	-0.05196
0.10716	-0.05339
0.11745	-0.05482
0.12871	-0.05624
0.14099	-0.05764
0.15434	-0.05902
0.16874	-0.06035
0.18415	-0.06160
0.20052	-0.06275
0.21774	-0.06378
0.23567	-0.06469
0.25417	-0.06545
0.27312	-0.06605
0.29241	-0.06648
0.31192	-0.06675
0.33158	-0.06685
0.35128	-0.06677
0.37098	-0.06650
0.39062	-0.06604
0.41018	-0.06539
0.42955	-0.06455
0.44876	-0.06348
0.46779	-0.06216
0.48668	-0.06056
0.50549	-0.05866
0.52427	-0.05649
0.54307	-0.05400
0.56196	-0.05120
0.58102	-0.04809
0.60030	-0.04471
0.61981	-0.04106
0.63953	-0.03719
0.65945	-0.03310
0.67957	-0.02883
0.69978	-0.02449
0.71985	-0.02016
0.73957	-0.01595
0.75877	-0.01197
0.77735	-0.00826
0.79525	-0.00488
0.81246	-0.00188
0.82899	0.00069
0.84491	0.00282
0.86024	0.00451
0.87506	0.00566
0.88951	0.00624
0.90372	0.00627
0.91781	0.00577
0.93188	0.00470
0.94602	0.00311
0.96027	0.00098
0.97473	-0.00176
0.98952	-0.00517
1.00000	-0.00794

NASA-SC-0614_eta-0.09_2.0	
1.00000	-0.00042
0.98944	0.00270
0.97322	0.00734
0.95676	0.01187
0.94035	0.01624
0.92379	0.02012
0.90684	0.02419
0.88964	0.02815
0.87189	0.03168
0.85331	0.03517
0.83424	0.03865
0.81476	0.04204
0.79501	0.04533
0.77509	0.04847
0.75503	0.05147
0.73491	0.05430
0.71474	0.05696
0.69458	0.05945
0.67444	0.06173
0.65431	0.06380
0.63418	0.06567
0.61400	0.06731
0.59374	0.06874
0.57336	0.06998
0.55286	0.07105
0.53227	0.07194
0.51157	0.07266
0.49075	0.07322
0.46983	0.07364
0.44884	0.07393
0.42784	0.07410
0.40688	0.07413
0.38596	0.07402
0.36514	0.07378
0.34446	0.07339
0.32393	0.07286
0.30365	0.07218
0.28364	0.07134
0.26397	0.07034
0.24472	0.06922
0.22606	0.06797
0.20811	0.06662
0.19101	0.06517
0.17488	0.06365
0.15982	0.06206
0.14584	0.06044
0.13297	0.05881
0.12119	0.05717
0.11043	0.05555
0.10062	0.05392
0.09165	0.05232
0.08346	0.05073
0.07595	0.04916
0.06905	0.04761
0.06269	0.04607
0.05682	0.04454
0.05138	0.04301
0.04633	0.04147
0.04163	0.03990
0.03725	0.03831
0.03316	0.03670
0.02934	0.03503
0.02578	0.03333
0.02245	0.03156
0.01935	0.02973
0.01646	0.02784
0.01380	0.02587
0.01137	0.02382
0.00915	0.02168
0.00718	0.01946
0.00544	0.01716
0.00395	0.01479
0.00270	0.01236
0.00170	0.00990
0.00094	0.00741
0.00041	0.00492
0.00011	0.00245
0.00003	0.00123
0.00000	0.00000
0.00010	-0.00241
0.00039	-0.00480
0.00089	-0.00723
0.00161	-0.00966
0.00257	-0.01207
0.00375	-0.01445
0.00517	-0.01677
0.00682	-0.01902
0.00871	-0.02120
0.01082	-0.02329
0.01315	-0.02529
0.01570	-0.02720
0.01846	-0.02904
0.02142	-0.03081
0.02460	-0.03252
0.02800	-0.03416
0.03163	-0.03575
0.03551	-0.03729
0.03965	-0.03880
0.04408	-0.04027
0.04883	-0.04170
0.05393	-0.04310
0.05941	-0.04449
0.06532	-0.04588
0.07171	-0.04726
0.07864	-0.04864
0.08618	-0.05003
0.09438	-0.05144
0.10334	-0.05284
0.11313	-0.05425
0.12383	-0.05565
0.13551	-0.05705
0.14821	-0.05842
0.16194	-0.05976
0.17669	-0.06103
0.19239	-0.06222
0.20897	-0.06330
0.22632	-0.06425
0.24429	-0.06508
0.26276	-0.06576
0.28163	-0.06628
0.30077	-0.06664
0.32010	-0.06684
0.33951	-0.06687
0.35895	-0.06671
0.37838	-0.06637
0.39774	-0.06585
0.41698	-0.06515
0.43605	-0.06425
0.45492	-0.06312
0.47364	-0.06173
0.49225	-0.06006
0.51081	-0.05812
0.52933	-0.05590
0.54790	-0.05336
0.56657	-0.05053
0.58542	-0.04740
0.60449	-0.04400
0.62378	-0.04036
0.64329	-0.03649
0.66301	-0.03242
0.68290	-0.02819
0.70288	-0.02388
0.72270	-0.01961
0.74214	-0.01548
0.76107	-0.01156
0.77938	-0.00792
0.79702	-0.00460
0.81399	-0.00167
0.83033	0.00084
0.84608	0.00293
0.86129	0.00458
0.87601	0.00572
0.89039	0.00632
0.90454	0.00640
0.91857	0.00595
0.93256	0.00498
0.94659	0.00350
0.96072	0.00149
0.97505	-0.00110
0.98969	-0.00437
1.00000	-0.00701

NASA-SC-0614_eta-0.09_-2.0	
1.00000	0.00698
0.98931	0.00935
0.97261	0.01288
0.95530	0.01637
0.93748	0.01979
0.91935	0.02329
0.90122	0.02668
0.88312	0.03006
0.86471	0.03366
0.84574	0.03717
0.82634	0.04061
0.80667	0.04396
0.78683	0.04717
0.76686	0.05023
0.74682	0.05314
0.72674	0.05587
0.70666	0.05844
0.68660	0.06081
0.66657	0.06298
0.64654	0.06494
0.62648	0.06668
0.60636	0.06822
0.58614	0.06955
0.56579	0.07071
0.54536	0.07169
0.52481	0.07250
0.50413	0.07315
0.48336	0.07365
0.46249	0.07401
0.44157	0.07425
0.42066	0.07436
0.39980	0.07434
0.37902	0.07418
0.35833	0.07388
0.33779	0.07344
0.31743	0.07285
0.29732	0.07212
0.27751	0.07123
0.25806	0.07019
0.23908	0.06902
0.22072	0.06774
0.20311	0.06636
0.18639	0.06490
0.17066	0.06336
0.15599	0.06177
0.14241	0.06016
0.12994	0.05853
0.11852	0.05691
0.10808	0.05529
0.09856	0.05368
0.08985	0.05209
0.08188	0.05052
0.07457	0.04896
0.06784	0.04743
0.06164	0.04590
0.05590	0.04438
0.05057	0.04285
0.04563	0.04132
0.04102	0.03976
0.03672	0.03819
0.03270	0.03658
0.02894	0.03492
0.02543	0.03321
0.02215	0.03145
0.01910	0.02963
0.01626	0.02774
0.01364	0.02578
0.01123	0.02373
0.00904	0.02161
0.00710	0.01939
0.00538	0.01710
0.00391	0.01474
0.00268	0.01232
0.00169	0.00987
0.00094	0.00739
0.00041	0.00491
0.00010	0.00244
0.00002	0.00122
0.00000	0.00000
0.00010	-0.00240
0.00039	-0.00479
0.00089	-0.00721
0.00160	-0.00964
0.00254	-0.01204
0.00371	-0.01440
0.00511	-0.01672
0.00675	-0.01896
0.00861	-0.02113
0.01069	-0.02321
0.01300	-0.02520
0.01551	-0.02712
0.01822	-0.02895
0.02115	-0.03071
0.02428	-0.03241
0.02763	-0.03405
0.03120	-0.03564
0.03501	-0.03718
0.03908	-0.03867
0.04343	-0.04013
0.04808	-0.04156
0.05307	-0.04296
0.05843	-0.04434
0.06421	-0.04572
0.07045	-0.04709
0.07720	-0.04847
0.08453	-0.04985
0.09251	-0.05124
0.10122	-0.05263
0.11072	-0.05403
0.12110	-0.05543
0.13243	-0.05682
0.14476	-0.05819
0.15811	-0.05954
0.17247	-0.06083
0.18780	-0.06203
0.20402	-0.06315
0.22105	-0.06414
0.23874	-0.06501
0.25698	-0.06574
0.27562	-0.06632
0.29458	-0.06673
0.31375	-0.06699
0.33307	-0.06708
0.35241	-0.06701
0.37175	-0.06674
0.39104	-0.06630
0.41023	-0.06567
0.42927	-0.06486
0.44811	-0.06384
0.46680	-0.06257
0.48532	-0.06105
0.50378	-0.05924
0.52218	-0.05717
0.54061	-0.05479
0.55910	-0.05213
0.57774	-0.04915
0.59660	-0.04591
0.61567	-0.04241
0.63497	-0.03867
0.65449	-0.03472
0.67422	-0.03058
0.69408	-0.02632
0.71393	-0.02203
0.73356	-0.01783
0.75278	-0.01378
0.77148	-0.00998
0.78959	-0.00645
0.80707	-0.00327
0.82396	-0.00049
0.84031	0.00187
0.85622	0.00380
0.87173	0.00526
0.88713	0.00626
0.90239	0.00712
0.91723	0.00766
0.93183	0.00768
0.94629	0.00717
0.96073	0.00613
0.97527	0.00453
0.99008	0.00230
1.00000	0.00038

NASA-SC-0614_eta-0.09_3.5	
1.00000	-0.00324
0.98976	0.00008
0.97393	0.00506
0.95770	0.01000
0.94130	0.01482
0.92488	0.01932
0.90821	0.02344
0.89151	0.02748
0.87470	0.03096
0.85711	0.03426
0.83893	0.03762
0.82025	0.04091
0.80123	0.04413
0.78196	0.04723
0.76253	0.05020
0.74299	0.05302
0.72337	0.05569
0.70373	0.05819
0.68410	0.06051
0.66448	0.06265
0.64488	0.06458
0.62523	0.06630
0.60554	0.06782
0.58574	0.06914
0.56584	0.07029
0.54583	0.07127
0.52572	0.07209
0.50550	0.07275
0.48518	0.07326
0.46476	0.07364
0.44429	0.07390
0.42382	0.07404
0.40338	0.07405
0.38302	0.07393
0.36273	0.07367
0.34257	0.07328
0.32259	0.07276
0.30281	0.07209
0.28332	0.07127
0.26415	0.07030
0.24537	0.06920
0.22715	0.06800
0.20959	0.06668
0.19283	0.06529
0.17699	0.06381
0.16214	0.06227
0.14832	0.06070
0.13556	0.05911
0.12385	0.05752
0.11312	0.05593
0.10331	0.05435
0.09433	0.05278
0.08611	0.05122
0.07856	0.04969
0.07162	0.04817
0.06522	0.04667
0.05930	0.04517
0.05382	0.04368
0.04872	0.04218
0.04397	0.04067
0.03954	0.03913
0.03540	0.03758
0.03153	0.03599
0.02791	0.03435
0.02452	0.03266
0.02135	0.03092
0.01840	0.02911
0.01566	0.02724
0.01312	0.02530
0.01080	0.02329
0.00869	0.02119
0.00681	0.01900
0.00516	0.01675
0.00375	0.01443
0.00257	0.01205
0.00162	0.00965
0.00090	0.00722
0.00039	0.00479
0.00010	0.00238
0.00003	0.00119
0.00000	0.00000
0.00011	-0.00248
0.00041	-0.00495
0.00095	-0.00745
0.00172	-0.00994
0.00273	-0.01242
0.00398	-0.01486
0.00549	-0.01723
0.00725	-0.01953
0.00925	-0.02175
0.01149	-0.02387
0.01397	-0.02590
0.01666	-0.02785
0.01958	-0.02971
0.02272	-0.03150
0.02609	-0.03323
0.02970	-0.03490
0.03356	-0.03651
0.03769	-0.03807
0.04211	-0.03960
0.04686	-0.04108
0.05196	-0.04254
0.05745	-0.04398
0.06339	-0.04540
0.06981	-0.04683
0.07679	-0.04824
0.08438	-0.04968
0.09268	-0.05111
0.10175	-0.05256
0.11169	-0.05401
0.12259	-0.05545
0.13451	-0.05689
0.14751	-0.05830
0.16160	-0.05968
0.17677	-0.06099
0.19295	-0.06221
0.21006	-0.06331
0.22796	-0.06429
0.24651	-0.06512
0.26560	-0.06579
0.28507	-0.06629
0.30482	-0.06662
0.32474	-0.06679
0.34473	-0.06677
0.36473	-0.06655
0.38471	-0.06614
0.40459	-0.06555
0.42433	-0.06474
0.44387	-0.06372
0.46323	-0.06243
0.48244	-0.06087
0.50155	-0.05901
0.52063	-0.05685
0.53971	-0.05439
0.55887	-0.05160
0.57819	-0.04848
0.59774	-0.04507
0.61750	-0.04140
0.63750	-0.03748
0.65771	-0.03335
0.67811	-0.02903
0.69859	-0.02462
0.71894	-0.02023
0.73893	-0.01597
0.75838	-0.01194
0.77720	-0.00818
0.79528	-0.00477
0.81263	-0.00176
0.82927	0.00081
0.84525	0.00294
0.86060	0.00454
0.87540	0.00557
0.88977	0.00605
0.90383	0.00597
0.91772	0.00531
0.93163	0.00405
0.94569	0.00223
0.95993	-0.00015
0.97443	-0.00312
0.98932	-0.00683
1.00000	-0.00981

NASA-SC-0614_eta-0.09_3.0	
1.00000	-0.00230
0.98943	0.00103
0.97319	0.00597
0.95680	0.01080
0.94048	0.01543
0.92443	0.01967
0.90846	0.02346
0.89254	0.02729
0.87637	0.03072
0.85923	0.03392
0.84127	0.03726
0.82259	0.04056
0.80338	0.04383
0.78377	0.04701
0.76392	0.05005
0.74385	0.05295
0.72368	0.05570
0.70346	0.05828
0.68322	0.06066
0.66298	0.06285
0.64274	0.06481
0.62245	0.06657
0.60209	0.06810
0.58162	0.06943
0.56102	0.07057
0.54033	0.07155
0.51953	0.07234
0.49859	0.07297
0.47757	0.07345
0.45645	0.07378
0.43528	0.07400
0.41415	0.07409
0.39307	0.07403
0.37206	0.07383
0.35118	0.07349
0.33044	0.07300
0.30993	0.07237
0.28968	0.07157
0.26975	0.07062
0.25024	0.06952
0.23126	0.06829
0.21295	0.06696
0.19548	0.06553
0.17897	0.06402
0.16351	0.06243
0.14915	0.06081
0.13592	0.05917
0.12380	0.05752
0.11273	0.05588
0.10264	0.05425
0.09344	0.05263
0.08503	0.05102
0.07734	0.04944
0.07027	0.04787
0.06378	0.04632
0.05778	0.04477
0.05223	0.04323
0.04708	0.04168
0.04230	0.04011
0.03784	0.03852
0.03368	0.03690
0.02980	0.03523
0.02618	0.03351
0.02279	0.03174
0.01965	0.02990
0.01672	0.02800
0.01402	0.02602
0.01154	0.02397
0.00930	0.02182
0.00729	0.01959
0.00552	0.01728
0.00401	0.01489
0.00275	0.01245
0.00173	0.00997
0.00096	0.00746
0.00042	0.00496
0.00011	0.00246
0.00003	0.00123
0.00000	0.00000
0.00010	-0.00242
0.00039	-0.00481
0.00090	-0.00725
0.00162	-0.00968
0.00258	-0.01210
0.00377	-0.01448
0.00519	-0.01681
0.00686	-0.01906
0.00876	-0.02124
0.01088	-0.02333
0.01323	-0.02534
0.01579	-0.02725
0.01856	-0.02909
0.02155	-0.03086
0.02474	-0.03257
0.02816	-0.03422
0.03181	-0.03581
0.03571	-0.03736
0.03987	-0.03886
0.04433	-0.04032
0.04911	-0.04176
0.05425	-0.04316
0.05977	-0.04455
0.06572	-0.04594
0.07217	-0.04733
0.07915	-0.04872
0.08675	-0.05011
0.09504	-0.05151
0.10408	-0.05292
0.11397	-0.05433
0.12478	-0.05574
0.13657	-0.05714
0.14939	-0.05851
0.16326	-0.05985
0.17813	-0.06112
0.19396	-0.06229
0.21067	-0.06336
0.22812	-0.06431
0.24619	-0.06512
0.26476	-0.06579
0.28369	-0.06628
0.30292	-0.06662
0.32231	-0.06680
0.34177	-0.06681
0.36126	-0.06663
0.38073	-0.06626
0.40012	-0.06572
0.41938	-0.06499
0.43847	-0.06405
0.45738	-0.06288
0.47612	-0.06145
0.49476	-0.05974
0.51335	-0.05775
0.53192	-0.05547
0.55054	-0.05288
0.56929	-0.04999
0.58821	-0.04681
0.60736	-0.04336
0.62672	-0.03967
0.64629	-0.03576
0.66607	-0.03165
0.68600	-0.02740
0.70594	-0.02309
0.72569	-0.01885
0.74504	-0.01475
0.76384	-0.01088
0.78200	-0.00731
0.79947	-0.00406
0.81625	-0.00121
0.83238	0.00122
0.84789	0.00321
0.86282	0.00477
0.87725	0.00578
0.89134	0.00621
0.90523	0.00611
0.91903	0.00546
0.93285	0.00426
0.94675	0.00254
0.96078	0.00030
0.97502	-0.00254
0.98961	-0.00605
1.00000	-0.00888

NASA-SC-0614_eta-0.09_4.0	
1.00000	-0.00419
0.98980	-0.00077
0.97403	0.00433
0.95790	0.00940
0.94162	0.01434
0.92537	0.01894
0.90885	0.02310
0.89231	0.02720
0.87575	0.03071
0.85836	0.03396
0.84032	0.03730
0.82176	0.04059
0.80280	0.04381
0.78356	0.04692
0.76414	0.04991
0.74459	0.05274
0.72495	0.05543
0.70531	0.05795
0.68565	0.06029
0.66600	0.06245
0.64636	0.06440
0.62670	0.06614
0.60698	0.06767
0.58714	0.06901
0.56720	0.07019
0.54717	0.07118
0.52703	0.07201
0.50679	0.07269
0.48643	0.07321
0.46597	0.07360
0.44547	0.07386
0.42495	0.07401
0.40448	0.07403
0.38405	0.07391
0.36373	0.07367
0.34352	0.07329
0.32349	0.07277
0.30367	0.07210
0.28412	0.07129
0.26490	0.07033
0.24608	0.06923
0.22781	0.06803
0.21020	0.06672
0.19339	0.06532
0.17749	0.06384
0.16259	0.06231
0.14874	0.06073
0.13594	0.05914
0.12419	0.05756
0.11343	0.05597
0.10359	0.05438
0.09458	0.05281
0.08634	0.05126
0.07877	0.04972
0.07181	0.04820
0.06540	0.04670
0.05947	0.04520
0.05397	0.04371
0.04886	0.04221
0.04410	0.04070
0.03966	0.03917
0.03551	0.03761
0.03163	0.03602
0.02800	0.03439
0.02461	0.03270
0.02143	0.03095
0.01847	0.02915
0.01572	0.02728
0.01318	0.02534
0.01085	0.02332
0.00873	0.02122
0.00685	0.01904
0.00519	0.01678
0.00376	0.01446
0.00258	0.01208
0.00162	0.00967
0.00090	0.00724
0.00039	0.00481
0.00010	0.00239
0.00003	0.00120
0.00000	0.00000
0.00011	-0.00249
0.00042	-0.00496
0.00096	-0.00747
0.00173	-0.00997
0.00275	-0.01245
0.00400	-0.01490
0.00552	-0.01728
0.00729	-0.01958
0.00930	-0.02179
0.01154	-0.02392
0.01403	-0.02595
0.01674	-0.02789
0.01966	-0.02976
0.02281	-0.03154
0.02619	-0.03327
0.02980	-0.03494
0.03368	-0.03655
0.03782	-0.03811
0.04226	-0.03963
0.04702	-0.04112
0.05213	-0.04258
0.05764	-0.04401
0.06359	-0.04544
0.07004	-0.04686
0.07703	-0.04829
0.08465	-0.04972
0.09297	-0.05116
0.10208	-0.05259
0.11206	-0.05404
0.12299	-0.05550
0.13496	-0.05692
0.14801	-0.05834
0.16215	-0.05972
0.17738	-0.06103
0.19362	-0.06224
0.21078	-0.06334
0.22874	-0.06430
0.24737	-0.06513
0.26650	-0.06580
0.28602	-0.06629
0.30582	-0.06662
0.32578	-0.06678
0.34580	-0.06674
0.36585	-0.06651
0.38585	-0.06609
0.40577	-0.06547
0.42553	-0.06466
0.44509	-0.06361
0.46447	-0.06231
0.48369	-0.06072
0.50284	-0.05884
0.52192	-0.05666
0.54104	-0.05416
0.56024	-0.05133
0.57962	-0.04818
0.59923	-0.04474
0.61907	-0.04104
0.63914	-0.03710
0.65943	-0.03293
0.67991	-0.02858
0.70049	-0.02416
0.72090	-0.01976
0.74087	-0.01551
0.76029	-0.01149
0.77901	-0.00777
0.79699	-0.00441
0.81422	-0.00145
0.83073	0.00106
0.84655	0.00313
0.86173	0.00465
0.87636	0.00560
0.89056	0.00599
0.90444	0.00581
0.91818	0.00506
0.93195	0.00368
0.94590	0.00174
0.96004	-0.00075
0.97446	-0.00385
0.98929	-0.00768
1.00000	-0.01075

NASA-SC-0712_eta-0.32_0		NASA-SC-0712_eta-0.32_0.5		NASA-SC-0712_eta-0.32_-0.5		NASA-SC-0712_eta-0.32_1.5		NASA-SC-0712_eta-0.32_-1.5		NASA-SC-0712_eta-0.32_1.0	
1.00000	0.00300	1.00000	0.00139	1.00000	0.00461	1.00000	-0.00185	1.00000	0.00782	1.00000	-0.00023
0.99211	0.00514	0.99200	0.00363	0.99156	0.00682	0.99237	0.00043	0.99178	0.00982	0.99243	0.00196
0.97989	0.00836	0.97966	0.00699	0.97852	0.01012	0.98028	0.00396	0.97901	0.01282	0.98046	0.00535
0.96731	0.01152	0.96701	0.01028	0.96513	0.01333	0.96746	0.00754	0.96582	0.01575	0.96775	0.00878
0.95448	0.01459	0.95420	0.01346	0.95158	0.01643	0.95389	0.01115	0.95232	0.01859	0.95427	0.01225
0.94161	0.01752	0.94146	0.01648	0.93806	0.01934	0.93955	0.01480	0.93872	0.02130	0.94001	0.01574
0.92879	0.02030	0.92889	0.01931	0.92468	0.02209	0.92453	0.01845	0.92513	0.02385	0.92502	0.01926
0.91629	0.02296	0.91672	0.02202	0.91177	0.02470	0.90888	0.02208	0.91183	0.02629	0.90935	0.02276
0.90448	0.02529	0.90524	0.02440	0.89944	0.02688	0.89288	0.02565	0.89909	0.02836	0.89318	0.02622
0.89287	0.02724	0.89398	0.02636	0.88708	0.02889	0.87651	0.02900	0.88633	0.03034	0.87651	0.02954
0.88090	0.02938	0.88239	0.02845	0.87419	0.03128	0.85904	0.03235	0.87299	0.03269	0.85903	0.03283
0.86816	0.03183	0.87012	0.03088	0.86025	0.03379	0.84109	0.03569	0.85852	0.03510	0.84109	0.03607
0.85423	0.03434	0.85673	0.03340	0.84491	0.03637	0.82298	0.03888	0.84268	0.03758	0.82290	0.03919
0.83899	0.03696	0.84202	0.03602	0.82843	0.03905	0.80474	0.04195	0.82571	0.04011	0.80459	0.04217
0.82270	0.03964	0.82623	0.03875	0.81094	0.04173	0.78686	0.04475	0.80767	0.04264	0.78644	0.04492
0.80546	0.04234	0.80955	0.04148	0.79253	0.04441	0.76884	0.04725	0.78849	0.04521	0.76814	0.04743
0.78754	0.04498	0.79221	0.04417	0.77346	0.04701	0.75017	0.04960	0.76868	0.04783	0.74936	0.04978
0.76893	0.04751	0.77433	0.04670	0.75390	0.04950	0.73107	0.05183	0.74868	0.05032	0.73027	0.05200
0.74976	0.04992	0.75566	0.04910	0.73400	0.05184	0.71161	0.05391	0.72847	0.05263	0.71087	0.05407
0.73002	0.05219	0.73626	0.05141	0.71374	0.05401	0.69178	0.05584	0.70814	0.05475	0.69126	0.05597
0.70988	0.05433	0.71632	0.05358	0.69323	0.05601	0.67170	0.05761	0.68762	0.05669	0.67136	0.05770
0.68940	0.05629	0.69592	0.05561	0.67246	0.05783	0.65131	0.05920	0.66690	0.05843	0.65119	0.05926
0.66861	0.05807	0.67516	0.05746	0.65147	0.05945	0.63054	0.06061	0.64594	0.05998	0.63067	0.06066
0.64744	0.05967	0.65401	0.05913	0.63013	0.06089	0.60933	0.06186	0.62464	0.06136	0.60980	0.06190
0.62584	0.06109	0.63241	0.06062	0.60845	0.06215	0.58768	0.06296	0.60297	0.06257	0.58850	0.06298
0.60380	0.06234	0.61038	0.06193	0.58637	0.06325	0.56561	0.06391	0.58095	0.06362	0.56680	0.06391
0.58127	0.06342	0.58784	0.06307	0.56392	0.06419	0.54322	0.06471	0.55857	0.06451	0.54480	0.06471
0.55830	0.06435	0.56483	0.06405	0.54123	0.06498	0.52056	0.06536	0.53595	0.06525	0.52253	0.06535
0.53502	0.06511	0.54149	0.06487	0.51828	0.06561	0.49768	0.06585	0.51310	0.06584	0.50006	0.06585
0.51145	0.06572	0.51784	0.06552	0.49525	0.06608	0.47466	0.06619	0.49015	0.06626	0.47744	0.06620
0.48778	0.06615	0.49397	0.06600	0.47204	0.06639	0.45154	0.06636	0.46702	0.06653	0.45474	0.06638
0.46390	0.06641	0.46996	0.06632	0.44876	0.06654	0.42829	0.06638	0.44385	0.06664	0.43190	0.06642
0.43987	0.06651	0.44581	0.06646	0.42542	0.06653	0.40508	0.06625	0.42061	0.06660	0.40908	0.06632
0.41587	0.06644	0.42165	0.06644	0.40213	0.06638	0.38198	0.06597	0.39745	0.06641	0.38635	0.06607
0.39187	0.06622	0.39748	0.06625	0.37888	0.06606	0.35905	0.06553	0.37435	0.06606	0.36378	0.06567
0.36807	0.06583	0.37346	0.06590	0.35583	0.06561	0.33639	0.06496	0.35146	0.06557	0.34144	0.06514
0.34450	0.06528	0.34965	0.06538	0.33308	0.06500	0.31419	0.06425	0.32889	0.06495	0.31952	0.06447
0.32137	0.06460	0.32625	0.06472	0.31071	0.06426	0.29257	0.06341	0.30681	0.06418	0.29813	0.06368
0.29883	0.06377	0.30339	0.06392	0.28893	0.06338	0.27169	0.06245	0.28526	0.06328	0.27736	0.06275
0.27702	0.06279	0.28123	0.06296	0.26778	0.06236	0.25158	0.06136	0.26445	0.06226	0.25735	0.06172
0.25599	0.06170	0.25987	0.06189	0.24741	0.06123	0.23245	0.06019	0.24445	0.06112	0.23822	0.06058
0.23598	0.06050	0.23951	0.06069	0.22800	0.06001	0.21436	0.05893	0.22540	0.05989	0.22006	0.05938
0.21709	0.05921	0.22021	0.05941	0.20967	0.05870	0.19743	0.05762	0.20745	0.05858	0.20305	0.05811
0.19944	0.05787	0.20214	0.05805	0.19253	0.05732	0.18172	0.05627	0.19066	0.05722	0.18715	0.05678
0.18304	0.05646	0.18539	0.05665	0.17660	0.05590	0.16717	0.05489	0.17512	0.05582	0.17240	0.05543
0.16792	0.05505	0.16994	0.05522	0.16190	0.05446	0.15379	0.05352	0.16078	0.05440	0.15881	0.05407
0.15408	0.05362	0.15575	0.05377	0.14843	0.05302	0.14156	0.05215	0.14762	0.05297	0.14632	0.05272
0.14142	0.05219	0.14280	0.05233	0.13614	0.05159	0.13034	0.05079	0.13558	0.05156	0.13487	0.05137
0.12985	0.05079	0.13099	0.05091	0.12492	0.05018	0.12008	0.04945	0.12458	0.05018	0.12437	0.05004
0.11929	0.04941	0.12022	0.04951	0.11468	0.04880	0.11067	0.04815	0.11454	0.04883	0.11474	0.04874
0.10965	0.04806	0.11040	0.04815	0.10535	0.04745	0.10205	0.04688	0.10538	0.04750	0.10591	0.04748
0.10084	0.04674	0.10143	0.04682	0.09681	0.04613	0.09412	0.04563	0.09698	0.04621	0.09779	0.04624
0.09274	0.04546	0.09321	0.04552	0.08898	0.04485	0.08680	0.04440	0.08927	0.04494	0.09031	0.04501
0.08530	0.04419	0.08565	0.04423	0.08178	0.04358	0.08003	0.04319	0.08216	0.04369	0.08337	0.04381
0.07842	0.04294	0.07867	0.04298	0.07513	0.04234	0.07373	0.04199	0.07558	0.04246	0.07694	0.04263
0.07203	0.04171	0.07221	0.04173	0.06896	0.04111	0.06786	0.04081	0.06947	0.04124	0.07095	0.04146
0.06609	0.04049	0.06620	0.04049	0.06323	0.03989	0.06237	0.03963	0.06378	0.04004	0.06535	0.04030
0.06054	0.03926	0.06059	0.03925	0.05788	0.03866	0.05723	0.03844	0.05847	0.03883	0.06010	0.03913
0.05533	0.03803	0.05534	0.03801	0.05287	0.03742	0.05238	0.03724	0.05349	0.03761	0.05517	0.03795
0.05044	0.03677	0.05040	0.03674	0.04816	0.03617	0.04780	0.03602	0.04879	0.03638	0.05051	0.03676
0.04581	0.03551	0.04574	0.03546	0.04372	0.03491	0.04346	0.03478	0.04436	0.03513	0.04610	0.03555
0.04144	0.03421	0.04133	0.03416	0.03952	0.03362	0.03934	0.03352	0.04018	0.03387	0.04192	0.03433
0.03729	0.03289	0.03715	0.03283	0.03555	0.03232	0.03542	0.03222	0.03621	0.03257	0.03794	0.03308
0.03334	0.03153	0.03319	0.03146	0.03178	0.03097	0.03169	0.03089	0.03244	0.03124	0.03416	0.03179
0.02958	0.03012	0.02941	0.03004	0.02821	0.02959	0.02812	0.02951	0.02886	0.02987	0.03054	0.03048
0.02599	0.02865	0.02582	0.02857	0.02481	0.02815	0.02472	0.02807	0.02545	0.02845	0.02709	0.02910
0.02257	0.02711	0.02239	0.02701	0.02159	0.02664	0.02147	0.02655	0.02220	0.02696	0.02380	0.02766
0.01931	0.02548	0.01912	0.02536	0.01852	0.02506	0.01836	0.02493	0.01911	0.02540	0.02065	0.02614
0.01621	0.02372	0.01602	0.02359	0.01562	0.02337	0.01540	0.02320	0.01618	0.02373	0.01764	0.02454
0.01326	0.02181	0.01308	0.02167	0.01289	0.02156	0.01259	0.02131	0.01341	0.02194	0.01477	0.02280
0.01049	0.01973	0.01031	0.01958	0.01034	0.01961	0.00995	0.01926	0.01081	0.02001	0.01206	0.02093
0.00790	0.01742	0.00774	0.01726	0.00797	0.01750	0.00748	0.01699	0.00839	0.01791	0.00950	0.01888
0.00554	0.01483	0.00540	0.01467	0.00582	0.01519	0.00524	0.01444	0.00617	0.01561	0.00712	0.01662
0.00345	0.01191	0.00335	0.01174	0.00394	0.01266	0.00326	0.01157	0.00420	0.01308	0.00496	0.01410
0.00175	0.00856	0.00168	0.00840	0.00235	0.00990	0.00164	0.00830	0.00254	0.01028	0.00308	0.01126
0.00052	0.00467	0.00050	0.00456	0.00112	0.00688	0.00049	0.00452	0.00123	0.00720	0.00154	0.00805
0.00015	0.00235	0.00015	0.00229	0.00032	0.00358	0.00014	0.00227	0.00035	0.00379	0.00046	0.00436
0.00000	0.00000	0.00000	0.00000	0.00009	0.00180	0.00000	0.00000	0.00010	0.00190	0.00013	0.00219
0.00045	-0.00433	0.00042	-0.00419	0.00000	0.00000	0.00045	-0.00432	0.00000	0.00000	0.00000	0.00000
0.00172	-0.00849	0.00161	-0.00823	0.00030	-0.00347	0.00171	-0.00847	0.00033	-0.00369	0.00044	-0.00428
0.00340	-0.01181	0.00322	-0.01149	0.00111	-0.00686	0.00340	-0.01178	0.00126	-0.00728	0.00168	-0.00840
0.00546	-0.01469	0.00519	-0.01436	0.00234	-0.00987	0.00544	-0.01466	0.00259	-0.01038	0.00335	-0.01170
0.00778	-0.01723	0.00744	-0.01689	0.00392	-0.01261	0.00776	-0.01720	0.00429	-0.01318	0.00538	-0.01459
0.01034	-0.01948	0.00992	-0.01913	0.00580	-0.01511	0.01032	-0.01944	0.00630	-0.01570	0.00770	-0.01714
0.01309	-0.02150	0.01259	-0.02116	0.00793	-0.01739	0.01306	-0.02146	0.00855	-0.01798	0.01025	-0.01941
0.01599	-0.02333	0.01543	-0.02299	0.01029	-0.01945	0.01597	-0.02329	0.01102	-0.02004	0.01301	-0.02142
0.01906	-0.02500	0.01843	-0.02467	0.01284	-0.02135	0.01902	-0.02496	0.01368	-0.02192	0.01592	-0.02327
0.02227	-0.02656	0.02157	-0.02623	0.01557	-0.02309	0.02223	-0.02652				
0.02563	-0.02801	0.02486	-0.02768	0.01845	-0.02470	0.02559	-0.02796				
0.02915	-0.02937	0.02831	-0.02904	0.02150	-0.02621	0.02910	-0.02932				
0.03283	-0.03067	0.03192	-0.03034	0.02470	-0.02763	0.03279	-0.03062				
0.03670	-0.03191	0.03570	-0.03158	0.02807	-0.02898	0.03665	-0.03185				
0.04076	-0.03309	0.03967	-0.03277	0.03161	-0.03026	0.04070	-0.03303				
0.04503	-0.03424	0.04385	-0.03392	0.03533	-0.03149	0.04498	-0.03418				
0.04954	-0.03536	0.04826	-0.03504	0.03926	-0.03268	0.04949	-0.03530				
0.05432	-0.03644	0.05292	-0.03612	0.04340	-0.03383	0.05425	-0.03639				
0.05939	-0.03751	0.05787	-0.03718	0.04779	-0.03494	0.05932	-0.03745				
0.06479	-0.03856	0.06314	-0.03822	0.05244	-0.03605	0.06472	-0.03849				
0.07057	-0.03960	0.06876	-0.03926	0.05738	-0.03712	0.07049	-0.03953				
0.07676	-0.04064	0.07479	-0.04030	0.06266	-0.03817	0.07668	-0.04057				
0.08344	-0.04168	0.08127	-0.04134	0.06831	-0.03922	0.08335	-0.04162				
0.09065	-0.04274	0.08825	-0.04239	0.07438	-0.04026	0.09054	-0.04268				
0.09844	-0.04381	0.09581	-0.04344	0.08093	-0.04132	0.09833	-0.04374				
0.10691	-0.04488	0.10401	-0.04450	0.08801	-0.04239	0.10678	-0.04481				
0.11614	-0.04597	0.11293	-0.04558	0.09568	-0.04347	0.11599	-0.04589				
0.12618	-0.04705	0.12264	-0.04666	0.10403	-0.04455	0.12603	-0.04697				
0.13716	-0.04811	0.13323	-0.04772	0.11315	-0.04565	0.13700	-0.04803				
0.14920	-0.04916	0.14483	-0.04877	0.12309	-0.04675	0.14901	-0.04908				
0.16236	-0.05019	0.15752	-0.04981	0.13397	-0.04784	0.16213	-0.05011				
0.17669	-0.05119	0.17136	-0.05081	0.14591	-0.04891	0.17644	-0.05110				
0.19222	-0.05214	0.18637	-0.05178	0.15897	-0.04996	0.19197	-0.05205				
0.20892	-0.05301	0.20254	-0.05267	0.17322	-0.05098	0.20860	-0.05292				
0.22667	-0.05378	0.21984	-0.05347	0.18867	-0.05196	0.22634	-0.05368				
0.24545	-0.05443	0.23814	-0.05417	0.20524	-0.05286	0.24510	-0.05433				
0.26507	-0.05493	0.25730	-0.05473	0.22291	-0.05366	0.26469	-0.05484				
0.28541	-0.05529	0.27729	-0.05513	0.24153	-0.05434	0.28500	-0.05519				
0.30626	-0.05548	0.29781	-0.05539	0.26098	-0.05488	0.30582	-0.05538				
0.32745	-0.05549	0.31871	-0.05548	0.28112	-0.05526	0.32698	-0.05539				
0.34880	-0.05534	0.33986	-0.05539	0.30178	-0.05549	0.34829	-0.05524				
0.37006	-0.05502	0.36102	-0.05515	0.32277	-0.05554	0.36951	-0.05492				
0.39106	-0.05453	0.38199	-0.05473	0.34396	-0.05543	0.39049	-0.05443				
0.41167	-0.05386	0.40263	-0.05414	0.36513	-0.05516	0.41107	-0.05376				
0.43178	-0.05301	0.42285	-0.05337	0.38613	-0.05471	0.43116	-0.05291				
0.45145	-0.05196	0.44264	-0.05241	0.40682	-0.05409	0.45082	-0.05185				
0.47076	-0.05070	0.46200	-0.05125	0.42715	-0.05327	0.47013	-0.05059				
0.48975	-0.04923	0.48101	-0.04989	0.44709	-0.05226	0.48907	-0.04913				
0.50854	-0.04753	0.49979	-0.04830	0.46670	-0.05104	0.50785	-0.04742				
0.52729	-0.04559	0.51845	-0.04647	0.48600	-0.04960	0.52659	-0.04547				
0.54609	-0.04339	0.53715	-0.04439	0.50512	-0.04792	0.54541	-0.04327				
0.56514	-0.04089	0.55598	-0.04205	0.52415	-0.04600	0.56442	-0.04078				
0.58458	-0.03811	0.57511	-0.03942	0.54323	-0.04380	0.58384	-0.03799				
0.60459	-0.03500	0.59478	-0.03647	0.56249	-0.04133	0.60381	-0.03489				
0.62522	-0.03159	0.61501	-0.03322	0.58207	-0.03856	0.62444	-0.03146				
0.64661	-0.02784	0.63593	-0.02965	0.60210	-0.03549	0.64577	-0.02773				
0.66858	-0.02384	0.65756	-0.02577	0.62265	-0.03211	0.66772	-0.02372				
0.69091	-0.01962	0.67977	-0.02164	0.64387	-0.02843	0.68997	-0.01952				
0.71313	-0.01536	0.70221	-0.01736	0.66558	-0.02449	0.71206	-0.01528				
0.73419	-0.01132	0.72412	-0.01315	0.68775	-0.02032	0.73311	-0.01125				
0.75347	-0.00770	0.74461	-0.00925	0.70990	-0.01609	0.75239	-0.00761				
0.77092	-0.00452	0.76339	-0.00577	0.73140	-0.01195	0.76984	-0.00444				
0.78658	-0.00179	0.78044	-0.00274	0.75166	-0.00812	0.78563	-0.00170				
0.80085	0.00052	0.79599	-0.00016	0.77040	-0.00470	0.79986	0.00063				
0.81390	0.00263	0.81028	0.00209	0.78778	-0.00168	0.81283	0.00249				
0.82594	0.00431	0.82319	0.00387	0.80364	0.00105	0.82506	0.00387				
0.83783	0.00563	0.83563	0.00519	0.81798	0.00331	0.83718	0.00492				
0.84945	0.00684	0.84774	0.00637	0.83161	0.00511	0.84901	0.00586				
0.86059	0.00781	0.85926	0.00731	0.84491	0.00666	0.86032	0.00656				
0.87147	0.00853	0.87041	0.00797	0.85756	0.00795	0.87131	0.00700				
0.88208	0.00903	0.88123	0.00841	0.86974	0.00891	0.88201	0.00723				
0.89243	0.00930	0.89175	0.00861	0.88154	0.00959	0.89243	0.00724				
0.90258	0.00935	0.90205	0.00859	0.89300	0.00999	0.90263	0.00704				
0.91258	0.00919	0.91215	0.00836	0.90421	0.01012	0.91265	0.00662				

NASA-SC-0712_eta-0.63_0	
[illegible]	[illegible]

NASA-SC-0712_eta-0.63_0.5	
[illegible]	[illegible]

NASA-SC-0712_eta-0.63_-0.5	
[illegible]	[illegible]

NASA-SC-0712_eta-0.63_1.5	
[illegible]	[illegible]

NASA-SC-0712_eta-0.63_-1.5	
[illegible]	[illegible]

NASA-SC-0712_eta-0.63_1.0	
[illegible]	[illegible]

NASA-SC-0712_eta-0.63_-1.0	
[illegible]	[illegible]

NASA-SC-0712_eta-0.63_2.5	
[illegible]	[illegible]

NASA-SC-0712_eta-0.63_2.0	
[illegible]	[illegible]

NASA-SC-0712_eta-0.63_-2.0	
[illegible]	[illegible]
0.04645	0.03577
0.04034	0.03396
0.03467	0.03208
0.02939	0.03011
0.02447	0.02805
0.01988	0.02583
0.01562	0.02341
0.01169	0.02072
0.00813	0.01769
0.00502	0.01421
0.00248	0.01018
0.00072	0.00550
0.00020	0.00277
0.00000	0.00000
0.00048	-0.00447
0.00182	-0.00877
0.00372	-0.01234
0.00609	-0.01548
0.00883	-0.01824
0.01187	-0.02070
0.01517	-0.02289
0.01870	-0.02488
0.02245	-0.02670
0.02643	-0.02840
0.03065	-0.02998
0.03511	-0.03149
0.03986	-0.03292
0.04491	-0.03429
0.05031	-0.03563
0.05609	-0.03693
0.06232	-0.03819
0.06907	-0.03944
0.07639	-0.04069
0.08439	-0.04194
0.09316	-0.04321
0.10280	-0.04449
0.11343	-0.04578
0.12519	-0.04708
0.13820	-0.04834
0.15264	-0.04958
0.16859	-0.05079
0.18608	-0.05193
0.20506	-0.05299
0.22540	-0.05390
0.24700	-0.05465
0.26961	-0.05521
0.29301	-0.05558
0.31689	-0.05572
0.34110	-0.05564
0.36531	-0.05534
0.38927	-0.05482
0.41285	-0.05407
0.43592	-0.05308
0.45845	-0.05182
0.48052	-0.05030
0.50225	-0.04847
0.52381	-0.04634
0.54526	-0.04389
0.56680	-0.04109
0.58853	-0.03797
0.61039	-0.03455
0.63230	-0.03086
0.65389	-0.02705
0.67461	-0.02324
0.69396	-0.01958
0.71146	-0.01622
0.72688	-0.01325
0.74032	-0.01070
0.75208	-0.00849
0.76241	-0.00653
0.77156	-0.00489
0.77981	-0.00356
0.78734	-0.00226
0.79433	-0.00071
0.80098	0.00108
0.80747	0.00292
0.81399	0.00464
0.82070	0.00608
0.82780	0.00722
0.83537	0.00825
0.84338	0.00937
0.85179	0.01052
0.86060	0.01156
0.86987	0.01250
0.87951	0.01332
0.88947	0.01398
0.89970	0.01444
0.91019	0.01468
0.92088	0.01467
0.93178	0.01438
0.94290	0.01379
0.95429	0.01286
0.96600	0.01155
0.97816	0.00980
0.99102	0.00750
1.00000	0.00554

NASA-SC-0712_eta-0.63_3.5	
[illegible]	[illegible]
0.04948	0.03639
0.04317	0.03462
0.03730	0.03280
0.03184	0.03089
0.02673	0.02887
0.02195	0.02672
0.01746	0.02438
0.01329	0.02176
0.00945	0.01880
0.00600	0.01535
0.00309	0.01126
0.00094	0.00629
0.00026	0.00318
0.00000	0.00000
0.00064	-0.00519
0.00246	-0.01008
0.00482	-0.01384
0.00764	-0.01704
0.01080	-0.01979
0.01425	-0.02220
0.01795	-0.02434
0.02186	-0.02628
0.02600	-0.02806
0.03038	-0.02972
0.03502	-0.03127
0.03994	-0.03275
0.04517	-0.03416
0.05077	-0.03552
0.05676	-0.03684
0.06323	-0.03813
0.07024	-0.03940
0.07786	-0.04067
0.08621	-0.04195
0.09537	-0.04324
0.10547	-0.04454
0.11667	-0.04585
0.12907	-0.04716
0.14285	-0.04843
0.15823	-0.04968
0.17527	-0.05089
0.19397	-0.05203
0.21429	-0.05304
0.23609	-0.05389
0.25922	-0.05454
0.28337	-0.05499
0.30824	-0.05520
0.33355	-0.05517
0.35894	-0.05489
0.38406	-0.05438
0.40863	-0.05361
0.43263	-0.05257
0.45593	-0.05126
0.47873	-0.04965
0.50113	-0.04773
0.52329	-0.04547
0.54540	-0.04287
0.56762	-0.03990
0.59007	-0.03659
0.61258	-0.03298
0.63497	-0.02914
0.65669	-0.02523
0.67705	-0.02144
0.69553	-0.01791
0.71181	-0.01479
0.72590	-0.01209
0.73802	-0.00976
0.74852	-0.00781
0.75780	-0.00614
0.76610	-0.00460
0.77354	-0.00315
0.78034	-0.00200
0.78674	-0.00126
0.79295	-0.00089
0.79912	-0.00077
0.80534	-0.00079
0.81168	-0.00085
0.81822	-0.00083
0.82499	-0.00060
0.83205	-0.00013
0.83945	0.00038
0.84729	0.00074
0.85561	0.00099
0.86435	0.00116
0.87345	0.00119
0.88287	0.00104
0.89260	0.00072
0.90258	0.00018
0.91276	-0.00059
0.92312	-0.00161
0.93365	-0.00294
0.94440	-0.00457
0.95537	-0.00654
0.96664	-0.00892
0.97835	-0.01178
0.99075	-0.01526
1.00000	-0.01806

NASA-SC-0712_eta-0.63_3.0	
[illegible]	[illegible]
0.04714	0.03577
0.04122	0.03405
0.03570	0.03227
0.03053	0.03041
0.02568	0.02844
0.02113	0.02633
0.01685	0.02404
0.01286	0.02147
0.00917	0.01856
0.00585	0.01518
0.00303	0.01116
0.00093	0.00628
0.00026	0.00317
0.00000	0.00000
0.00064	-0.00516
0.00244	-0.01004
0.00474	-0.01374
0.00748	-0.01689
0.01054	-0.01960
0.01387	-0.02196
0.01742	-0.02407
0.02118	-0.02598
0.02515	-0.02773
0.02934	-0.02936
0.03376	-0.03089
0.03844	-0.03233
0.04340	-0.03371
0.04868	-0.03504
0.05432	-0.03634
0.06037	-0.03759
0.06690	-0.03883
0.07397	-0.04005
0.08168	-0.04129
0.09011	-0.04253
0.09936	-0.04379
0.10956	-0.04506
0.12082	-0.04634
0.13332	-0.04759
0.14723	-0.04884
0.16269	-0.05005
0.17981	-0.05121
0.19860	-0.05230
0.21897	-0.05326
0.24082	-0.05407
0.26390	-0.05469
0.28798	-0.05509
0.31274	-0.05525
0.33789	-0.05518
0.36306	-0.05487
0.38795	-0.05432
0.41219	-0.05353
0.43584	-0.05246
0.45885	-0.05113
0.48129	-0.04951
0.50339	-0.04758
0.52528	-0.04532
0.54713	-0.04273
0.56917	-0.03977
0.59147	-0.03647
0.61399	-0.03284
0.63650	-0.02897
0.65845	-0.02501
0.67920	-0.02114
0.69805	-0.01755
0.71468	-0.01434
0.72907	-0.01158
0.74144	-0.00923
0.75217	-0.00725
0.76165	-0.00553
0.77008	-0.00393
0.77763	-0.00254
0.78459	-0.00152
0.79125	-0.00092
0.79781	-0.00062
0.80439	-0.00048
0.81110	-0.00040
0.81800	-0.00026
0.82514	0.00009
0.83257	0.00065
0.84033	0.00122
0.84851	0.00165
0.85713	0.00197
0.86611	0.00219
0.87537	0.00226
0.88492	0.00216
0.89469	0.00188
0.90463	0.00138
0.91472	0.00066
0.92495	-0.00032
0.93531	-0.00157
0.94583	-0.00312
0.95656	-0.00500
0.96757	-0.00725
0.97898	-0.00996
0.99104	-0.01325
1.00000	-0.01590

NASA-SC-0712_eta-0.63_4.0	
[illegible]	[illegible]
0.53310	0.06468
0.50170	0.06546
0.46988	0.06594
0.43771	0.06611
0.40553	0.06600
0.37340	0.06557
0.34166	0.06488
0.31065	0.06390
0.28069	0.06268
0.25215	0.06120
0.22536	0.05953
0.20061	0.05771
0.17812	0.05578
0.15797	0.05381
0.14006	0.05182
0.12420	0.04986
0.11018	0.04795
0.09778	0.04609
0.08675	0.04427
0.07688	0.04249
0.06799	0.04072
0.05991	0.03897
0.05254	0.03718
0.04576	0.03536
0.03950	0.03348
0.03367	0.03153
0.02825	0.02948
0.02317	0.02730
0.01844	0.02491
0.01404	0.02226
0.00998	0.01925
0.00634	0.01574
0.00327	0.01156
0.00099	0.00647
0.00027	0.00327
0.00000	0.00000
0.00067	-0.00527
0.00255	-0.01024
0.00499	-0.01406
0.00791	-0.01730
0.01119	-0.02008
0.01476	-0.02251
0.01859	-0.02467
0.02265	-0.02663
0.02695	-0.02843
0.03150	-0.03010
0.03633	-0.03167
0.04147	-0.03316
0.04695	-0.03459
0.05281	-0.03597
0.05911	-0.03730
0.06594	-0.03861
0.07334	-0.03991
0.08143	-0.04121
0.09030	-0.04252
0.10006	-0.04384
0.11085	-0.04516
0.12278	-0.04649
0.13603	-0.04779
0.15076	-0.04908
0.16708	-0.05031
0.18507	-0.05148
0.20466	-0.05255
0.22574	-0.05348
0.24815	-0.05422
0.27168	-0.05477
0.29602	-0.05509
0.32089	-0.05517
0.34602	-0.05502
0.37107	-0.05463
0.39570	-0.05400
0.41978	-0.05312
0.44326	-0.05196
0.46619	-0.05052
0.48862	-0.04878
0.51077	-0.04671
0.53276	-0.04433
0.55474	-0.04159
0.57682	-0.03850
0.59905	-0.03509
0.62127	-0.03142
0.64303	-0.02761
0.66383	-0.02381
0.68304	-0.02020
0.70024	-0.01691
0.71533	-0.01401
0.72841	-0.01150
0.73972	-0.00934
0.74960	-0.00752
0.75838	-0.00594
0.76626	-0.00446
0.77337	-0.00307
0.77989	-0.00197
0.78606	-0.00130
0.79208	-0.00102
0.79807	-0.00100
0.80414	-0.00113
0.81037	-0.00130
0.81682	-0.00140
0.82354	-0.00128
0.83057	-0.00092
0.83799	-0.00049
0.84583	-0.00016
0.85415	0.00005
0.86292	0.00015
0.87208	0.00012
0.88158	-0.00007
0.89139	-0.00046
0.90147	-0.00106
0.91176	-0.00189
0.92224	-0.00300
0.93290	-0.00441
0.94378	-0.00614
0.95488	-0.00822
0.96628	-0.01071
0.97811	-0.01369
0.99063	-0.01731
1.00000	-0.02023